INSTABILITY OF HIGH MACH NUMBER POISEUILLE (CHANNEL) FLOW: LINEAR ANALYSIS AND DIRECT NUMERICAL SIMULATIONS

A Dissertation

by

ZHIMIN XIE

Submitted to the Office of Graduate and Professional Studies of
Texas A&M University
in partial fulfillment of the requirements for the degree of

DOCTOR OF PHILOSOPHY

Chair of Committee,	Sharath Girimaji
Committee Members,	Rodney Bowersox
	Hamn-Ching Chen
	William Saric
Department Head,	Rodney Bowersox

August 2014

Major Subject: Aerospace Engineering

ABSTRACT

Poiseuille flow is a prototypical wall-bounded flow in which many fundamental aspects of fluid physics can be analyzed in isolation. The objective of this research is to establish the stability characteristics of high-speed laminar Poiseuille flow by examining the growth of small perturbations and their subsequent breakdown toward turbulence. The changing nature of pressure is considered critical to the transformation from incompressible to compressible behavior. The pressure-velocity interactions are central to the present investigation.

The study employs both linear analysis and temporal direct numerical simulations (DNS) and consists of three distinct parts. The first study addresses the development and validation of the gas kinetic method (GKM) for wall-bounded high Mach number flows. It is shown that sustaining the Poiseuille flow using a body force rather than pressure-gradient is better suited for accurate numerical simulations. Effect of uniform and non-uniform grids on the simulation outcomes is examined. Grid resolution and time-step convergence studies are performed over the range of Mach numbers of interest. The next study establishes the stability characteristics at very high and very low Mach number limits. While stability at low Mach number limit is governed by the well-established Orr-Sommerfeld analysis, the pressure-released Navier-Stokes equation is shown to accurately characterize stability at the infinite Mach number limit. A semi-analytical stability evolution expression is derived. It is shown that the GKM numerical approach accurately captures the low and high Mach number solutions very precisely. The third study examines the critical effects of perturbation orientation and Mach number on linear stability, and investigates the various

stages of perturbation evolution toward turbulent flow. This study can break into two parts. In the first part, an initial value linear analysis is performed to establish the self-similar scaling of pressure and velocity perturbations. The scaling then is confirmed with DNS. Based on analytical and numerical results, regions of stability and instability in the orientation space are established. Compressibility is shown to strongly stabilize streamwise perturbations. However, span-wise modes are relatively unaffected by Mach number. The multiple stages of temporal perturbation evolution are explained. The manner of Tollmien-Schlichting (TS) instability suppression due to compressibility is also described. In the second part, the progression from linear to nonlinear to preliminary stages of breakdown is examined. It is shown that nonlinear interactions between appropriate oblique perturbation mode pairs lead to span-wise and streamwise modes. The streamwise modes rapidly decay and span-wise perturbations are ultimately responsible for instability and breakdown toward turbulence. Overall, the studies performed in this research lead to fundamental advances toward understanding transition to turbulence in wall-bounded high-speed shear flows. Such an understanding is important for developing transition prediction tools and flow control strategies.

DEDICATION

To Xue Yang

ACKNOWLEDGEMENTS

I would like to thank my advisor Dr. Sharath Girimaji for his seemingly infinite patience, encouragement, and support. I am also indebted to my committee members Dr. Rodney Bowersox, Dr. Hamn-Ching Chen and Dr. William Saric for their kind suggestions and constructive criticism.

My deepest gratitude goes toward friends and family who selflessly give much needed assistance throughout this lengthy process. A very special thank you goes to Xue, whose emotional support has been unique in my life. My parents provide all support and help to me. Gaurav, Carlos, Ashraf, Jacob and Tim, it is great to have you guys as my officemates, and you certainly make the office a fun place to work and learn.

And finally my PhD accomplishment would not have been possible without all the excellent staff members at Texas A&M. Karen Knabe, Colleen Leatherman, and Jerry Gilbert are always patient and kind-hearted to help us go through the graduation precedure.

Most of this work was funded by The National Center for Hypersonic Laminar-Turbulent Transition Research at Texas A&M University. Computational resources were provided by the Texas A&M Supercomputing Facility.

TABLE OF CONTENTS

Page

LIST OF FIGURES

FIGURE Page

LIST OF TABLES

TABLE Page

1. INTRODUCTION

1.1 Motivation

Compressibility exerts a profound influence on transition and turbulence phenomena. A preeminent example of compressibility effect on turbulent flows is the suppression of the mixing layer growth rate in supersonic mixing layers [1]. This so-called "Langley curve" effect has been extensively investigated and the probable underlying phenomena has been proposed [2–5]. Many of these studies examine compressible flow physics in homogeneous shear flow which is a reasonable idealization of free shear flows. In wall-bounded flows, the most prominent manifestation of compressibility effects is on the transition process in high-speed boundary layers. In hypersonic boundary layers over cones and flat plates, the transition zone between laminar and turbulent regions is extended over a longer distance than in comparable low-speed boundary layer [6–9]. Furthermore, during the transition, the skin friction and heat transfer coefficients demonstrate strong non-monotonic behavior that cannot be explained by intermittency alone [8]. Sivasubramanian et al. [10] show that pressure fluctuations play an important role in this region of non-monotonic behavior.

Couette and Poiseuille flows are prototypical shear flows in which many fundamental physical features of practical importance pertaining to instability, transition and turbulence can be investigated. Both flows describe fluid motion between two parallel plates, but driven in different ways. In a Couette flow, the bottom plate is stationary and the top plate moves with a uniform velocity. The resulting flow has a linear velocity profile which corresponds to uniform shear (velocity-gradient). The walls of a Poiseuille flow are stationary and the fluid between them is driven by an

applied uniform pressure gradient. The Poiseuille velocity profile is parabolic and correspondingly the shear varies in space. In computer simulations, the Couette flow away from the wall can be approximated as a homogeneous shear flow. Much work has been done on instability and turbulence in homogeneous shear (Couette) flow. Instability and turbulence in homogeneous shear flow have been extensively studied in literature [11–17]. Most recently, the instability characteristics of homogeneous shear flows over a range of Mach number values have been contrasted by [17, 18]. To extend the investigation to include wall-bounded effects, Poiseuille flow is an appropriate choice. Poiseuille or channel flow serves as an excellent idealization of wall-bounded shear flows and has been widely used to study fundamental flow phenomena. In this thesis, we focus on the stability features in inhomogeneous shear (Poiseuille) flow. Experimental investigations of the stability of plane Poiseuille flows have been performed to understand the transition process in low-speed wall-bounded flows [19]. Large eddy simulations (LES) of transition in a compressible channel flow is presented in previous works [20]. In [21] and [22], important features of fully developed compressible turbulent channel flow have been identified.

The primary objective of this thesis is to investigate the stability characteristics of small perturbation evolution toward turbulence in high-speed wall-bounded flows. In particular, we investigate the influence of perturbation obliqueness and Mach number on stability. In homogeneous shear (Couette) flow, the effect of Mach number and perturbation orientation has been investigated in [23]. In that work, self-similar scaling of the pressure equation is demonstrated and multiple stability regions in perturbation-orientation space have been identified. The critical effect of perturbation obliqueness on pressure evolution and ultimately on stability has been demonstrated. Here, we perform a similar examination for wall-bounded flows which additionally feature the Tollmien-Schlichting (TS) instability at low speeds.

The present study features direct numerical simulations (DNS) as well as linear analysis. Unlike most stability and transition studies which examine eigenvalue problems, the linear analysis solves an initial value problem. The thesis is composed of three studies:

1. Development of gas-kinetics based numerical scheme for highly compressible wall-bounded flows.

2. Investigation of the stability of Poiseuille flow at extreme Mach numbers.

3. Analysis and simulation of Poiseuille flow instability and breakdown at intermediate Mach numbers.

The brief introduction to each study is provided in this section. In subsequent sections, each of the studies is presented in detail.

1.2 Development of Numerical Approach

The Gas Kinetic Method (GKM) is employed to perform direct numerical simulations (DNS) of Poiseuille flow. The GKM is emerging as a viable alternative to Navier-Stokes (NS) based flow simulation scheme, especially for compressible flows. One of the potential advantages of the gas-kinetic approach over more conventional methods is that the former employs a single scalar gas distribution function, f, to directly compute the fluxes of mass, momentum, energy densities [24]. The underlying argument is that it is more holistic to apply the discretization to the fundamental quantity, the distribution function, rather than the derived quantities, the primitive or conservative variables. The constitutive relationships such as the stress tensor and heat flux vector are computed as moments of the distribution function on the same stencil as convective fluxes leading to inherent consistency between various

discretized conservation equations and avoiding additional viscous/conductive discretization [25–30]. The GKM also offers a more convenient numerical platform for including non-thermochemical equilibrium and non-continuum effects as precise constitutive relations are not invoked in the simulations [17]. While the potential of GKM is clearly evident, much development, verification and validation is necessary before GKM can be considered as a robust and a versatile numerical approach for a broad range of computational fluid dynamics applications.

In a series of works, our research group has explored the applicability of kinetic theory based methods of the Lattice Boltzmann Method (LBM) and GKM to a variety of turbulent flows [11–17]. In [16], the authors compare the LBM and GKM against Navier-Stokes in mildly compressible turbulent flows. The GKM is augmented with a WENO-interpolation scheme and examined over a large range of Mach numbers in decaying isotropic and homogeneous shear turbulence in [17]. Overall, the GKM solver has been well studied for free-shear layers. An important class of flows in which GKM has not been carefully scrutinized is flows undergoing transition from laminar to turbulent states. Wall-bounded flows represent another category of flows in which GKM has not been tested yet.

To extend the GKM numerical simulation to wall-bounded shear flow which has non-uniform velocity gradient, the WENO scheme must be adapted to spatially-varying grid. The non-uniform WENO scheme is expected to capture the physics better by adapting to the variation of the flow. Wang et al. [31] have derived the explicit formulation of a fifth-order WENO method on non-uniform meshes and compared the performance with the classical uniform mesh approach demonstrating the significant benefit of the non-uniform scheme. Following Wang's proposal, the non-uniform WENO is developed and implemented into the GKM solver.

When performing temporal flow simulations, forcing terms should be introduced

into the momentum equation to ensure that the flow variables behave appropriately in the stream-wise direction. The forcing term can be manifested in the calculation either through an imposed pressure-gradient or an extra body force [21,32]. Of the two options, pressure-gradient forcing must be considered more natural as it represents a physical effect. In incompressible flows, both options lead to identical outcomes. However, in compressible flows there exists a fundamental difference between the two types of forcing. As pressure is related to other thermodynamic variables through the state equation, an imposed stream-wise pressure-gradient will necessarily lead to stream-wise variations in temperature and density. This could lead to undesirable consequences in the temporal simulation outcome. Body force driving, on the other hand, does not lead to stream-wise variation in the thermodynamic state variables [20,33]. However, as mentioned earlier, the body-force approach is less intrinsic to a flow than pressure-gradient forcing. Thus, in high-speed flows both body force and pressure-gradient approaches have potential shortcomings. It is important to compare and contrast the features of these two forcing approaches over a range of Mach numbers.

To obtain reliable DNS results, the convergence study is performed to examine the numerical accuracy of GKM solver. In addition, the calculated Reynolds stress evolution equation (RSEE) [34, 35] balance is also investigated. Verifying the balance serves two important purposes: (i)identifies the relative importance of different processes, and (ii) confirms the accuracy of the numerical computations.

1.3 Instability of Poiseuille Flow at Extreme Mach Numbers

In this study, we establish the stability characteristics of Poiseuille flow at very high and very low Mach number limits before proceeding to intermediate Mach numbers in the next study. Pressure plays a profound role in shaping the nature of insta-

bility, transition and turbulence phenomena in fluid flows. The interaction between pressure and velocity field depends upon the flow-to-acoustic (pressure) timescale ratio quantified by Mach number. At the vanishing Mach number limit, pressure evolves instantaneously to impose the incompressibility constraint on the velocity field. Under these conditions, hydrodynamic pressure can be completely determined from a Poisson equation. In such incompressible flows, pressure-enabled energy redistribution mitigates instability in hyperbolic flows but initiates and sustains instability in elliptic flows [36]. The flow physics at low Mach numbers is described by the incompressible Navier-Stokes equations.

At the limit of a very high Mach number, pressure evolution is very slow compared to that of the velocity field. Consequently, the velocity field evolves nearly impervious to the pressure field. The pressure-less Navier-Stokes equation, called the pressure-released equation (PRE), describes the evolution at extremely high Mach number limits. The PRE analysis has been shown to accurately characterize the high Mach number Navier-Stokes physics in homogeneous shear flows [17, 18, 37]. The PRE analysis has also been widely used for inferring velocity gradient dynamics at very high Mach numbers [38].

In this part, we will perform a linear perturbation analysis of the pressure-released equation (PRE) to describe the evolution of small perturbations in very high Mach number Poiseuille flows. At the limit of a very small Mach number, the classical Orr-Sommerfeld analysis [39, 40] is used to evaluate perturbation evolution. In addition to the analyses, direct numerical simulations (DNS) of the Poiseuille flow at extreme Mach number limits will be performed using the Gas Kinetic Method. Apart from providing insight into the instability flow physics at extreme Mach number limits, the present study serves an important goal – to benchmark the validity of the GKM simulations at these limits.

1.4 Instability of Poiseuille Flow at Intermediate Mach Numbers

With the increase in the Mach number, the role of pressure changes significantly. As discussed before, at a very low Mach number pressure is dictated by the Poisson equation. Pressure evolves very rapidly to impose the divergence free condition to the velocity field. However, at a very high Mach number, the action of pressure is relatively slow compared to that of velocity field. Consequently, the velocity field evolves almost unaffected by pressure. At intermediate Mach numbers, the time scale of pressure evolution is comparable to that of velocity. Pressure behaves according to the wave equation resulting from the energy equation and thermodynamic state equation. In this section, we focus on the instability characteristics of Poiseuille flow at intermediate Mach numbers by investigating the evolution of small perturbation in forms of various wave modes. The study employs temporal DNS and linear analysis of the corresponding initial value problems.

The primary objective of this study is to investigate the stability characteristics of small perturbation evolution in high-speed channel flow. In particular, we investigate the influence of perturbation obliqueness and Mach number on stability. In Couette flow, the effect of Mach number and perturbation orientation has been investigated in [23]. In that work, self-similar scaling of the pressure equation is demonstrated and multiple stability regions in perturbation-orientation space have been identified. The critical effect of perturbation obliqueness on pressure evolution and ultimately on stability has been demonstrated. Here, we perform a similar examination for wall-bounded flows which additionally feature the Tollmien-Schlichting (TS) instability at low speeds. We perform both linear analysis and direct numerical simulations of small perturbation evolution in high Mach number Poiseuille flow. The linear analysis mostly focuses on the interaction between pressure and velocity perturbations in

linear regime. The influence of Mach number and perturbation obliqueness are examined. The outcome of the linear analysis is then confirmed using DNS data. Finally, breakdown toward turbulence is examined employing two coupled initial modes.

1.5 Dissertation Outline

This dissertation is organized as follows. In Section 2, we develop the numerical schemes and tools for high fidelity direct numerical simulation (DNS) of wall-bounded flows . In Section 3, the instability features at extreme Mach number limits is discussed. In Section 4, we present the instability investigation at intermediate Mach numbers. We present the conclusions in Section 5.

2. NUMERICAL APPROACH DEVELOPMENT

The compressible Navier-Stokes equations based on the ideal-gas law form the basis of our study.

$$\frac{\partial \rho^*}{\partial t^*} + \frac{\partial}{\partial x_j^*}\left(\rho^* u_j^*\right) = 0, \tag{2.1}$$

$$\frac{\partial u_i^*}{\partial t^*} + u_j^* \frac{\partial u_i^*}{\partial x_j^*} = \frac{1}{\rho^*}\frac{\partial \tau_{ij}^*}{\partial x_j^*}, \tag{2.2}$$

$$\rho^* c_v^* \left(\frac{\partial T^*}{\partial t^*} + u_j^* \frac{\partial T^*}{\partial x_j^*}\right) = \frac{\partial}{\partial x_j^*}\left(k^* \frac{\partial T^*}{\partial x_j^*}\right) + \tau_{ij}^* e_{ij}^*, \tag{2.3}$$

$$P^* = \rho^* R T^*, \tag{2.4}$$

The rate of strain tensor and stress tensor are defined as shown:

$$e_{ij}^* = \frac{1}{2}\left(\frac{\partial u_i^*}{\partial x_j^*} + \frac{\partial u_j^*}{\partial x_i^*}\right), \tag{2.5}$$

$$\tau_{ij}^* = 2\mu^* e_{ij}^* + \left[\frac{2}{3}\left(\lambda^* - \mu^*\right) e_{kk}^* - P^*\right]\delta_{ij}, \tag{2.6}$$

where asterisks denote dimensional quantities, c_v^* is the specific heat at constant volume, k^* is the coefficient of thermal conductivity, R is the specific gas constant, μ^* is the coefficient of dynamic viscosity and λ^* is the coefficient of second viscosity. The dynamic viscosity is assumed to follow Sutherland's law [41].

In this thesis, the direct numerical simulation (DNS) is based on the Gas Kinetic Method (GKM). It is important to distinguish the GKM from other kinetic theory-based models such as the Lattice Boltzmann method (LBM) and Direct Simulation Monte Carlo (DSMC). The LBM is a discrete velocity model wherein the different velocities at a given point represent a lattice structure on a velocity space grid.

DSMC is based on conceptual particles that represent a collection of molecules. The GKM, on the other hand, is a hybrid finite volume method the details of which are presented in the following discussion.

The GKM is a finite-volume numerical scheme which combines both fluid and kinetic approaches. The fluid part comes from the fact that macroscopic fluid variables are solved. The kinetic part comes from the fact that the fluxes are calculated by taking moments of a particle distribution function. The central equation for the GKM is the following:

$$\frac{\partial}{\partial t}\int_{\Omega} U dx + \oint_{A} \vec{F} \cdot d\vec{A} = 0. \tag{2.7}$$

Equation (2.7) shows the conservation of a macroscopic flow quantity (U) in a control volume (Ω). U represents mass, momentum or energy. $\vec{F}$ is the flux through the cell interfaces ($\vec{A}$). The GKM scheme can be decomposed into three stages: reconstruction, gas evolution and projection. In reconstruction, the values of macroscopic variables at cell center are interpolated to generate values at cell interface. The weighted essentially non-oscillatory (WENO) scheme [42, 43] is used for reconstruction in the present solver.

In gas evolution stage, the fluxes across cell interface are calculated using kinetic approach. The flux through a cell interface for one-dimensional flow case is the following:

$$F_1 = [F_\rho, F_{\rho v_1}, F_E]^T = \int_{-\infty}^{\infty} v_1 \psi f(x_1, t, v_1, \xi) d\Xi. \tag{2.8}$$

Equation (2.8) represents the flux calculation of mass (F_ρ), momentum ($F_{\rho v_1}$), and energy (F_E) by calculating the moments of the particle distribution function (f). Here, $d\Xi = dv_1 d\xi$, ξ is the molecular internal degrees of freedom and ψ is the vector

of moments. The expression of ψ is given by:

$$\psi = \left(1, v_1, \frac{1}{2}(v_1^2 + \xi^2)\right). \tag{2.9}$$

To calculate f, the Boltzmann equation with Bhatnagar-Gross-Krook (BGK) collision operator is used [24]. The distribution function f is solved in the form of the following:

$$\begin{aligned} f(x_{i+1/2}, t, \quad v_1, v_2, v_3, \xi) = \tfrac{1}{\tau}\textstyle\int_0^t g(x_1', t', v_1, v_2, v_3, \xi) \\ e^{-(t-t')/\tau} dt' + e^{-t/\tau} f_0(x_{i+1/2} - v_1 t). \end{aligned} \tag{2.10}$$

The particle distribution function f at cell interface $x_{i+1/2}$ and time t are presented in equation (2.10). Here, x_1' represents the particle trajectory, v_1, v_2 and v_3 are particle velocity space, τ is the characteristic relaxation time, f_0 is the initial distribution function and g is the equilibrium distribution function. f_0 and g are calculated from the reconstructed macroscopic variables at the cell interface.

After f has been solved and updated, the fluxes are calculated through equation (2.8). Then, in the projection stage with calculated fluxes, equation (2.7) gives updated cell center macroscopic values.

$$U_j^{n+1} = U_j^n - \frac{1}{x_{j+\frac{1}{2}} - x_{j-\frac{1}{2}}} \int_t^{t+\triangle t} \left(F_{j+\frac{1}{2}}(t) - F_{j-\frac{1}{2}}(t)\right) dt, \tag{2.11}$$

Equation (2.11) shows the macroscopic variable updates in one-dimensional flow case. Here, n represents the number of time step. Further details of GKM can be found in [24, 44–48].

2.1 Non-uniform WENO Scheme

The GKM scheme has been well validated in compressible homogeneous shear flow [11–17]. In [16], the authors compare the LBM and GKM against Navier-Stokes in mildly compressible turbulent flows. The GKM is augmented with a WENO-interpolation scheme and examined over a large range of Mach numbers in decaying isotropic and homogeneous shear turbulence in [17]. In this thesis, wall-bounded Poiseuille flow is considered. There exists important distinction between homogeneous shear flow and Poiseuille flow. One critical distinction between these two types of flow is the shear in background flow. The homogeneous shear flow exhibits uniform background velocity gradient, however, Poiseuille flow features variable background velocity gradient. To better capture the flow physics in Poiseuille flow, the previous uniform WENO interpolation scheme for homogeneous shear flow must be extended to non-uniform grid.

Before developing the non-uniform WENO scheme, we first present a general discussion of WENO scheme. In finite-volume schemes, the fluxes at the cell interface are required in order to determine the cell center flow variables. To calculate the fluxes at the cell interface, the flow variables at the cell center must be interpolated to the cell interface. Simple interpolation schemes such as linear and polynomial functions can be implemented. However, Gibbs-phenomenon oscillations can occur for these simple schemes in the presence of steep gradients. To prevent the occurrence of this unphysical phenomenon a sophisticated scheme, such as weighted essentially non-oscillatory (WENO) scheme, must be used. The WENO scheme uses adaptive stencils in the vicinity of steep gradients to avoid oscillation. Previous free shear flow simulations mostly use uniform WENO scheme due to mesh simplicity. In the Poiseuille flow, shear is non-uniform in the wall-normal direction. Thus, non-uniform

WENO is implemented into the GKM solver to better simulate the flow physics.

A fifth order non-uniform WENO scheme is used and its mathematical description is given in [31]. To construct 5th order WENO scheme we designate a stencil $S_r^{(i)}, r = 0, 1, 2$. For a given cell I_i, the stencil is defined as:

$$S_0 = I_{i-2}, I_{i-1}, I_i, \tag{2.12}$$

$$S_1 = I_{i-1}, I_i, I_{i+1}, \tag{2.13}$$

$$S_2 = I_i, I_{i+1}, I_{i+2}. \tag{2.14}$$

On each stencil, there exists a quadratic $P_r^{(i)}(x), r = 0, 1, 2$ constructed using the cell center value of three cells. To obtain a fifth-order accurate approximation of $u(x_{i+\frac{1}{2}})$, we choose the convex combinations of $P_r(x_{i+\frac{1}{2}})$ as:

$$u(x_{i+\frac{1}{2}}) = \sum_{r=0}^{2} w_r P_r(x_{i+\frac{1}{2}}), \tag{2.15}$$

where

$$\sum_{r=0}^{2} w_r = 1. \tag{2.16}$$

To determine the approximation of $u(x_{i+\frac{1}{2}})$, we must solve for w_r and $P_r(x_{i+\frac{1}{2}})$. First, we define the cell size as $h_m, m = 1, 2, \cdots, 5$ as:

$$h_m = \Delta x_{i-3+m}, m = 1, 2, \cdots, 5. \tag{2.17}$$

Then $P_r(x_{i+\frac{1}{2}})$ is computed as follows:

$$P_r(x_{i+\frac{1}{2}}) = \sum_{j=0}^{2} c_{rj} u_{i-r+j}, \tag{2.18}$$

Here

$$c_{rj} = b_{rj} h_{3-r+j}, \tag{2.19}$$

And b_{rj} is determined by the mesh distribution as:

$$b_{rj} = \sum_{m=j+1}^{3} \frac{\sum_{l=0,l\neq m}^{3} \left(\prod_{q=0,q\neq m,l}^{3} \left(x_{i+\frac{1}{2}} - x_{i-r+q-\frac{1}{2}} \right) \right)}{\prod_{l=0,l\neq m}^{3} \left(x_{i-r+m-\frac{1}{2}} - x_{i-r+l-\frac{1}{2}} \right.}. \tag{2.20}$$

In terms of h_m, the b_{rj} can be obtained as:

$$\begin{aligned}
b_{22} &= \frac{1}{h_1+h_2+h_3} + \frac{1}{h_2+h_3} + \frac{1}{h_3}, && (2.21)\\
b_{21} &= b_{22} - \frac{h_1+h_2+h_3}{h_2 h_3}, && (2.22)\\
b_{20} &= b_{21} + \frac{(h_1+h_2+h_3)h_3}{h_1 h_2 (h_2+h_3)}, && (2.23)\\
b_{12} &= \frac{(h_2+h_3)h_3}{(h_2+h_3+h_4)(h_3+h_4)h_4}, && (2.24)\\
b_{11} &= b_{12} + \frac{1}{h_2+h_3} + \frac{1}{h_3} - \frac{1}{h_4}, && (2.25)\\
b_{10} &= b_{11} - \frac{(h_2+h_3)h_4}{h_2 h_3 (h_3+h_4)}, && (2.26)\\
b_{02} &= -\frac{h_3 h_4}{(h_3+h_4+h_5)(h_4+h_5)h_5}, && (2.27)\\
b_{01} &= b_{02} + \frac{h_3(h_4+h_5)}{(h_3+h_4)h_4 h_5}, && (2.28)\\
b_{00} &= b_{01} + \frac{1}{h_3} - \frac{1}{h_4} - \frac{1}{h_4+h_5}. && (2.29)
\end{aligned}$$

After $P_r(x_{i+\frac{1}{2}})$ is computed, we need to find weighted coefficients w_r. The smooth measure IS_r is defined as:

$$IS_r = \int_{x_{i-\frac{1}{2}}}^{x_{i+\frac{1}{2}}} h_3 (P_r'(x))^2 dx + \int_{x_{i-\frac{1}{2}}}^{x_{i+\frac{1}{2}}} (h_3)^3 (P_r"(x))^2 dx, \tag{2.30}$$

With smooth measure IS_r, we define:

$$\alpha_r = \frac{d_r}{(\epsilon + IS_r)^2}, \tag{2.31}$$

Here ϵ is a small positive number that is introduced to avoid the denominator becoming zero. The d_r is calculated using the cell size as:

$$d_2 = \frac{(h_3+h_4)(h_3+h_4+h_5)}{(h_1+h_2+h_3+h_4)(h_1+h_2+h_3+h_4+h_5)}, \tag{2.32}$$

$$d_1 = \frac{(h_1+h_2)(h_3+h_4+h_5)(h_1+2h_2+2h_3+2h_4+h_5)}{(h_1+h_2+h_3+h_4)(h_2+h_3+h_4+h_5)(h_1+h_2+h_3+h_4+h_5)}, \tag{2.33}$$

$$d_0 = \frac{h_2(h_1+h_2)}{(h_2+h_3+h_4+h_5)(h_1+h_2+h_3+h_4+h_5)}. \tag{2.34}$$

Finally, the coefficient w_r is given by:

$$w_r = \frac{\alpha_r}{\alpha_0+\alpha_1+\alpha_2}. \tag{2.35}$$

From w_r and P_r, the interpolation value at cell interface can be obtained.

2.2 Body Force vs. Pressure Gradient Forcing

When performing temporal flow simulations, forcing terms must be introduced into the momentum equation to ensure that the flow variables behave appropriately in the stream-wise direction. The forcing term can be manifested in the calculation either through an imposed pressure-gradient or an extra body force [21,32]. Of the two options, pressure-gradient forcing must be considered more natural as it represents a physical effect. In incompressible flows, both options lead to identical outcomes. However, in compressible flows there exists a fundamental difference between the two types of forcing. As pressure is related to other thermodynamic variables through the state equation, an imposed stream-wise pressure-gradient will necessarily lead

to stream-wise variations in temperature and density. This could lead to undesirable consequences in the temporal simulation outcome. Body force driving, on the other hand, does not yield much streamwise variation in the thermodynamic state variables [20, 33]. However, as mentioned earlier, the body-force approach is less intrinsic to a flow than pressure-gradient forcing. Thus, in high-speed flows both body force and pressure-gradient approaches have potential shortcomings. It is important to compare and contrast the features of these two forcing approaches over a range of Mach numbers.

We examine the difference between body force and pressure-gradient forcing in temporal flow simulations at low and high Mach number Poiseuille flows. The uniform parabolic background velocity profile requires an uniform pressure-gradient which can be calculated from the momentum conservation equation:

$$\frac{dP^*}{dx} = -\frac{2\mu U_0}{\rho L^2}. \tag{2.36}$$

Here, μ is the dynamic viscosity, U_0 is the centerline background velocity, ρ is the density and L is half channel width. With a pressure-gradient along the stream-wise direction, the background pressure decreases linearly in the downstream direction. In compressible flows, pressure is coupled to density and temperature by the equation of state. Consequently, density and temperature also linearly change in the stream-wise direction.

In the body force case, an artificial force is applied along stream-wise direction to sustain the background flow:

$$g_x = -\frac{2\mu U_0}{\rho L^2}. \tag{2.37}$$

Since this body force is unrelated to pressure, there is no variation of the latter in the downstream direction. Other thermodynamic variables such as temperature and density are also essentially uniform along stream-wise direction.

2.3 Verification Simulations

First we perform a set of simulations to verify the fidelity of the solver. A brief introduction of flow conditions and numerical set-up are now given. The perturbation superposed into background flow is considered in current work. Three grid resolutions and four different Mach number cases are simulated to examine the numerical fidelity of GKM solver in wall-bounded Poiseuille flow.

2.3.1 Flow Conditions

To examine the small perturbation evolution, the flow field is decomposed into background flow and perturbation quantities:

$$\rho^* = \bar{\rho} + \rho', \ u_i^* = \bar{u}_i + u_i', \ P^* = \bar{P} + p', \tag{2.38}$$

Here the asterisk represents the instantaneous flow, the bar denotes background flow and the prime represents perturbation superposed to the background flow. The perturbation equations are obtained by subtracting the background flow equations from the total variable equations. In the present work, the background flow is taken to be a planar and parallel stream-wise profile:

$$\bar{u}_i = (U(y), 0, 0), \tag{2.39}$$

The background velocity profile $U(y)$ is specified as a parabolic function along the wall-normal direction. The background flow has the velocity profile:

$$U(y) = U_0(1 - \frac{y^2}{L^2}), \tag{2.40}$$

Here U_0 is the centerline value of the background velocity, y is the wall-normal coordinate and L is the half channel width.

Perturbation velocities are also introduced in the same plane:

$$u_i' = (u, v, 0), \tag{2.41}$$

The initial perturbation velocities u and v are Tollmien-Schlichting (TS) waves obtained from solutions of linear stability equation as described further in next section. The evolution of u and v will be investigated to examine the effect of body force and pressure-gradient forcing.

2.3.2 Simulation Procedure

The computational domain is a rectangular box of dimension ratio $4 : 1 : 0.1$ along x (streamwise), y (wall-normal) and z (span-wise) directions. Grid cells are evenly distributed along x and z directions, but along wall-normal direction y geometric distribution is used. The geometric grids for different resolutions are specified as:

$$\frac{l_{i+1}}{l_i} = 1.020345, i = 1, 2, 3, \cdots, n/2, n = 160, \tag{2.42}$$

$$\frac{l_{i+1}}{l_i} = 1.0125, i = 1, 2, 3, \cdots, n/2, n = 200, \tag{2.43}$$

$$\frac{l_{i+1}}{l_i} = 1.008172, i = 1, 2, 3, \cdots, n/2, n = 400, \tag{2.44}$$

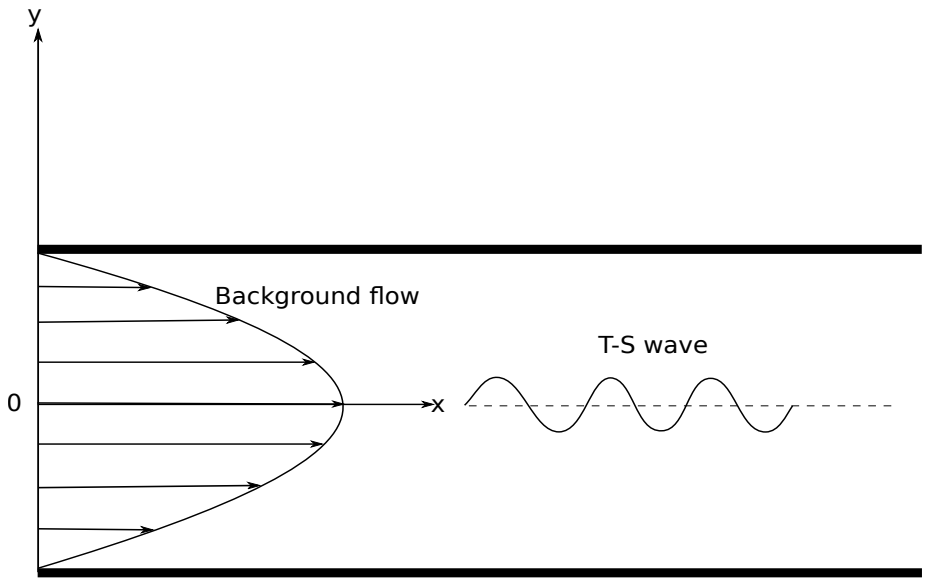

Figure 2.1: Sketch of computational domain

Table 2.1: Background flow conditions for low and high Mach number cases

	$U_0(m/s)$	$\rho(kg/m^3)$	$T(K)$	Re	M
Case1	45	1	353	45458	0.12
Case2	1130	1	353	45458	3
Case3	1883	1	353	45458	5
Case4	3013	1	353	45458	8

Here l is the cell size along y direction and n is the number of cells along y direction.

Four Mach number cases are examined to investigate the flow evolution in low-speed and high-speed regimes. The details of those cases are given in Table 2.1. The flow domain with background velocity profile and perturbation is shown in Figure 2.1. The growth or decay of perturbations with time is monitored to investigate the flow evolution. The magnitude of velocity perturbation is set to 0.5% of the value of centerline background velocity. The perturbation velocity is small enough for the evolution to be governed by linear theory. Along x and z direction periodic boundary

conditions are applied. No-slip and no-penetration wall boundaries are applied in the y direction. Temperature boundary conditions can be set to both adiabatic or isothermal conditions. The adiabatic wall inhibits heat flux across the wall by setting the temperature gradient to zero. The isothermal wall specifies a fixed temperature at the wall. It is found that both boundary conditions yield similar perturbation evolutions even though the background temperature and density profiles may be slightly different. The results presented in this paper are based on the adiabatic wall condition.

2.4 Verification Results

First, the comparison between uniform and non-uniform WENO simulation results are presented. Then the outcomes of body force and pressure gradient forcing are showed and the capability of these two forcing in high Mach number Poiseuille flow simulations is discussed. Finally, convergence study and budget consistency check are performed.

2.4.1 Uniform vs. Non-uniform Grid

Poiseuille flow simulations with uniform and non-uniform grids are compared. Both simulations use 100 cells along the wall-normal direction to compute Poiseuille flow at incompressible regime. The kinetic energy plot at Mach number 0.08 is given in Figure 2.2. The non-uniform case shows kinetic energy evolution is in good agreement with theoretical prediction. The theoretical result is based on linear stability theory which will be discussed in the next section with detail. However, the uniform case demonstrates unphysical oscillations and is clearly incorrect. Several other comparisons (figures not shown) also confirm the superiority of non-uniform grids over uniform mesh. Overall, it is evident that non-uniform WENO scheme is better suited for the Poiseuille flow simulations.

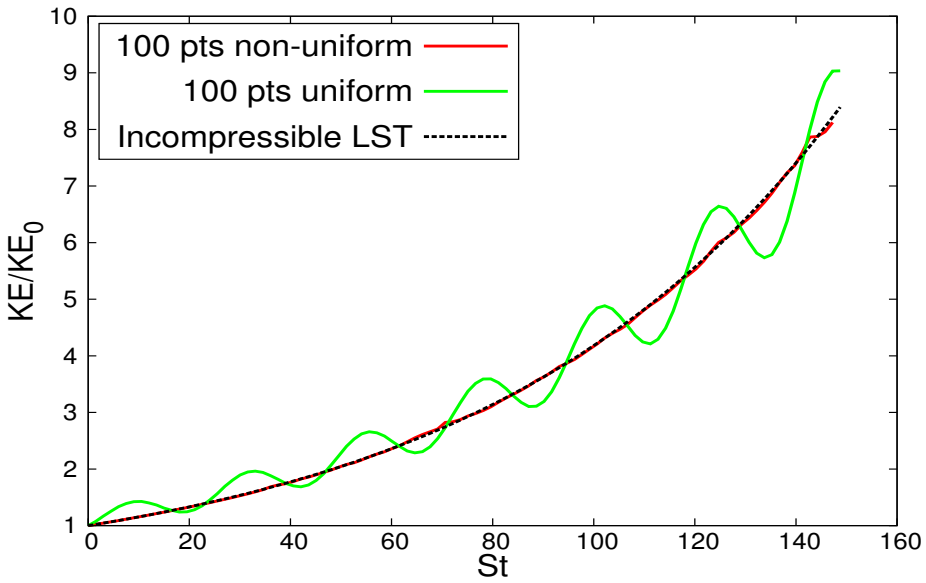

Figure 2.2: Comparison of non-uniform and uniform WENO scheme at Mach=0.08

2.4.2 Pressure Gradient vs. Body Force

Both pressure-gradient and body force are considered to sustain the background flow. The kinetic energy evolution of small perturbation is examined to compare the effect of those two driving forces. The volume-averaged kinetic energy evolution is shown in Figure 2.3. The kinetic energy evolution is plotted against normalized time: $t^* = \frac{U_0 t}{L}$. The linear stability theory prediction is also shown for comparison. Excellent agreement between computation and analysis is seen. The thermodynamic variables, such as temperature and density, are initially uniform throughout the flow domain implying no thermodynamic fluctuations. During the evolution, the temperature and density changes are examined. Figure 2.4 gives the comparison between velocity perturbation and temperature perturbation. The maximum values of perturbation velocity and temperature during the evolution are plotted as a function of time. For both forcing cases, the temperature perturbation is scaled 100 times. Clearly in low-speed flow thermodynamic quantities such as temperature and density

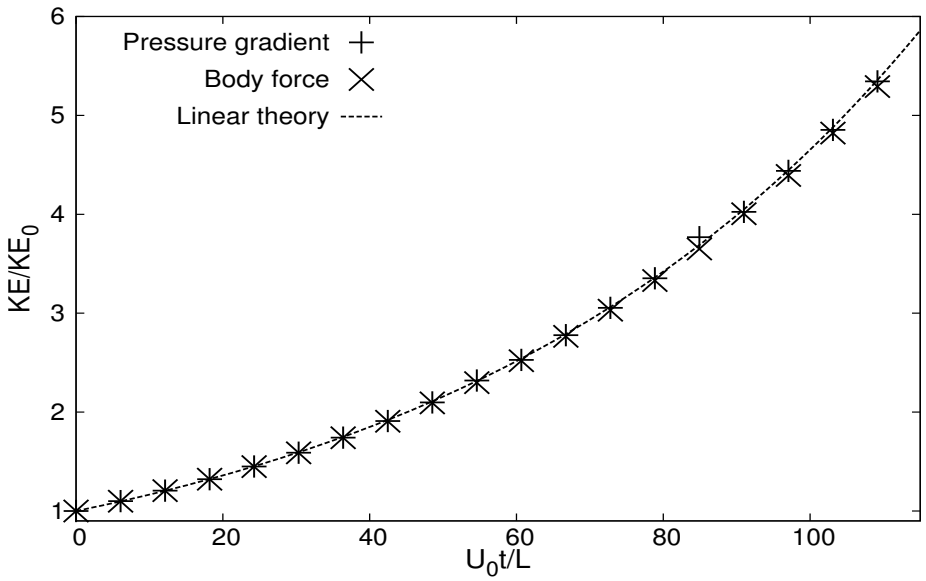

Figure 2.3: Evolution of perturbation kinetic energy at Mach=0.12

change very little from their initial state.

The kinetic energy evolution of the body force and pressure-gradient driven simulations at Mach 8 are compared in Figure 2.5. While the two cases are initially very similar, the pressure-gradient simulation becomes unstable at 65 time units and produces unphysical results. The difference between the two schemes becomes noticeable at a much earlier time—approximately 35 time units onward. Pressure-gradient simulation results may be unphysical from 35 time units. Many transition to turbulence studies [49] require high fidelity over a period of hundred time units. Thus it is reasonable to infer that pressure-gradient forcing is not suitable for long duration simulations. The reason for this is investigated next.

The difference of the background thermodynamic variables between the two forcing types is examined. For pressure-gradient forcing, the background pressure and temperature contours are given in Figure 2.6 for Mach 8 case at normalized time $t^* = 12$. Pressure decreases linearly along stream-wise direction. Temperature ex-

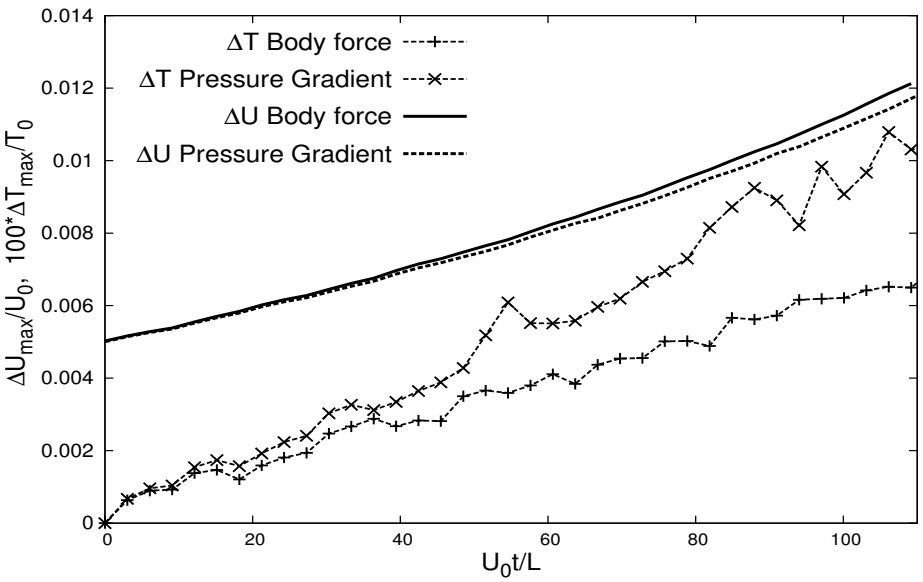

Figure 2.4: Comparison of velocity and temperature perturbation evolution at Mach=0.12

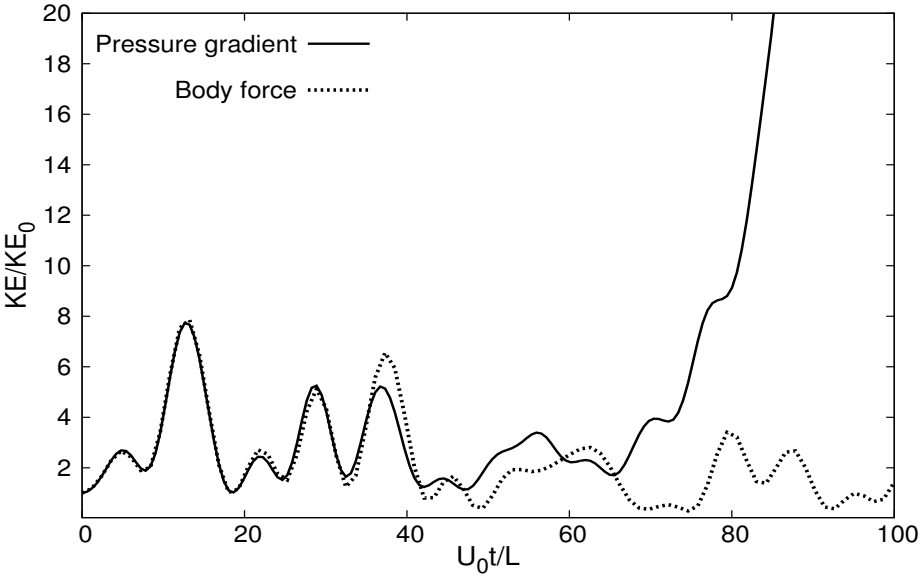

Figure 2.5: Evolution of perturbation kinetic energy at Mach=8

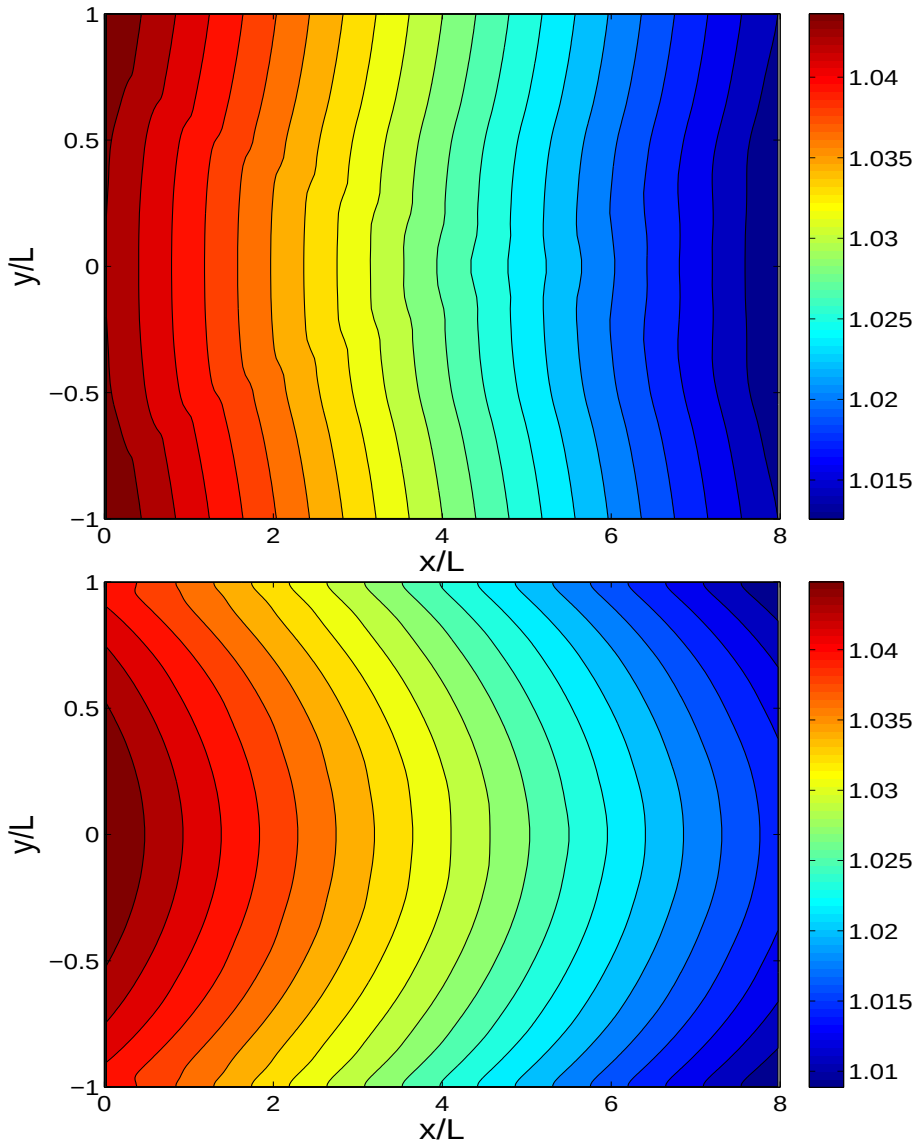

Figure 2.6: Pressure(top) and temperature(bottom) contours for pressure-gradient case at t^*=12: P is normalized by $P_0 = 101311Pa$, T is normalized by $T_0 = 353K$

hibits similar behavior. The observed background thermodynamic field behavior is clearly non-uniform in streamwise direction. This is at odds with the basic tenets of a temporal simulation. For the body force case, the pressure and temperature contours at Mach 8 are shown in Figure 2.7. Uniform pressure and temperature behavior along the stream-wise direction is clearly seen. Clearly, the body force sim-

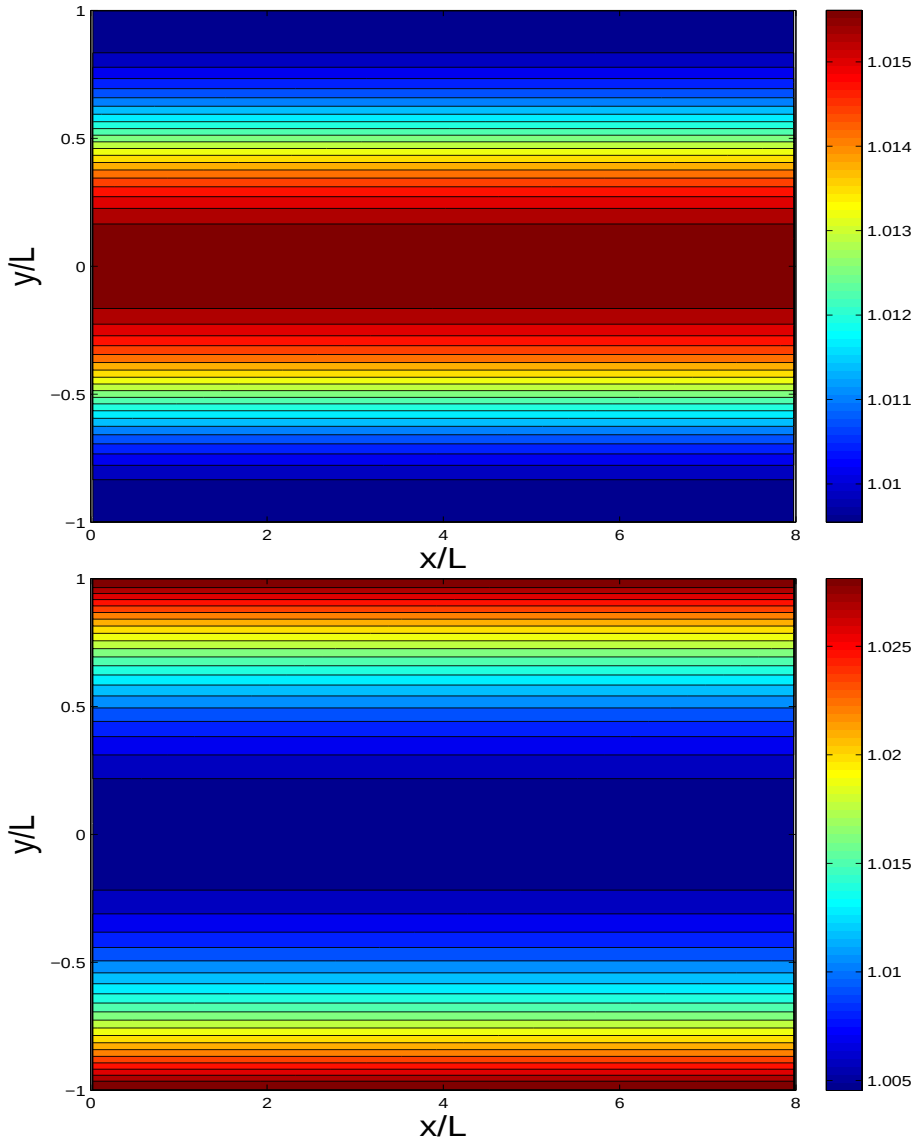

Figure 2.7: Pressure(top) and temperature(bottom) contours for body force case at $t^* = 12$: P is normalized by $P_0 = 101311Pa$, T is normalized by $T_0 = 353K$

ulation produces a background thermodynamic field with very little variation in the stream-wise direction as required. This stream-wise homogeneity of thermodynamic variables makes body force better suited for temporal simulation. Overall, for high Mach number simulations, body force and pressure-gradient forcing yield distinctly different background thermodynamic features and perturbation kinetic energy evo-

lutions deviate from each other beyond early stages.

2.4.3 Convergence Study

In high-speed flow regime, we perform a convergence study for grid resolution and time step. Three Mach numbers are considered: 3, 5, and 8. The background flow conditions for these three Mach number cases are given in Table 2.1. The volume averaged kinetic energy is considered as the representation of perturbation evolution in the simulation. The grid convergence study focuses on the resolution along wall-normal direction. Three grid resolutions are investigated for all three Mach number cases. The grid convergence study results are shown in Figures 2.8, 2.10 and 2.12. The kinetic energy evolutions for those three grid resolutions are in good agreement. The time-step convergence study results are shown in Figures 2.9, 2.11 and 2.13. Four time-steps are considered for Mach 3 and 5 cases, whereas six time-steps are examined for Mach 8 case. The kinetic energy evolutions of different time steps are also shown to be in good agreement. Thus, both grid and time step convergence for high-speed Poiseuille flow simulations is demonstrated.

2.4.4 Reynolds Stress Budget

Reynolds stress is an important quantity in examining stability, especially in turbulent flows. We focus on the Reynolds stress evolution equation to examine the fidelity of the numerical scheme in greater detail. The Favre-averaged Reynolds stress evolution equation [35] is used to scrutinize the Reynolds stress budget. The Favre-averaged Reynolds stress equation is given as follows:

$$\frac{\partial \tau_{ij}}{\partial t} + \frac{\partial \tilde{u}_k \tau_{ij}}{\partial x_k} = P_{ij} + \Pi_{ij} - \epsilon_{ij} + T_{ij} + W_{ij}, \tag{2.45}$$

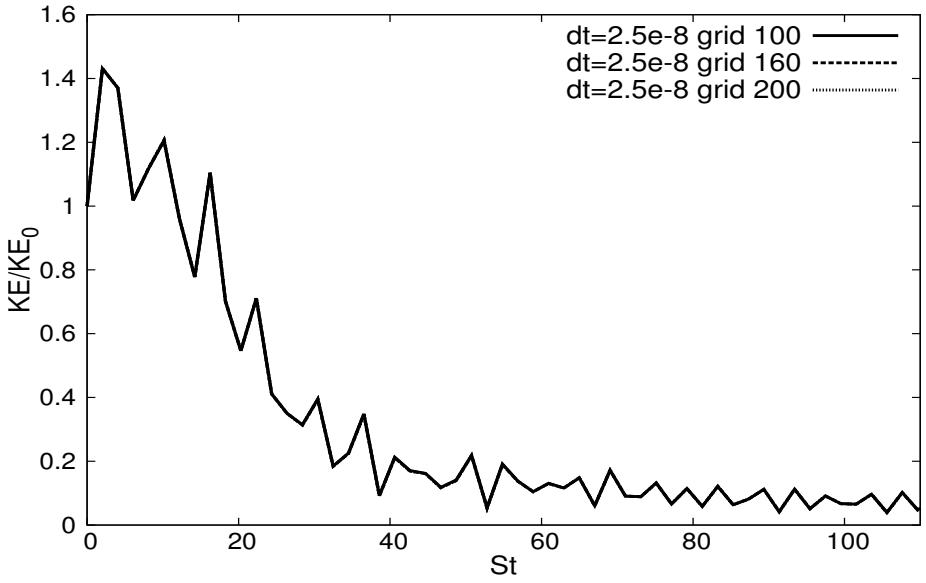

Figure 2.8: Grid resolution study at Mach=3

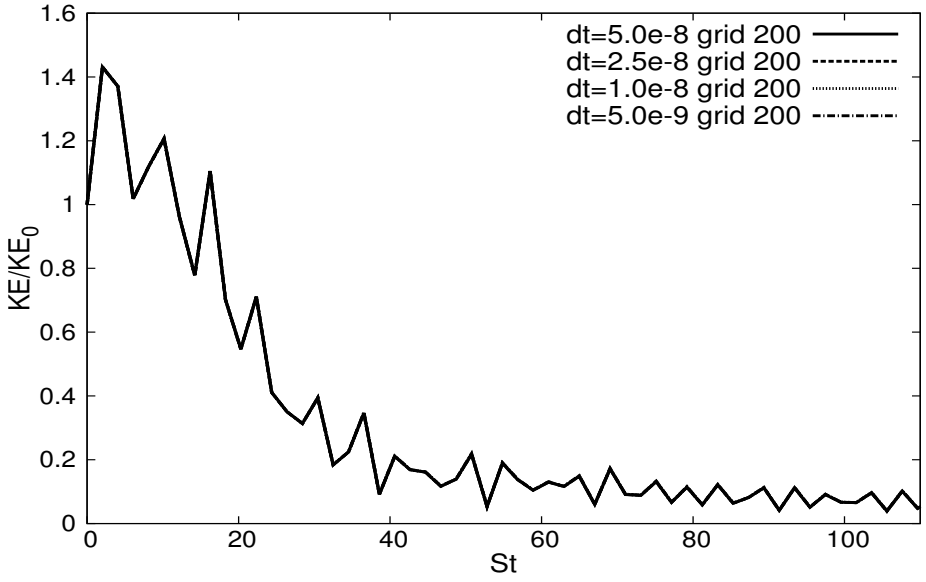

Figure 2.9: Time step study at Mach=3

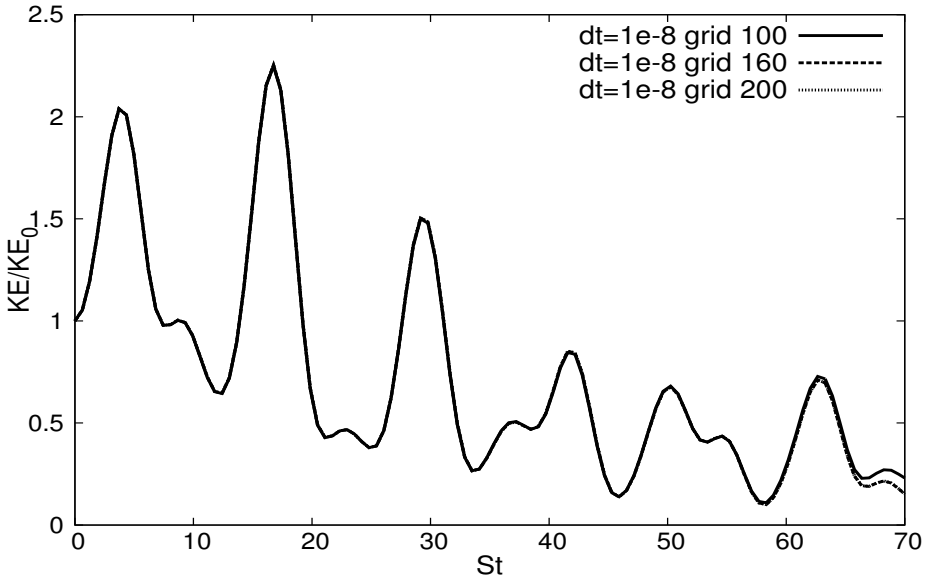

Figure 2.10: Grid resolution study at Mach=5

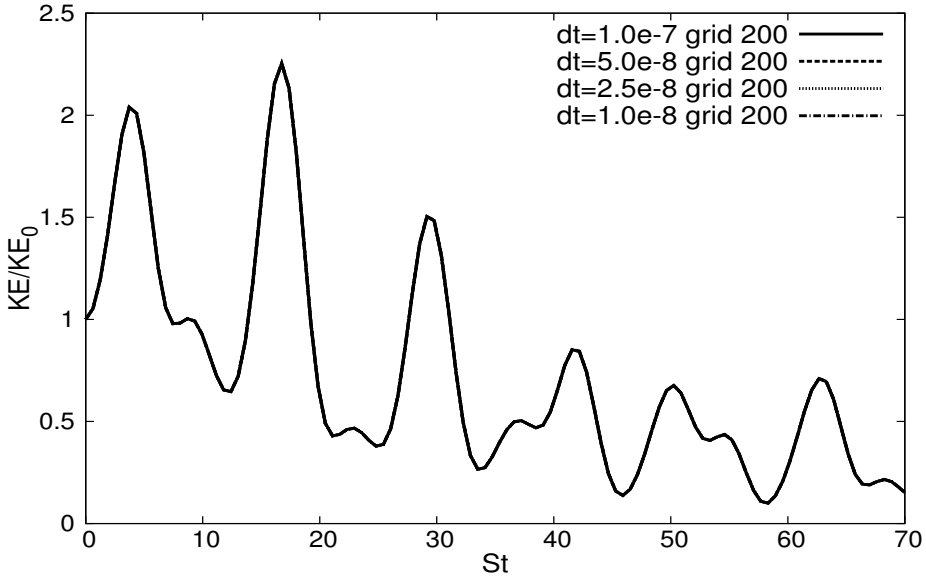

Figure 2.11: Time step study at Mach=5

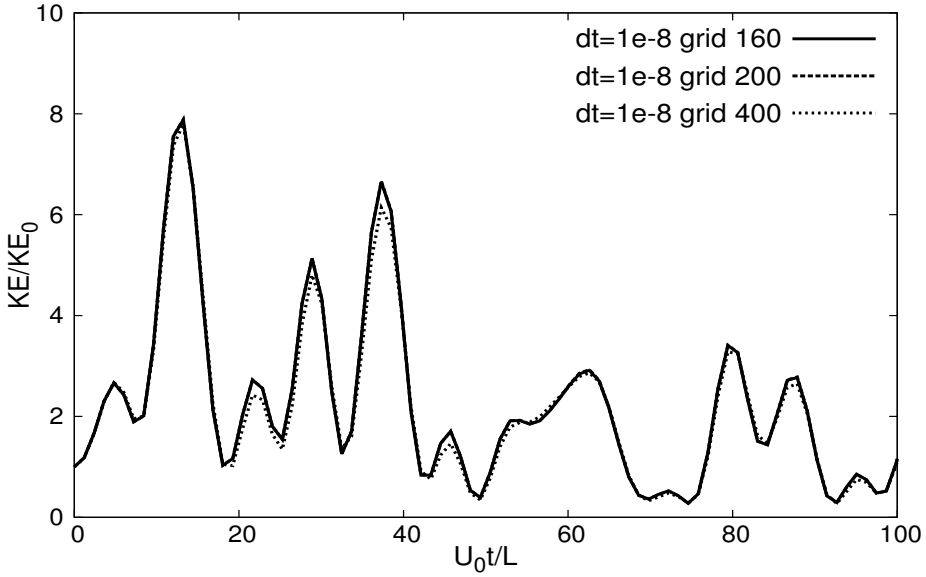

Figure 2.12: Grid resolution study at Mach=8

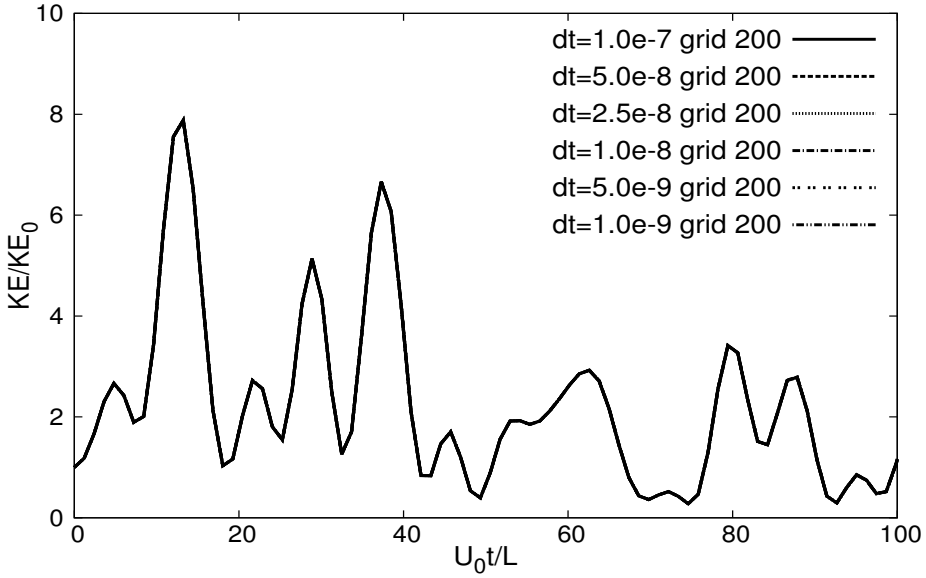

Figure 2.13: Time step study at Mach=8

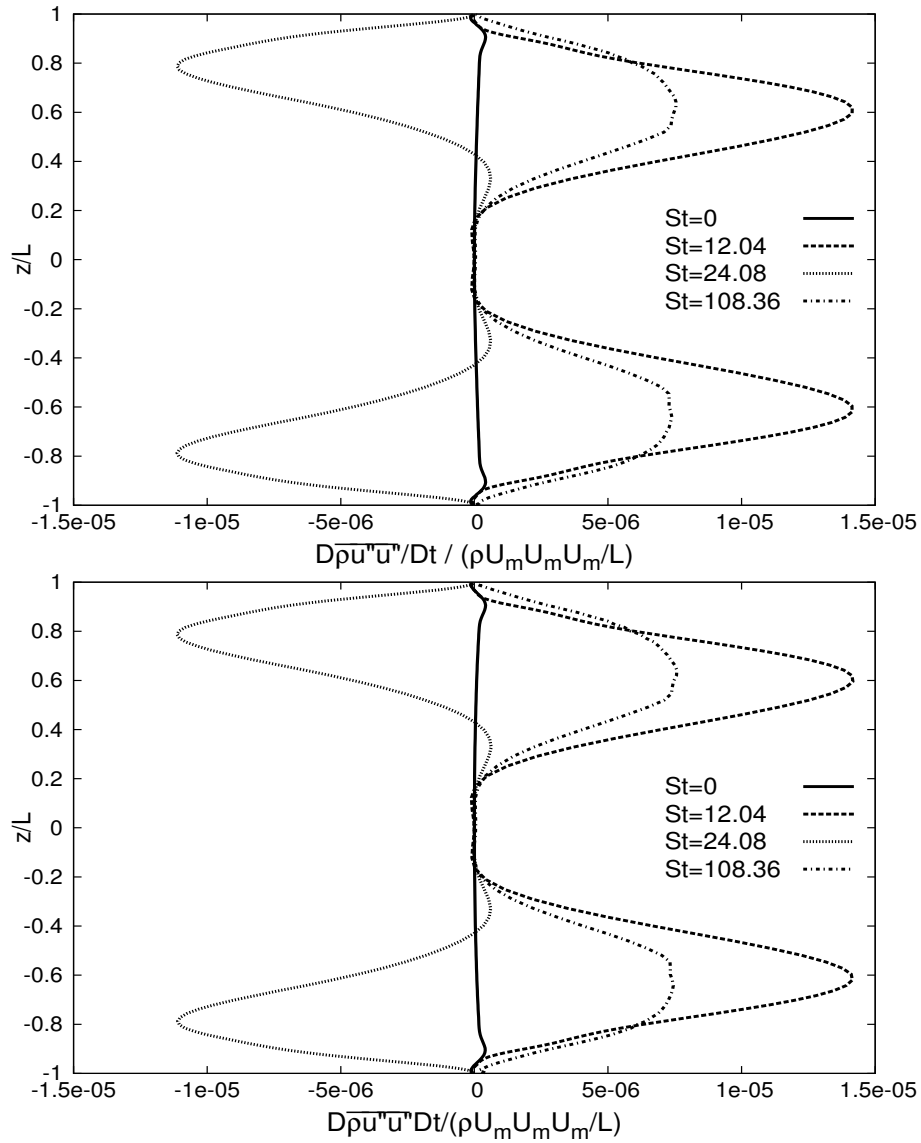

Figure 2.14: Budget equation for τ_{11} check at Mach 8: left hand side (top) and right hand side(bottom)

The various terms in this equation are: Reynolds stress, $\tau_{ij} = \overline{\rho u_i'' u_j''}$; production, $P_{ij} = -\tau_{ik}\partial\tilde{u}_j/\partial x_k - \tau_{jk}\partial\tilde{u}_i/\partial x_k$; and, velocity-pressure-gradient-tensor, $\Pi_{ij} = -\overline{u_i''\partial p'/\partial x_j + u_j''\partial p'/\partial x_i}$. Other terms such as dissipation ϵ_{ij}, transport term T_{ij} and work W_{ij}, are trivial in this work.

We compute the two sides of equation to examine the numerical accuracy of the

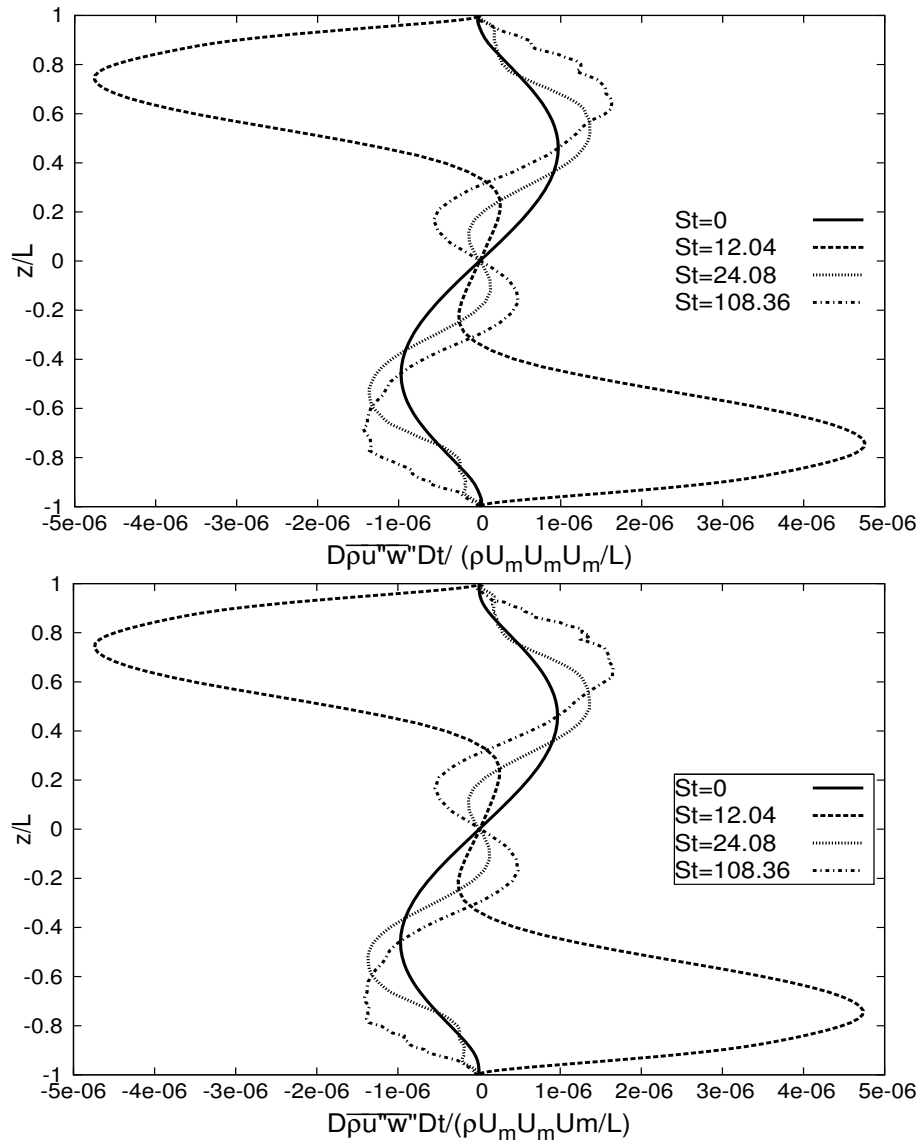

Figure 2.15: Budget equation for τ_{13} check at Mach 8: left hand side (top) and right hand side(bottom)

budget in simulation. Both sides of equation (2.45) are independently calculated from the DNS data. The left and right side of equation are shown in Figures 2.14 and 2.15 for two Reynolds stress components. The exact equivalence of left and right side of the Reynolds stress evolution equation strongly supports the reliability of the present budget analysis. The internal consistency check of this equation confirms the validity of the simulation and the physical phenomena precisely captured by DNS.

2.5 Summary and Conclusion

In this section, we examine the applicability of GKM for wall-bounded Poiseuille flow in both low-speed and high-speed flow regimes. To better accommodate the spatial variation in Poiseuille flow, the fifth order non-uniform WENO scheme is developed and implemented into the GKM solver. The simulation results for both uniform and non-uniform WENO schemes are compared by examining the kinetic energy evolution. Non-uniform WENO is shown to have better performance. Furthermore, both body force and pressure-gradient are applied to sustain the flow. For low-speed flow, small perturbation evolution agrees well with linear theory for both driving cases and those two driving sources do not significantly alter the thermodynamic quantity evolution due to weak thermodynamic coupling. For high-speed flow, body force driving produces a background thermodynamic field that is uniform in the stream-wise direction. Pressure-gradient driven simulation results show undesirable stream-wise gradients leading to unphysical results. Therefore, body force driven temporal simulations appear to be better suited for temporal simulations of compressible flows. Convergence study is performed to obtain reliable simulation result for GKM scheme in Poiseuille flow. The Reynolds stress evolution equation is examined numerically in the DNS data. The two sides of the budget equation are shown to have exact equivalence in the simulation results. This study establishes

the fidelity of the numerical scheme. Now we proceed with further investigation to examine the stability of high-speed Poiseuille flows.

3. INSTABILITY OF POISEUILLE FLOW AT EXTREME MACH NUMBERS*

The main objective of this study is to examine the stability of Poiseuille flow at the two extremes of Mach number—incompressible and highly compressible limits. The main distinguishing feature between the two extreme limits of Poiseuille/channel flow is the action of pressure. Pressure plays a profound role in shaping the nature of instability, transition and turbulence phenomena in fluid flows. The interaction between pressure and velocity fields depends upon the flow-to-acoustic (pressure) timescale ratio quantified by the Mach number. At the vanishing Mach number limit, pressure evolves very rapidly to impose the incompressibility constraint on the velocity field. Under these conditions, hydrodynamic pressure can be completely determined from a Poisson equation. In such incompressible flows, pressure-enabled energy redistribution mitigates instability in hyperbolic flows, but initiates and sustains instability in elliptic flows [36]. The flow physics at low Mach numbers is described by the incompressible Navier-Stokes equations.

With the increasing Mach number, the nature of pressure action on the flow field changes. Pressure evolves according to a wave-equation resulting from energy conservation statement and the thermodynamic state equation. In high speed flows, as the timescale of velocity and pressure become comparable, pressure does not act rapidly enough to impose the divergence-free constraint on the velocity field. This in turn leads to the flow becoming compressible with significant changes in density across the field. At the limit of a very high Mach number, pressure evolution is very slow compared to that of the velocity field. Consequently, the velocity field evolves

*Reprinted with permission from "Instability of Poiseuille flow at extreme Mach numbers: Linear analysis and simulations" by Z. Xie and S. S. Girimaji, 2014, *Physical Review E*, 89, 043001, Copyright[2014] by American Physical Society

nearly impervious to the pressure field. The pressure-less Navier-Stokes equation, called the pressure-released equation (PRE), describes the evolution at extremely high Mach numbers. The PRE flow behavior has been shown to accurately characterize the high Mach number Navier-Stokes physics in homogeneous shear (Couette) flows [17, 18, 37]. The PRE equation has also been widely used for inferring velocity gradient dynamics at very high Mach numbers [38].

In this study, we will perform a linear perturbation analysis of the pressure-released equation (PRE) to describe the evolution of small perturbations in very high Mach number Poiseuille flows. At the limit of a very small Mach number, the classical Orr-Sommerfeld analysis is used to evaluate perturbation evolution. In addition to the analyses, direct numerical simulations (DNS) of the Poiseuille flow at extreme Mach numbers will be performed using the Gas Kinetic Method (GKM). Apart from providing insight into the instability flow physics at extreme Mach numbers, the present study serves an important second goal – to benchmark the validity of the GKM simulations at these limits.

The outline of this section is organized as follows. Section 3.1 contains the fundamental governing equations and linear analyses at the two Mach number limits. The simulation cases conditions are given in section 3.2. Comparison between the analysis and numerical results are shown in section 3.3. The conclusion is given in section 3.4 with a brief discussion.

3.1 Linear Analysis

We present the linear analysis of small perturbation evolution at both high Mach and low Mach number limit. The compressible Navier-Stokes equations along with the ideal-gas assumption form the basis of our analysis. These equations are given in (2.1), (2.2), (2.3) and (2.4). The equations are non-dimensionalized with the

following reference quantities: density ρ_0, velocity U_0, temperature T_0, characteristic length L, viscosity μ_0, heat conductivity k_0 and speed of sound a_0. The specific values of these quantities depend on the flow under consideration. For the channel flow, the reference values are those of background flow at the centerline at $t = 0$. L is half channel width. The dimensionless quantities are defined as:

$$\begin{aligned} \rho = \rho^*/\rho_0,\ u_i = u_i^*/U_0,\ T = T^*/T_0, \\ P = P^*/\rho_0 a_0^2,\ x_i = x_i^*/L,\ t = U_0 t^*/L, \\ \mu = \mu^*/\mu_0,\ \lambda = \lambda^*/\mu_0,\ k = k^*/k_0. \end{aligned} \tag{3.1}$$

The dimensionless compressible NS equations can be rewritten as follows:

$$\frac{\partial \rho}{\partial t} + \frac{\partial}{\partial x_j}(\rho u_j) = 0, \tag{3.2}$$

$$\frac{\partial u_i}{\partial t} + u_j \frac{\partial u_i}{\partial x_j} = -\frac{1}{\rho}\frac{\partial P}{\partial x_i}\frac{1}{M^2} + \frac{\mu}{\rho}\frac{\partial^2 u_i}{\partial x_j \partial x_j}\frac{1}{Re} + \frac{\mu + 2\lambda}{3\rho}\frac{\partial^2 u_j}{\partial x_i \partial x_j}\frac{1}{Re}, \tag{3.3}$$

The pressure equation is:

$$\begin{aligned} \frac{\partial P}{\partial t} \quad + \quad u_j \frac{\partial P}{\partial x_j} = \frac{\partial}{\partial x_j}\left(\frac{k}{\rho}\frac{\partial P}{\partial x_j} - \frac{kP}{\rho^2}\frac{\partial \rho}{\partial x_j}\right)\frac{\gamma}{RePr} + \frac{2}{3}(\lambda - \mu)\frac{\partial u_j}{\partial x_j}\frac{\partial u_k}{\partial x_k}\frac{\gamma(\gamma-1)M^2}{Re} \\ + \quad \frac{1}{2}\mu\left(\frac{\partial u_i}{\partial x_j}\frac{\partial u_i}{\partial x_j} + 2\frac{\partial u_i}{\partial x_j}\frac{\partial u_j}{\partial x_i} + \frac{\partial u_j}{\partial x_i}\frac{\partial u_j}{\partial x_i}\right)\frac{\gamma(\gamma-1)M^2}{Re} - P\frac{\partial u_k}{\partial x_k}\gamma, \end{aligned} \tag{3.4}$$

The relevant dimensionless parameters are: Reynolds number Re, Mach number M, Prandtl number Pr and specific heat ratio γ:

$$Re = \frac{\rho_0 U_0 L}{\mu_0},\ M = \frac{U_0}{a_0},\ Pr = \frac{c_p^* \mu_0}{k_0},\ \gamma = \frac{c_p^*}{c_v^*}, \tag{3.5}$$

In the DNS simulations the Prandtl number Pr is held constant at 0.7. The specific heat ratio γ is held constant at 1.4.

3.1.1 High Mach Number Linear Analysis

While the DNS performed in this work employs the full equation set, the analysis is restricted to inviscid (and non-conducting) flow phenomena. The simplified equations are:

$$\frac{\partial \rho}{\partial t} + \frac{\partial}{\partial x_j}(\rho u_j) = 0, \tag{3.6}$$

$$\frac{\partial u_i}{\partial t} + u_j \frac{\partial u_i}{\partial x_j} = -\frac{1}{\rho}\frac{\partial P}{\partial x_i}\frac{1}{M^2}, \tag{3.7}$$

$$\frac{\partial P}{\partial t} + u_j \frac{\partial P}{\partial x_j} = -P\frac{\partial u_k}{\partial x_k}\gamma. \tag{3.8}$$

To investigate flow stability, we examine the small perturbation evolution. We decompose the flow field into background flow and perturbation quantities:

$$\rho = \bar{\rho} + \rho',\ u_i = \bar{u}_i + u_i',\ P = \bar{P} + P'. \tag{3.9}$$

The background flow equations have a form that is similar to that of total flow:

$$\frac{\partial \bar{\rho}}{\partial t} + \frac{\partial}{\partial x_j}(\bar{\rho}\bar{u}_j) = 0, \tag{3.10}$$

$$\frac{\partial \bar{u}_i}{\partial t} + \bar{u}_j \frac{\partial \bar{u}_i}{\partial x_j} = -\frac{1}{\bar{\rho}}\frac{\partial \bar{P}}{\partial x_i}\frac{1}{M^2}, \tag{3.11}$$

$$\frac{\partial \bar{P}}{\partial t} + \bar{u}_j \frac{\partial \bar{P}}{\partial x_j} = -\bar{P}\frac{\partial \bar{u}_k}{\partial x_k}\gamma. \tag{3.12}$$

The perturbation evolution equation can be obtained by subtracting the background flow equations (3.10)-(3.12) from the corresponding full equations (3.6)-(3.8):

$$\frac{\partial \rho'}{\partial t} + \frac{\partial}{\partial x_j}\left(\rho' \bar{u}_j + \bar{\rho} u_j' + \rho' u_j'\right) = 0, \tag{3.13}$$

$$\frac{\partial u_i'}{\partial t} + \bar{u}_j \frac{\partial u_i'}{\partial x_j} + u_j' \frac{\partial \bar{u}_i}{\partial x_j} + u_j' \frac{\partial u_i'}{\partial x_j} = -\frac{1}{\bar{\rho}} \frac{\partial P'}{\partial x_i} \frac{1}{M^2} + \frac{\rho'}{\bar{\rho}^2} \frac{\partial (\bar{P} + P')}{\partial x_i} \frac{1}{M^2}, \tag{3.14}$$

$$\frac{\partial P'}{\partial t} + \bar{u}_j \frac{\partial P'}{\partial x_j} + u_j' \frac{\partial \bar{P}}{\partial x_j} + u_j' \frac{\partial P'}{\partial x_j} = -(\bar{P} \frac{\partial u_k'}{\partial x_k} + P' \frac{\partial \bar{u}_k}{\partial x_k} + P' \frac{\partial u_k'}{\partial x_k})\gamma, \tag{3.15}$$

Equation (3.14) stipulates the balance between flow inertia on the left hand side(LHS) and the pressure forces on the right hand side(RHS). The pressure forces are inversely proportional to the square of Mach number, indicating its reduction with increasing flow velocity. At the limit of infinite Mach number, the pressure effects can be negligible and the momentum following a background streamline will be nearly unchanged:

$$\lim_{M \to \infty} \left[-\frac{1}{\bar{\rho}} \frac{\partial P'}{\partial x_i} \frac{1}{M^2} + \frac{\rho'}{\bar{\rho}^2} \frac{\partial (\bar{P} + P')}{\partial x_i} \frac{1}{M^2} \right] \longrightarrow 0, \tag{3.16}$$

This represents the pressure-released limit of flow. Clearly the description will be valid only for a finite period of time as the integrated RHS, however small initially, will ultimately affect the momentum [18, 50]. The equation (3.14) in absence of the pressure terms is called the pressure-released equation (PRE) for velocity perturbations. The form of equation (3.14) clearly indicates that the duration of PRE validity will increase with increasing the Mach number as demonstrated in [50] for homogeneous shear flow. During the period of PRE validity, the energy equation decouples from the momentum equation as the changes in thermodynamic fluctuations are too slow to affect the velocity field evolution.

The background flow follows the parallel shear flow condition and planar velocity

perturbations are considered:

$$\bar{u}_i = (U(y), 0, 0), \tag{3.17}$$

$$u_i' = (u, v, 0). \tag{3.18}$$

As in the incompressible transition analysis, we restrict our considerations to planar velocity perturbations. Non-planar and oblique perturbations will be considered in future works. We formulate the PRE analysis for the evolution of small perturbations in a channel flow. We linearize the equations retaining only terms of order one in the perturbation field. Finally, the linearized PRE for small perturbation evolution in parallel non-uniform shear flows can be written as:

$$\frac{\partial u}{\partial t} + U\frac{\partial u}{\partial x} + v\frac{dU}{dy} = 0, \tag{3.19}$$

$$\frac{\partial v}{\partial t} + U\frac{\partial v}{\partial x} = 0. \tag{3.20}$$

Perturbations that are periodic in x-direction are investigated. We take the normal mode approach [39, 40] to solve the perturbation evolution equations. Normal mode forms of perturbations are given as:

$$u = \hat{u}(y,t)e^{i\alpha x}, \tag{3.21}$$

$$v = \hat{v}(y,t)e^{i\alpha x}, \tag{3.22}$$

Here $\hat{u}$ and $\hat{v}$ are the mode amplitudes of u and v velocity perturbations. The resulting mode amplitude equations are:

$$\frac{D\hat{u}(y,t)}{Dt} = -\hat{v}(y,t)\frac{dU}{dy}, \tag{3.23}$$

$$\frac{D\hat{v}(y,t)}{Dt} = 0, \tag{3.24}$$

$\frac{D}{Dt}$ represents the time rate of change in the frame moving with background flow. The mode amplitudes are clearly functions of y-coordinate and time. Therefore, the solutions to these equations will be of the form:

$$\hat{u}(y,t) = \hat{u}(y,0) - \hat{v}(y,0)\frac{dU}{dy}(y)t, \tag{3.25}$$

$$\hat{v}(y,t) = \hat{v}(y,0). \tag{3.26}$$

The solution is very similar to the homogeneous shear flow PRE result, with the exception that the amplitude is dependent on the y-coordinate as shear is not uniform. Given the background shear variation(dU/dy) and the initial perturbation profile $\hat{u}(y,0)$ and $\hat{v}(y,0)$, all the flow variables can be analytically determined at later times. Bertsch et al. [18] estimate the duration as a function of the Mach number over which the PRE solution will remain a reasonable idealization of a high Mach number homogeneous shear flow. They show that PRE result is valid for time range [18]:

$$\tau = \frac{St^*}{M^{1/2}} \sim 1.8, \tag{3.27}$$

where S is the local value of shear which is uniform in homogeneous shear flow. These results will be used to examine the high Mach number behavior of flow perturbations in the results section.

3.1.2 Low Mach Number Linear Analysis

For incompressible flow, the linear analysis of small perturbation evolution is well established [39,40,51]. The divergence-free velocity condition decouples the momentum and energy equations. The flow can again be decomposed into background

and perturbation velocities. The perturbation velocity equations are obtained by subtracting background flow equations from total flow equations:

$$\frac{\partial u_i'}{\partial x_i} = 0, \tag{3.28}$$

$$\frac{\partial u_i'}{\partial t} + \bar{u}_j \frac{\partial u_i'}{\partial x_j} + u_j' \frac{\partial \bar{u}_i}{\partial x_j} + u_j' \frac{\partial u_i'}{\partial x_j} = -\frac{\partial p'}{\partial x_i} + \frac{1}{Re} \frac{\partial^2 u_i'}{\partial x_j \partial x_j}, \tag{3.29}$$

Here prime represents perturbation quantities and overbar represents background quantities as before. The normalization is similar to equation(3.1), except pressure is normalized in incompressible flows as: $P_0 = \rho_0 U_0^2$. The specific values of these quantities depend on the flow under consideration. For the channel flow, the reference values are those of background flow at the centerline at $t = 0$. L is half channel width. The only dimensionless parameter of relevance is the Reynolds number Re.

The background flow and perturbations are given in equations (3.17)and(3.18). This planar velocity perturbation is found to be most unstable from linear stability theory perspective [39,40]. The perturbation equations reduce to the following forms:

$$\frac{\partial u}{\partial x} + \frac{\partial v}{\partial y} = 0, \tag{3.30}$$

$$\frac{\partial u}{\partial t} + U \frac{\partial u}{\partial x} = -\frac{\partial p'}{\partial x} + \frac{1}{Re} \left(\frac{\partial^2 u}{\partial x \partial x} + \frac{\partial^2 u}{\partial y \partial y} \right) - v \frac{dU}{dy}, \tag{3.31}$$

$$\frac{\partial v}{\partial t} + U \frac{\partial v}{\partial x} = -\frac{\partial p'}{\partial y} + \frac{1}{Re} \left(\frac{\partial^2 v}{\partial x \partial x} + \frac{\partial^2 v}{\partial y \partial y} \right). \tag{3.32}$$

In this analysis, the viscous term is retained as its effect is essential for the instability under consideration. We take the complex normal mode approach to

solve perturbation equations. Normal modes of perturbations are given as [40]:

$$u = \psi(y)e^{i\alpha(x-ct)}, \tag{3.33}$$

$$v = \phi(y)e^{i\alpha(x-ct)}, \tag{3.34}$$

$$p' = p(y)e^{i\alpha(x-ct)}, \tag{3.35}$$

ψ, ϕ and p are complex magnitude of perturbation velocity and pressure. α is wavenumber of perturbation along streamwise direction. c is the complex phase speed which will be calculated from equation. By substituting those normal modes form into perturbation equations and combining those equations together, we can generate a single stability equation–Orr-Sommerfeld equation(OSE) [51]. The OSE is given as:

$$\frac{d^4\phi}{dy^4} - 2\alpha^2\frac{d^2\phi}{dy^2} + \alpha^4\phi - i\alpha Re[(U-c)(\frac{d^2\phi}{dy^2} - \alpha^2\phi) - \frac{d^2U}{dy^2}\phi] = 0. \tag{3.36}$$

For channel flow, the background velocity profile is:

$$U = 1 - y^2, \tag{3.37}$$

U is normalized with centerline velocity and y is normalized with half channel width. With boundary conditions $y = \pm 1, \phi = \phi' = 0$, equation (3.36) reduces to an eigenvalue problem. There are many well-established procedures to solve this eigenvalue problem [52,53]. By solving the OSE, the velocity perturbation $\phi(y)$ is obtained. The other velocity component $\psi(y)$ can also be calculated by the continuity relation. The eigenvalue c is also from the equation solution. The complex eigenvalue c indicates the temporal growth rate of perturbation modes. The eigenfunctions $\psi(y)$ and $\phi(y)$

provide the particular spatial shapes of the perturbation modes. The most unstable perturbation modes correspond to Tollmien-Schlichting (TS) waves. Following TS wave forms, the initial condition of the perturbation is introduced into our simulation. Two flow condition sets are considered in this work. For $Re = 30406, \alpha = \pi/4$, the most unstable mode has eigenvalue $c = 0.1734+0.009105i$. For $Re = 45458, \alpha = \pi/4$, the most unstable mode has eigenvalue $c = 0.1614 + 0.009788i$. Those corresponding eigenfunctions (ψ,ϕ) are obtained by solving the eigenvalue problem.

3.2 Simulation Cases

Temporal channel flow simulations of small perturbation evolution with a specified background velocity field are performed using the GKM. The Mach number range of the simulations is 0.08-7.2, and Reynolds number range is 30,000-230,000. The characteristic length is taken to be the channel half-width which is specified to be 0.020032m. The domain size along streamwise direction is considered as one wavelength of perturbation. The wavelength is taken to be eight times of the channel half-width. The background velocity field is parabolic and is sustained steady using streamwise body force or pressure gradient. While both techniques yielded identical results, body force approach was used in the final calculations for the high Mach number study as it enables the background thermodynamic state to be nearly steady. The background temperature increase due to viscous losses was found to be minimal and did not affect the outcome of the simulations even at high Mach numbers.

Two channel flow cases are examined in the low Mach number study and they are detailed in Table 3.1. The initial perturbation profile for the low Mach number study is chosen to be the most unstable wave mode of the OSE analysis. Simulations are performed for multiple perturbation velocity amplitudes: 0.1%, 0.5%, 2% of the background flow centerline velocity.

Table 3.1: Background flow conditions for low Mach number limit

	$U_0(m/s)$	$\rho(kg/m^3)$	$T(K)$	Re	M	grid$(x * y * z)$
Case1	30	1	353	30406	0.08	$160 \times 100 \times 4$
Case2	45	1	353	45458	0.12	$160 \times 100 \times 4$

Table 3.2: Background flow conditions for high Mach number limit

	$U_0(m/s)$	$\rho(kg/m^3)$	$T(K)$	Re	M	grid$(x * y * z)$
Case1	705.2	0.0189	61	65754	4.5	$160 \times 200 \times 4$
Case2	931.6	0.02	60	93900	6.0	$160 \times 200 \times 4$
Case3	1108.5	0.04	59	227763	7.2	$160 \times 200 \times 4$

The high Mach number study involves three cases for the flow conditions which are given in Table 3.2. Following the transition to turbulence study [20], the background velocity is taken to be parabolic in shape corresponding to a laminar flow. The PRE verification process admits any initial perturbation profile. Therefore, for the sake of simplicity, we use the low Mach number OSE solution as the perturbation profile. The streamwise wavelength and amplitude of the perturbation profile are also similar to that of the low Mach number study. In both low and high Mach number studies, the background thermodynamic field is uniform initially and evolves slowly with time. The grid resolutions are chosen based on grid convergence investigation.

3.3 Results: Analysis vs. Simulations

The results are presented in three parts. In the first part we compare the linear analysis-based evolution of perturbation kinetic energy at low and high Mach numbers. The second part focuses exclusively on the high Mach number limit. The analytical results are compared against DNS data. A similar comparison is performed

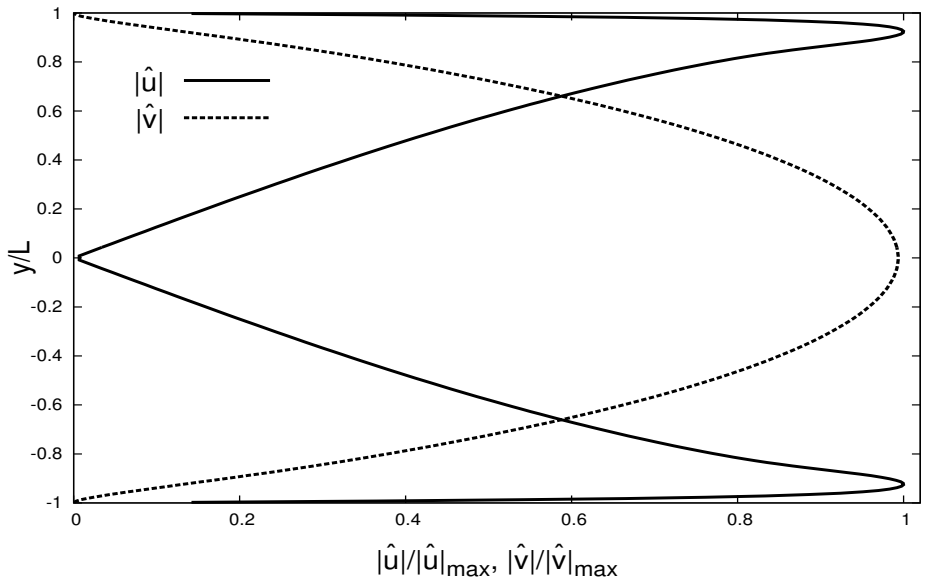

Figure 3.1: Profiles of perturbation velocity

in the third part, but at the low Mach number limit.

3.3.1 Analytical Results at High and Low Mach Number Limit

In DNS, the perturbation is initially superposed to the background laminar flow. The initial conditions for perturbation are from OSE eigensolution which provides the spatial distribution of perturbation modes. The initial velocity perturbation shapes are given in Figure 3.1. These perturbations are set to periodic along streamwise direction and the contours of initial perturbation are given by Figure 3.2.

At both Mach number extremes, the streamwise perturbation velocity dominates the contribution to the perturbation kinetic energy. In Figure 3.3, the streamwise perturbation kinetic energy evolution as computed from linear analyses at the two Mach number extremes are plotted. In the absence of pressure effects, the kinetic energy grows rather rapidly in the pressure-released high-Mach number limit. The low-Mach number OSE solution exhibits very slow growth. It is therefore reasonable to say that the action of Poisson pressure is to significantly diminish the growth rate,

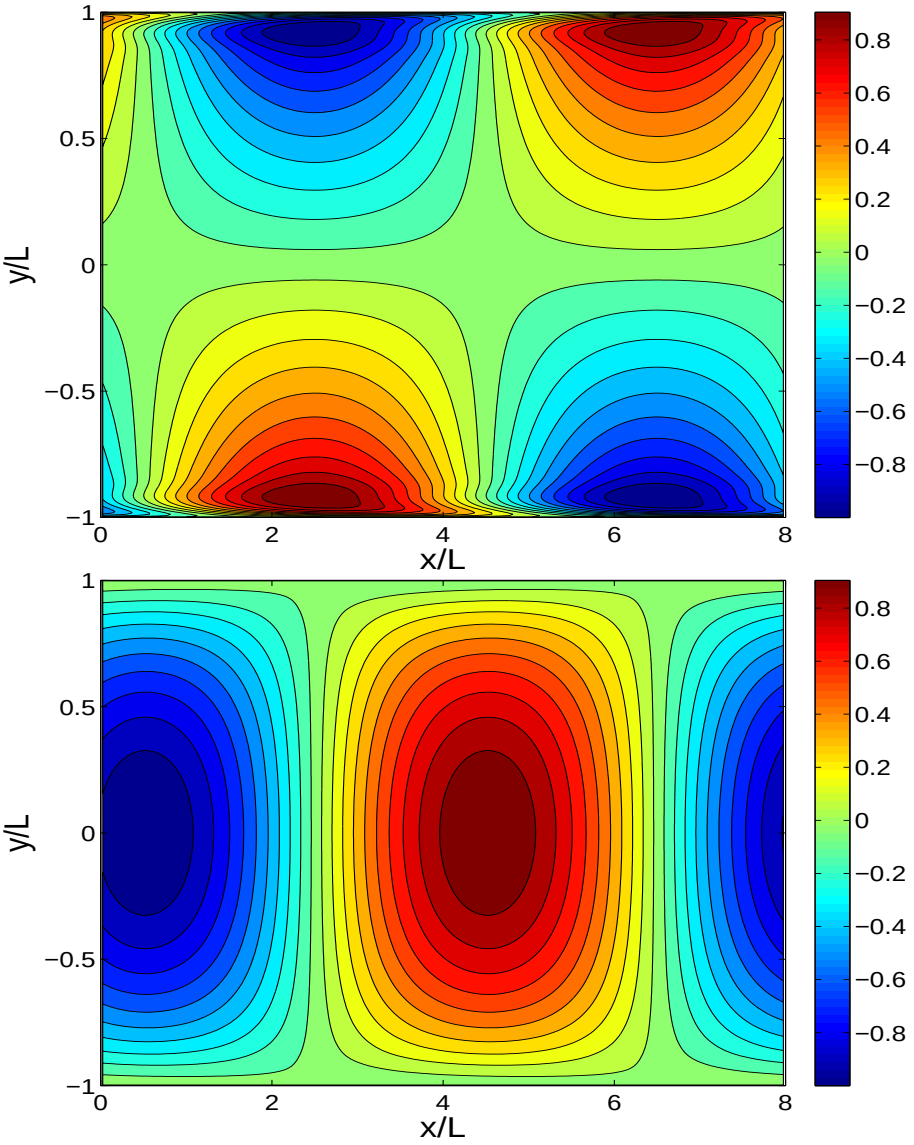

Figure 3.2: Contours of perturbation velocity: u/u_{max}(top) and v/v_{max}(bottom)

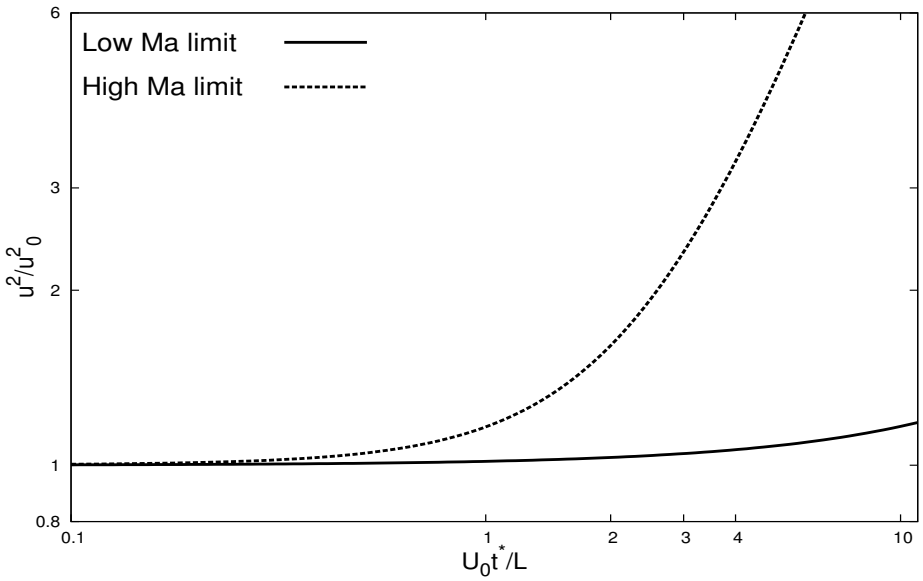

Figure 3.3: Comparison of streamwise kinetic energy from linear analyses at high and low Mach number limit (low Mach number 0.12)

when compared to the pressure-released equation. This is consistent with the findings of Mishra et al. [36] for homogeneous shear (Couette) flows. But it is important to note that the pressure-released effect will not last indefinitely and consequently, the linear PRE may be valid only for a finite period of time. This will be examined by comparing linear PRE against DNS data in the next sub-section.

3.3.2 High Mach Number Limit: DNS vs. PRE

In Figure 3.4, we compare the linear-PRE results against DNS data at different Mach numbers. Non-linear and viscous effects are present in DNS computations. The solid line in Figure 3.4(a) represents the analytical PRE result obtained from squaring and integrating equation (3.25). The DNS results of various Mach numbers are shown with symbols. Clearly, the agreement is excellent at early times. It is evident that the larger Mach number simulations follow the asymptotic analytical behavior for a longer period of time as anticipated in [18]. Next we examine the

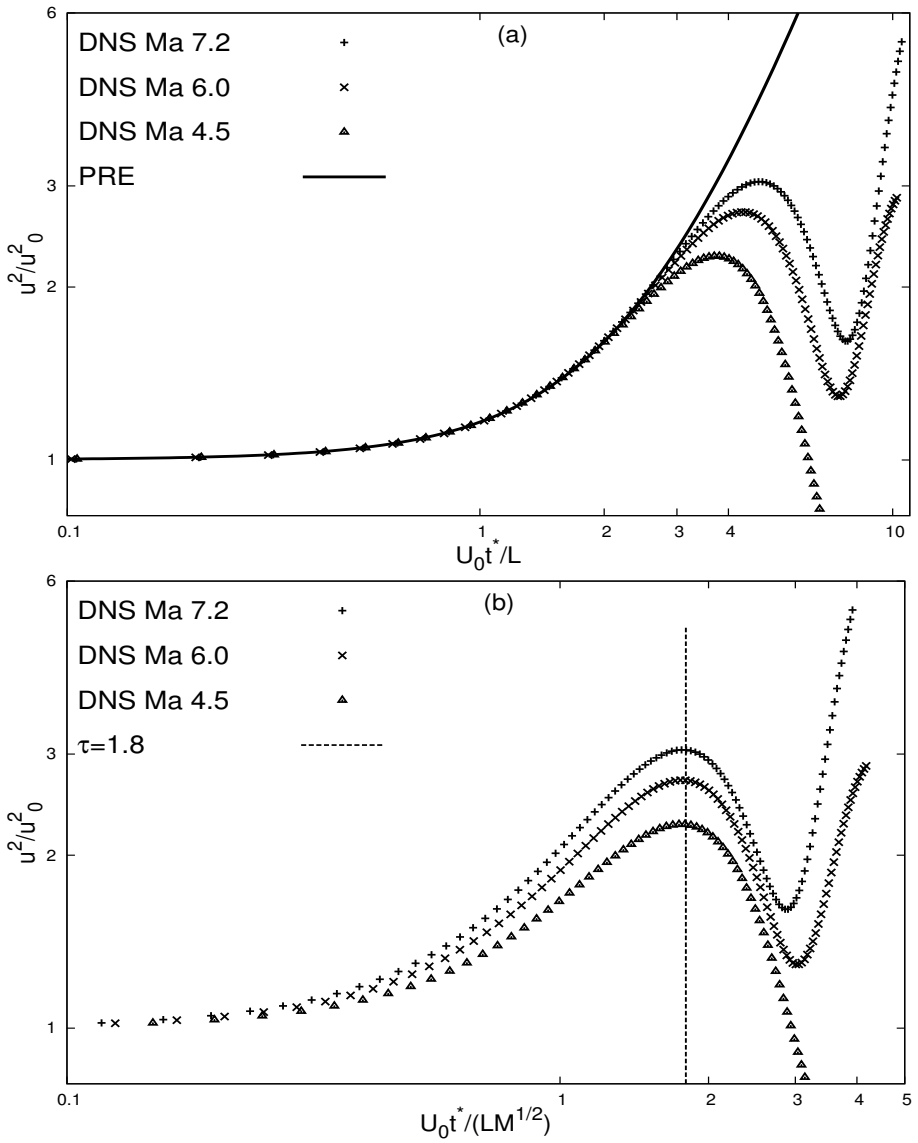

Figure 3.4: DNS vs. PRE for streamwise kinetic energy evolution:(a)shear time and (b)mixed time

precise duration over which the PRE formulation is valid in Figure 3.4(b). Clearly the departure of DNS solution from PRE occurs at the estimated time τ which has approximate value 1.8, same as in [18]. Beyond this time, pressure effects begin to influence the flow field.

In the PRE analysis, the perturbation velocity field is a strong function of the

wall-normal coordinate y. It is therefore important to verify whether the streamwise and wall-normal perturbation velocity profiles are captured by DNS. In Figure 3.5, we compare the streamwise perturbation velocity u profile obtained from DNS data at different lapse times against PRE solution at the corresponding times. Only Mach 6 case results are shown as other cases show similar behaviors. The DNS (Mach 6) results match the PRE solution at nearly all locations at all times. The numerical and analytical profiles show a small but discernible difference at the peak u locations. This observation can be attributed to the fact that peak u values occur in regions of very steep second derivatives. In these peak regions, viscous effects (second derivative) dominate over inertial effects (first derivative). Thus the inviscid PRE solution is slightly different from the full-physics DNS solution. Comparison of DNS and PRE wall-normal perturbation velocity v profiles at different elapsed times are given in Figure 3.6. The PRE analysis indicates that this profile is invariant in time. The DNS solutions do indeed capture this time-independence. Overall, it is evident that the computational scheme represents the physics of pressure-released limit accurately over the initial stages of perturbation growth, further the duration over which the DNS results are consistent with PRE is similar to that in homogeneous shear flows [17] at high Mach number limit.

3.3.3 Low Mach Number Limit: DNS vs. OSE

While PRE represents the asymptotic limit of pressure being too slow to modify the velocity field evolution, incompressible flow represents the opposite extreme in which pressure acts instantly to keep the velocity field divergence free at all times. We will now investigate if DNS captures the linear evolution of small perturbations as dictated by the Orr-Sommerfeld equation (OSE).

We commence with a comparison of DNS and OSE velocity field evolution. The

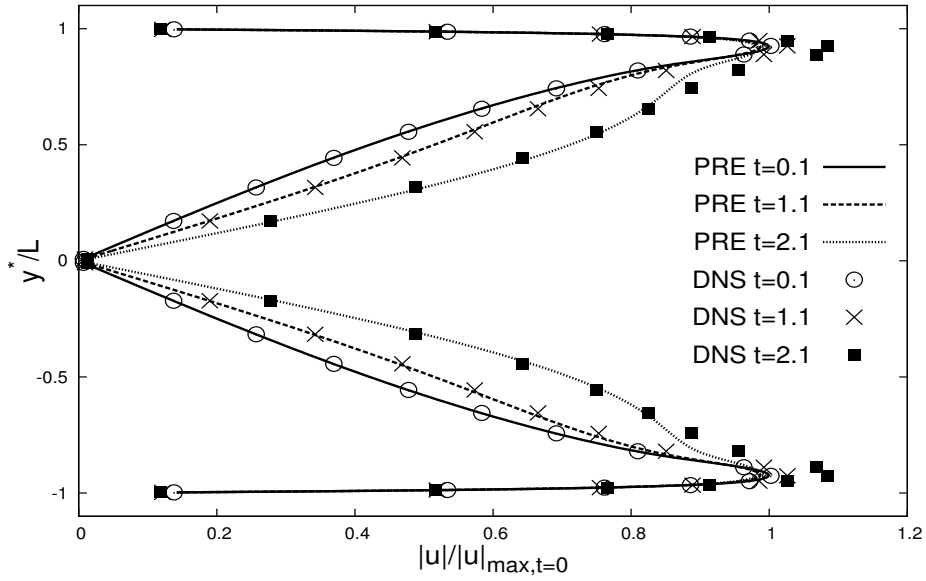

Figure 3.5: Perturbation velocity u profile evolution with time at Ma=6: t=$U_0 t^*/L$

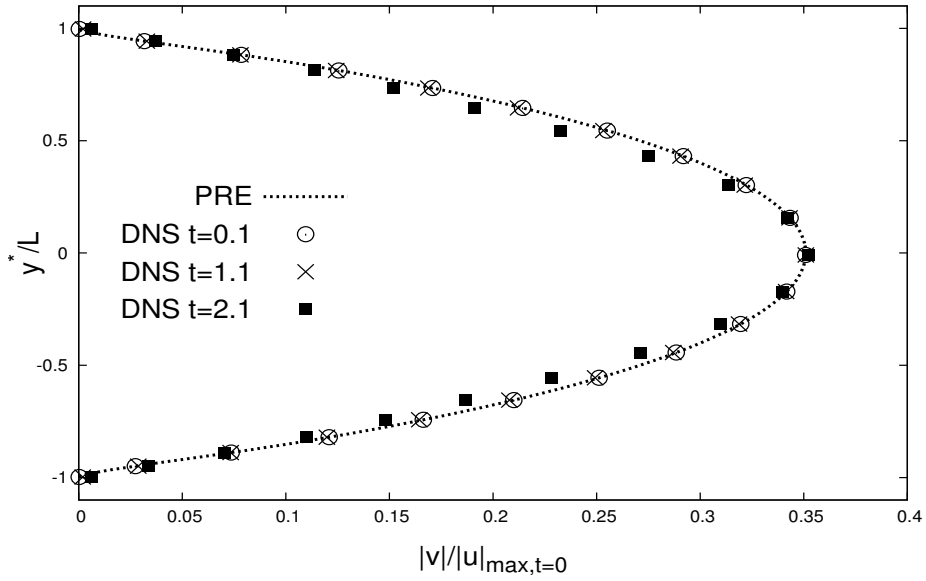

Figure 3.6: Perturbation velocity v profile evolution with time at Ma=6: t=$U_0 t^*/L$

DNS at two incompressible Mach numbers performed with different initial perturbation amplitudes are plotted along with OSE solutions in Figure 3.7. Figure 3.7(a) shows Case 1 for which Reynolds and Mach numbers are 30408 and 0.08 respectively. The streamwise perturbation velocity magnitude maximas at different wall-normal distances in DNS solution are considered. The maxima evolution for three initial intensities (0.1%, 0.5%, 2%) is found to follow the linear analysis result very closely at the early stages before nonlinear effects begin to appear. Here the time is normalized by characteristic length and initial background flow centerline velocity. In Figure 3.7(b), Case 2 (Re= 45458, and Ma= 0.12) is examined. In this plot the square root of volume-averaged kinetic energy is considered. Once again excellent agreement between DNS results and OSE solution is seen irrespective of the initial perturbation intensity.

Next we compare the evolution of streamwise perturbation velocity u and wall-normal perturbation velocity v profiles in Figures 3.8 and 3.9. Only the Ma=0.12 (Re=45458) results are provided as both Mach number cases yield identical outcomes. Since the OSE solution adopts normal mode form as (3.33) and (3.34) whose spatial and time dependency are separate, the normalized profiles of both u and v must be invariant in time. Indeed, DNS solution preserves the normal mode shape accurately.

3.4 Summary and Conclusion

We develop a linear pressure-released equation (PRE) analysis to describe the stability of very high Mach number Poiseuille flow. The PRE and Orr-Sommerfeld analysis are compared against Poiseuille flow DNS results at extreme Mach numbers. The DNS employs the Gas-Kinetic Method (GKM) to study small perturbation evolution in channel flows over a range of Mach and Reynolds numbers. The agreement between numerical simulations and linear analysis is very encouraging. Overall the

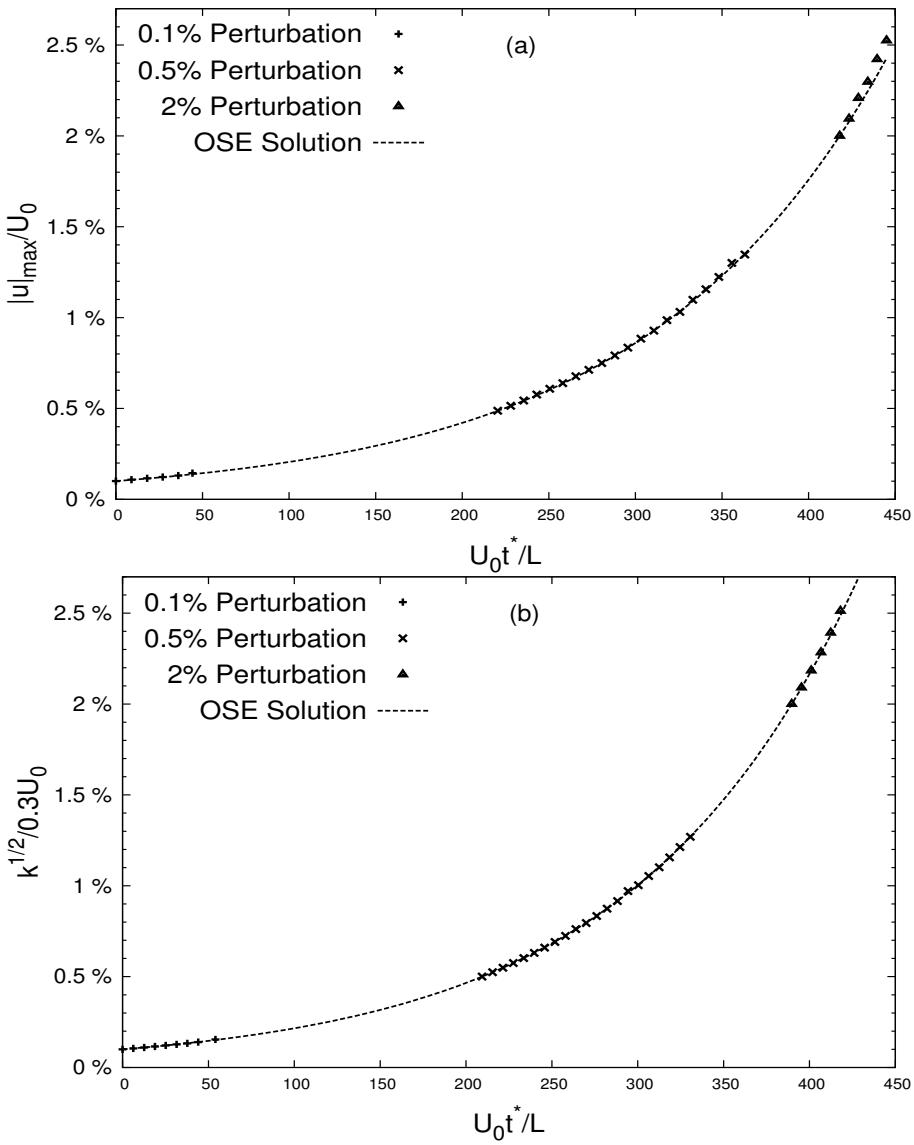

Figure 3.7: Comparison of perturbation growth rate:(a)Ma=0.08 and (b)Ma=0.12

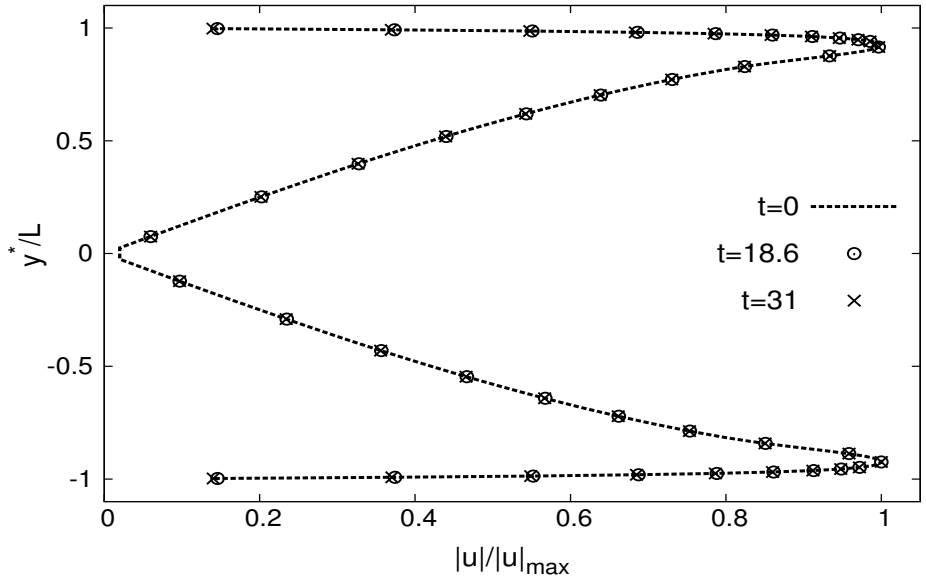

Figure 3.8: Time evolution of perturbation velocity u profile at Ma=0.12: t=$U_0 t^*/L$

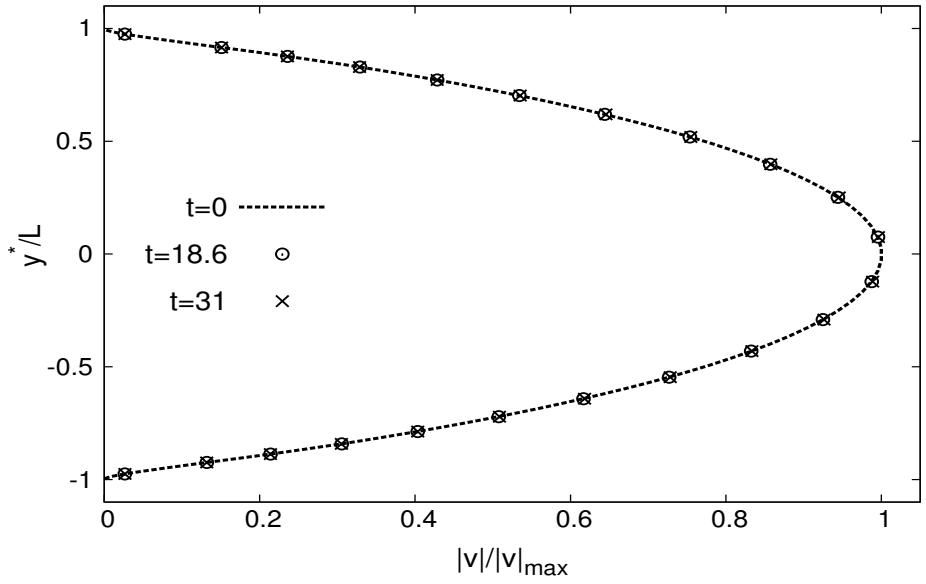

Figure 3.9: Time evolution of perturbation velocity v profile at Ma=0.12: t=$U_0 t^*/L$

present study reveals the physical accuracy and numerical viability of GKM approach for simulating wall-bounded flow instabilities over a large Mach number range. The importance of PRE for describing wall-bounded non-uniform shear flow at early stage of evolution is firmly established. The work in this study is published in [54].

4. INSTABILITY OF POISEUILLE FLOW AT INTERMEDIATE MACH NUMBERS

We now investigate the stability characteristics of small perturbation evolution in high-speed channel flow at intermediate Mach numbers. Specifically, we investigate the influence of perturbation obliqueness and Mach number on stability. This study employs linear analysis and DNS. The linear analysis solves an initial value problem, rather than an eigenvalue problem, to establish the various stages of perturbation evolution. The corresponding temporal-DNS is performed using the Gas Kinetic Method (GKM). The GKM solver has been well validated by [16, 23] and in previous sections. The base velocity field is taken to be parabolic. This velocity field is sustained using either a pressure gradient or a body force. Temporal channel flow simulations are performed starting from imposed two and three-dimensional perturbations. To contrast incompressible and compressible flow characteristics, normal modes of the incompressible channel flow with modifications are used as the initial perturbations at all speed regime. This is similar to the initial condition used by other investigators [20] to examine breakdown to turbulence in compressible channel flow. To establish the generality of the influence, other mode shapes are also used for the initial perturbations.

4.1 Governing Equations and Linear Analysis

The compressible Navier-Stokes equations along with ideal-gas assumption form the basis of the analysis in this study. It is given in equations (2.1), (2.2), (2.3) and (2.4).

4.1.1 Linear Analysis

The flow field is decomposed into base flow and perturbations. The decomposition is given by:

$$\rho^* = \bar{\rho} + \rho', \tag{4.1}$$

$$u_i^* = \bar{U}_i + u_i', \tag{4.2}$$

$$p^* = \bar{P} + p'. \tag{4.3}$$

Base flow satisfies the governing equations and stays nearly stationary over the duration of the analysis. The base flow is plane Poiseuille flow with a parallel velocity profile:

$$\bar{U}_i = (\bar{U}_1(x_2), 0, 0). \tag{4.4}$$

The perturbation field is fully three-dimensional and is given by:

$$u_i' = (u_1', u_2', u_3'). \tag{4.5}$$

We consider small initial perturbations so that the non-linear terms in perturbation equations can be neglected in the analysis. Here, x_1 is defined as streamwise direction, x_2 is wall-normal direction and x_3 is span-wise direction.

By subtracting base flow equations from those of total flow, the linearized per-

turbation equations can be obtained:

$$\frac{\partial u_1'}{\partial t} + \bar{U}_1 \frac{\partial u_1'}{\partial x_1} = -\frac{1}{\bar{\rho}} \frac{\partial p'}{\partial x_1} - u_2' \frac{\partial \bar{U}_1}{\partial x_2} + \frac{\mu}{\bar{\rho}} \left(\frac{\partial^2 u_1'}{\partial x_k \partial x_k} - \frac{1}{9} \frac{\partial^2 u_k'}{\partial x_1 \partial x_k} \right), \tag{4.6}$$

$$\frac{\partial u_2'}{\partial t} + \bar{U}_1 \frac{\partial u_2'}{\partial x_1} = -\frac{1}{\bar{\rho}} \frac{\partial p'}{\partial x_2} + \frac{\mu}{\bar{\rho}} \left(\frac{\partial^2 u_2'}{\partial x_k \partial x_k} - \frac{1}{9} \frac{\partial^2 u_k'}{\partial x_2 \partial x_k} \right), \tag{4.7}$$

$$\frac{\partial u_3'}{\partial t} + \bar{U}_1 \frac{\partial u_3'}{\partial x_1} = -\frac{1}{\bar{\rho}} \frac{\partial p'}{\partial x_3} + \frac{\mu}{\bar{\rho}} \left(\frac{\partial^2 u_3'}{\partial x_k \partial x_k} - \frac{1}{9} \frac{\partial^2 u_k'}{\partial x_3 \partial x_k} \right), \tag{4.8}$$

$$\frac{\partial p'}{\partial t} + \bar{U}_1 \frac{\partial p'}{\partial x_1} = -\bar{P}\gamma \left(\frac{\partial u_1'}{\partial x_1} + \frac{\partial u_2'}{\partial x_2} + \frac{\partial u_3'}{\partial x_3} \right) + o(\mu). \tag{4.9}$$

Here $o(\mu)$ is the viscous term in linearized perturbation pressure equation. From the velocity field, the linearized perturbation vorticity equations can be obtained:

$$\begin{aligned} \frac{\partial w_1'}{\partial t} + \bar{U}_1 \frac{\partial w_1'}{\partial x_1} = {} & \frac{1}{\bar{\rho}^2} \frac{\partial \bar{\rho}}{\partial x_2} \frac{\partial p'}{\partial x_3} - \frac{\partial \bar{U}_1}{\partial x_2} \frac{\partial u_3'}{\partial x_1} - \frac{\mu}{\bar{\rho}^2} \frac{\partial \bar{\rho}}{\partial x_2} \left(\frac{\partial^2 u_3'}{\partial x_k \partial x_k} - \frac{1}{9} \frac{\partial^2 u_k'}{\partial x_3 \partial x_k} \right) \\ & + \frac{\mu}{\bar{\rho}} \left(\frac{\partial^3 u_3'}{\partial x_k \partial x_k \partial x_2} - \frac{\partial^3 u_2'}{\partial x_k \partial x_k \partial x_3} \right), \end{aligned} \tag{4.10}$$

$$\frac{\partial w_2'}{\partial t} + \bar{U}_1 \frac{\partial w_2'}{\partial x_1} = -\frac{\partial \bar{U}_1}{\partial x_2} \frac{\partial u_2'}{\partial x_3} + \frac{\mu}{\bar{\rho}} \left(\frac{\partial^3 u_1'}{\partial x_k \partial x_k \partial x_3} - \frac{\partial^3 u_3'}{\partial x_k \partial x_k \partial x_1} \right), \tag{4.11}$$

$$\begin{aligned} \frac{\partial w_3'}{\partial t} + \bar{U}_1 \frac{\partial w_3'}{\partial x_1} = {} & \frac{1}{\bar{\rho}^2} \frac{\partial \bar{\rho}}{\partial x_2} \frac{\partial p'}{\partial x_1} - \frac{\partial \bar{U}_1}{\partial x_2} \left(\frac{\partial u_1'}{\partial x_1} + \frac{\partial u_2'}{\partial x_2} \right) - \frac{\mu}{\bar{\rho}^2} \frac{\partial \bar{\rho}}{\partial x_2} \left(\frac{\partial^2 u_1'}{\partial x_k \partial x_k} - \frac{1}{9} \frac{\partial^2 u_k'}{\partial x_1 \partial x_k} \right) \\ & + \frac{\mu}{\bar{\rho}} \left(\frac{\partial^3 u_2'}{\partial x_k \partial x_k \partial x_1} - \frac{\partial^3 u_1'}{\partial x_k \partial x_k \partial x_2} \right) + u_2' \frac{\partial^2 \bar{U}_1}{\partial x_2 \partial x_2}, \end{aligned} \tag{4.12}$$

In span-wise perturbation vorticity (w_3) equation (4.12), multiple instability mechanisms can be identified. On the right side of equation(4.12), the first term $\frac{1}{\bar{\rho}^2} \frac{\partial \bar{\rho}}{\partial x_2} \frac{\partial p'}{\partial x_1}$ represents the baroclinic effect, the second term $\frac{\partial \bar{U}_1}{\partial x_2} \left(\frac{\partial u_1'}{\partial x_1} + \frac{\partial u_2'}{\partial x_2} \right)$ represents compressible vortex production, the third and fourth terms are viscous effect and the last term $u_2' \frac{\partial^2 \bar{U}_1}{\partial x_2 \partial x_2}$ is the second derivative effect. The same span-wise vorticity equation in the incompressible flow regime only contains the second derivative term and

viscous effect term. In compressible flow linear analysis, the viscous effect plays a less prominent role than the pressure-velocity interactions. Therefore, we focus on the inviscid perturbation equations:

$$\frac{\partial u_1'}{\partial t} + \bar{U}_1 \frac{\partial u_1'}{\partial x_1} = -\frac{1}{\bar{\rho}} \frac{\partial p'}{\partial x_1} - u_2' \frac{\partial \bar{U}_1}{\partial x_2}, \tag{4.13}$$

$$\frac{\partial u_2'}{\partial t} + \bar{U}_1 \frac{\partial u_2'}{\partial x_1} = -\frac{1}{\bar{\rho}} \frac{\partial p'}{\partial x_2}, \tag{4.14}$$

$$\frac{\partial u_3'}{\partial t} + \bar{U}_1 \frac{\partial u_3'}{\partial x_1} = -\frac{1}{\bar{\rho}} \frac{\partial p'}{\partial x_3}, \tag{4.15}$$

$$\frac{\partial p'}{\partial t} + \bar{U}_1 \frac{\partial p'}{\partial x_1} = -\bar{P}\gamma \left(\frac{\partial u_1'}{\partial x_1} + \frac{\partial u_2'}{\partial x_2} + \frac{\partial u_3'}{\partial x_3} \right). \tag{4.16}$$

To demarcate the perturbation wave mode's shift from its own growth or decay, the perturbation equations are considered in a coordinate frame moving with base flow. The coordinate frame transformation is given by:

$$X_1 = x_1 - \int_0^t \bar{U}_1 dt, \tag{4.17}$$

$$X_2 = x_2, \tag{4.18}$$

$$X_3 = x_3, \tag{4.19}$$

$$t = t. \tag{4.20}$$

Perturbation equations in the new frame are given as:

$$\frac{du_1'}{dt} = -\frac{1}{\bar{\rho}}\frac{\partial p'}{\partial X_1} - u_2'\frac{\partial \bar{U}_1}{\partial x_2}, \tag{4.21}$$

$$\frac{du_2'}{dt} = -\frac{1}{\bar{\rho}}\frac{\partial p'}{\partial X_2} + \frac{1}{\bar{\rho}}\frac{\partial p'}{\partial X_1}\int_0^t \frac{\partial \bar{U}_1}{\partial x_2}dt, \tag{4.22}$$

$$\frac{du_3'}{dt} = -\frac{1}{\bar{\rho}}\frac{\partial p'}{\partial X_3}, \tag{4.23}$$

$$\frac{dp'}{dt} = -\bar{P}\gamma\left(\frac{\partial u_1'}{\partial X_1} + \frac{\partial u_2'}{\partial X_2} - \frac{\partial u_2'}{\partial X_1}\int_0^t \frac{\partial \bar{U}_1}{\partial x_2}dt + \frac{\partial u_3'}{\partial X_3}\right). \tag{4.24}$$

Based on the flow homogeneity in streamwise (X_1) and span-wise (X_3) directions, the perturbation is introduced in the normal mode forms:

$$u_1' = \hat{u}_1(X_2,t)e^{i(\kappa_1 X_1 + \kappa_3 X_3)}, \tag{4.25}$$

$$u_2' = \hat{u}_2(X_2,t)e^{i(\kappa_1 X_1 + \kappa_3 X_3)}, \tag{4.26}$$

$$u_3' = \hat{u}_3(X_2,t)e^{i(\kappa_1 X_1 + \kappa_3 X_3)}, \tag{4.27}$$

$$p' = \hat{p}(X_2,t)e^{i(\kappa_1 X_1 + \kappa_3 X_3)}. \tag{4.28}$$

Here, hat represents the complex mode amplitude and κ_1&κ_3 are spatial wave numbers. With these mode forms implemented into perturbation equations, the perturbation mode magnitude equations are given as:

$$\frac{d\hat{u}_1}{dt} = -\frac{1}{\bar{\rho}}i\kappa_1\hat{p} - \hat{u}_2\frac{\partial \bar{U}_1}{\partial x_2}, \tag{4.29}$$

$$\frac{d\hat{u}_2}{dt} = -\frac{1}{\bar{\rho}}\frac{\partial \hat{p}}{\partial X_2} + \frac{1}{\bar{\rho}}i\kappa_1\hat{p}\int_0^t \frac{\partial \bar{U}_1}{\partial x_2}dt, \tag{4.30}$$

$$\frac{d\hat{u}_3}{dt} = -\frac{1}{\bar{\rho}}i\kappa_3\hat{p}, \tag{4.31}$$

$$\frac{d\hat{p}}{dt} = -\bar{P}\gamma \left[i\kappa_1 \hat{u}_1 + \frac{\partial \hat{u}_2}{\partial X_2} - i\kappa_1 \hat{u}_2 \int_0^t \frac{\partial \bar{U}_1}{\partial x_2} dt + i\kappa_3 \hat{u}_3 \right]. \tag{4.32}$$

Inspection of equations (4.30) and (4.32) suggests that time integrated terms dominate the perturbation evolution at long times. It is evident that pressure interacts most strongly with the wall-normal velocity u_2. At long times, this interaction is described by:

$$\frac{d\hat{u}_2}{dt} \sim \frac{1}{\bar{\rho}} i\kappa_1 \hat{p} \int_0^t \frac{\partial \bar{U}_1}{\partial x_2} t, \tag{4.33}$$

$$\frac{d\hat{p}}{dt} \sim \bar{P}\gamma i\kappa_1 \hat{u}_2 \int_0^t \frac{\partial \bar{U}_1}{\partial x_2} t, \tag{4.34}$$

Evidently, p' and u_2' are coupled as in a harmonic oscillator. In such a case, energy must be equi-partitioned between these two perturbation components. Similar findings have been reported in other flows such as homogeneous shear [18, 23]. Later in this study, DNS results will be scrutinized for this equi-partition.

Most importantly, the pressure-velocity interaction does not require the presence of a second derivative in the background velocity field. At this stage we isolate the linear and quadratic effects of the background velocity field. In incompressible flow, the quadratic nature of the profile leads to the Tollmien-Schlichting instability. In compressible flows, the nature of the pressure field is established by the linear part of the flow field. Our goal is to examine the influence of the compressible pressure field on the TS wave instability.

First we examine the nature of the pressure field by simplifying the background field to be locally linear.

$$\frac{\partial \bar{U}_1}{\partial x_2}(x_2) \approx S = constant, \tag{4.35}$$

Clearly, neglecting the second derivative will have some consequences. The validity of this simplification will be assessed later by comparing analytical results against

DNS data.

4.1.1.1 Uniform Shear Initial Value Analysis

Under the assumption of uniform shear flow, the mode forms can be written as:

$$u_1' = \hat{u}_1(t)e^{i(\kappa_1 X_1+\kappa_2 X_2+\kappa_3 X_3)}, \tag{4.36}$$

$$u_2' = \hat{u}_2(t)e^{i(\kappa_1 X_1+\kappa_2 X_2+\kappa_3 X_3)}, \tag{4.37}$$

$$u_3' = \hat{u}_3(t)e^{i(\kappa_1 X_1+\kappa_2 X_2+\kappa_3 X_3)}, \tag{4.38}$$

$$p' = \hat{p}(t)e^{i(\kappa_1 X_1+\kappa_2 X_2+\kappa_3 X_3)}. \tag{4.39}$$

The velocity and pressure equations simplify to

$$\frac{d\hat{u}_1}{dt} = -\frac{1}{\bar{\rho}} i\kappa_1 \hat{p} - \hat{u}_2 S, \tag{4.40}$$

$$\frac{d\hat{u}_2}{dt} = -\frac{1}{\bar{\rho}} \frac{\partial \hat{p}}{\partial X_2} + \frac{1}{\bar{\rho}} i\kappa_1 \hat{p} \int_0^t S dt, \tag{4.41}$$

$$\frac{d\hat{u}_3}{dt} = -\frac{1}{\bar{\rho}} i\kappa_3 \hat{p}, \tag{4.42}$$

$$\frac{d\hat{p}}{dt} = -\bar{P}\gamma \left[i\kappa_1 \hat{u}_1 + \frac{\partial \hat{u}_2}{\partial X_2} - i\kappa_1 \hat{u}_2 \int_0^t S dt + i\kappa_3 \hat{u}_3 \right]. \tag{4.43}$$

Given $\hat{u}_i(0)$ and $\hat{p}(0)$, we now seek the perturbation evolution. The equations (4.40), (4.41), (4.42) and (4.43), and solution mode forms (4.36), (4.37), (4.38) and (4.39), are now similar to that in a homogeneous shear flows [23]. Following the derivation in [17], the pressure evolution equation can be written as:

$$\frac{d^3\hat{p}}{dt^3} = -a^2 S^2 \kappa^2(0) cos^2\beta (t^2 \frac{d\hat{p}}{dt} + 4t\hat{p}), \tag{4.44}$$

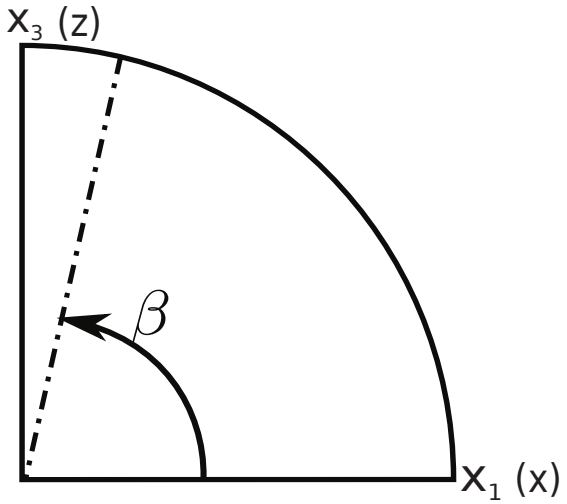

Figure 4.1: The orientation angle of oblique modes

Here $\hat{p}$ is the Fourier amplitude of pressure perturbation, a is speed of sound and $\kappa(0)$ is the initial wave number and β is the obliqueness angle of a typical wave vector shown in Figure 4.1.

In the linear analysis for homogeneous shear flows [18, 23], it is shown that the velocity field is significantly influenced by pressure effects which are closely related to the perturbation orientation. For oblique modes, new parameters are defined such as effective shear and effective Mach number. With the oblique wave vector, the effective shear, S^*, experienced by a perturbation is given by:

$$S^* = Scos(\beta). \tag{4.45}$$

The effective Mach number experienced by a perturbation mode, M^*, defined as:

$$M^* = \frac{S^*}{\kappa(0)a} = M_0 cos(\beta), \tag{4.46}$$

where M_0 is the reference Mach number. This is the Mach number experienced by a

streamwise ($\beta = 0°$) mode.

With the effective parameters, the pressure perturbation in equation (4.44) yields a self-similar form of:

$$\frac{d^3\hat{p}}{dt^{*3}} = -\left(t^{*2}\frac{d\hat{p}}{dt^*} + 4t^*\hat{p}\right), \tag{4.47}$$

The normalized time is defined as:

$$t^* = \frac{S^*t}{\sqrt{M^*}}. \tag{4.48}$$

Crucial inferences can be drawn from the self-similar behavior of pressure equation:

1. The effective Mach number M^* of a perturbation mode, rather than the reference Mach number M_0, is more suitable to characterize the behavior of pressure.

2. In terms of normalized variables, the behavior of pressure is independent of obliqueness angle.

3. There should exists a critical obliqueness angle β_c which experiences unit effective Mach number.
$$\beta_c = cos^{-1}(\frac{1}{M_0}). \tag{4.49}$$

4. The critical angle demarcates the perturbation-orientation space into two regions: supersonic region and subsonic region. All modes with $\beta < \beta_c$ are classified as supersonic as their effective Mach number is greater than unity. Modes with $\beta > \beta_c$ are identified as subsonic modes.

5. Streamwise ($\beta = 0°$) modes experience the highest effective Mach number whereas span-wise modes experience nearly zero effective Mach number.

In the compressible homogeneous shear flow, [17] shows that all supersonic modes are stable and all subsonic modes are unstable. The schematic stability map for

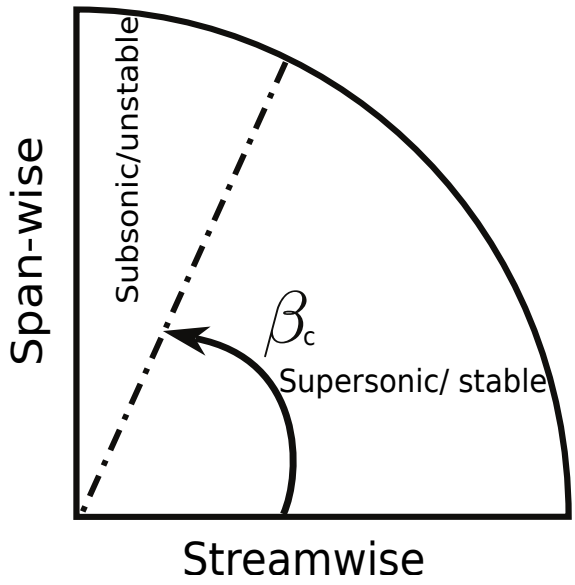

Figure 4.2: Schematic of modal stability for compressible homogeneous shear flow

compressible homogeneous shear flow is given in Figure 4.2. In this study, we will use DNS to examine how obliqueness affects the flow stability in Poiseuille flow.

4.1.1.2 Non-uniform Shear Effect

The consequence of non-uniform shear is now examined using the span-wise vorticity equation:

$$\begin{aligned}\frac{\partial w_3'}{\partial t} + \bar{U}_1\frac{\partial w_3'}{\partial x_1} &= \frac{1}{\bar{\rho}^2}\frac{\partial \bar{\rho}}{\partial x_2}\frac{\partial p'}{\partial x_1} - \frac{\partial \bar{U}_1}{\partial x_2}\left(\frac{\partial u_1'}{\partial x_1} + \frac{\partial u_2'}{\partial x_2}\right) - \frac{\mu}{\bar{\rho}^2}\frac{\partial \bar{\rho}}{\partial x_2}\left(\frac{\partial^2 u_1'}{\partial x_k \partial x_k} - \frac{1}{9}\frac{\partial^2 u_k'}{\partial x_1 \partial x_k}\right) \\ &\quad + \frac{\mu}{\bar{\rho}}\left(\frac{\partial^3 u_2'}{\partial x_k \partial x_k \partial x_1} - \frac{\partial^3 u_1'}{\partial x_k \partial x_k \partial x_2}\right) + u_2'\frac{\partial^2 \bar{U}_1}{\partial x_2 \partial x_2}, \end{aligned} \tag{4.50}$$

The inhomogeneous effect is incumbent in the term $u_2'\frac{\partial^2 \bar{U}_1}{\partial x_2 \partial x_2}$ and viscous terms. In the low-speed regime, these terms yield the Tollmien-Schlichting instability and the second derivative term is the major contributing effect in the span-wise vorticity equation. However, in high-speed flow as depicted in equation (4.50), baroclinic

term $\frac{1}{\bar{\rho}^2}\frac{\partial \bar{\rho}}{\partial x_2}\frac{\partial p'}{\partial x_1}$ and compressible vorticity production term $\frac{\partial \bar{U}_1}{\partial x_2}\left(\frac{\partial u_1'}{\partial x_1}+\frac{\partial u_2'}{\partial x_2}\right)$ appear, and influence the evolution of span-wise vorticity at compressible flow regime. In the later DNS discussion, these three terms will be examined.

4.2 Numerical Simulations

The computational domain is a rectangular box of dimension ratio 4 : 1 along $x(x_1)$ and $y(x_2)$ directions. Along $z(x_3)$ direction, the box length depends upon the mode under consideration. Grid cells are uniformly distributed along x and z direction, but along wall-normal direction (y) geometric distribution is applied. The convergence study for grid resolution and time step is performed as shown in Figures 2.8, 2.9, 2.10, 2.11, 2.12 and 2.13. Excellent grid and time step convergence have been obtained.

The details of simulation cases are given in Table 3.2. U_0 is the initial base flow velocity at the centerline, ρ is the initial base flow density and T is the initial base flow temperature. Reynolds and Mach numbers are based on these base flow quantities and length scale. The magnitude of velocity perturbation is set to 0.5% of the value of centerline base velocity. Periodic boundary conditions are applied in x and z direction. In y direction, no-slip and no-penetration walls are applied. Both adiabatic and isothermal conditions for temperature are examined. It is found that both temperature boundary conditions yield similar perturbation evolutions although the base temperature and density profiles may be slightly different. The results discussed in this study are based on the isothermal wall condition.

4.3 Single Mode Perturbation

We first present the DNS simulation results of single perturbation mode evolution. The effect of mode orientation and base flow Mach number on single mode evolution is examined. A set of modes of different obliqueness angles are investigated to examine

stability characteristics in this high-speed Poiseuille flow. Three Mach numbers are examined to demonstrate Mach number effect on mode evolution.

4.3.1 Single Mode Perturbation in Incompressible Poiseuille Flow

For incompressible wall-bounded flow, Tollmien-Schlichting instability is well-known from linear stability theory. In this work, the obliqueness angle $\beta = 0°$ represents TS instability wave. In present DNS, the growth of TS wave is accurately captured and good agreement is reached between DNS and linear theory prediction. The kinetic energy evolution of TS wave mode at incompressible limit (Ma=0.08) is given in Figure 4.3. In Figure 4.3, kinetic energy evolution of other different obliqueness angles are also given. It is observed that for $\beta = 90°$, the perturbation evolution exhibits extremely rapid growth. This mode grows more rapidly than TS wave mode. Perturbation modes with intermediate angles also demonstrate growing evolution at this low-speed limit. The growth rate of intermediate angle modes is confined by the two limits: $\beta = 0°$ and $\beta = 90°$. Overall, perturbation modes with all obliqueness angles exhibit persistent growth behavior in this low-speed Poiseuille flow. To summarize the mode behavior in incompressible flow limit, an instability schematic map is proposed in Figure 4.4. For all perturbation modes with different obliqueness angles, persistent growth is observed. Instability feature is identified for all modes. This instability behavior is also dependent on the obliqueness angle. As to $\beta = 90°$, the most unstable evolution is observed. With increase in Mach number, this instability feature in Figure 4.4 is affected by compressibility effect. To further analyze the compressibility effect on perturbation evolution, we focus on the mode evolution with different obliqueness angles under several Mach numbers in the next discussion.

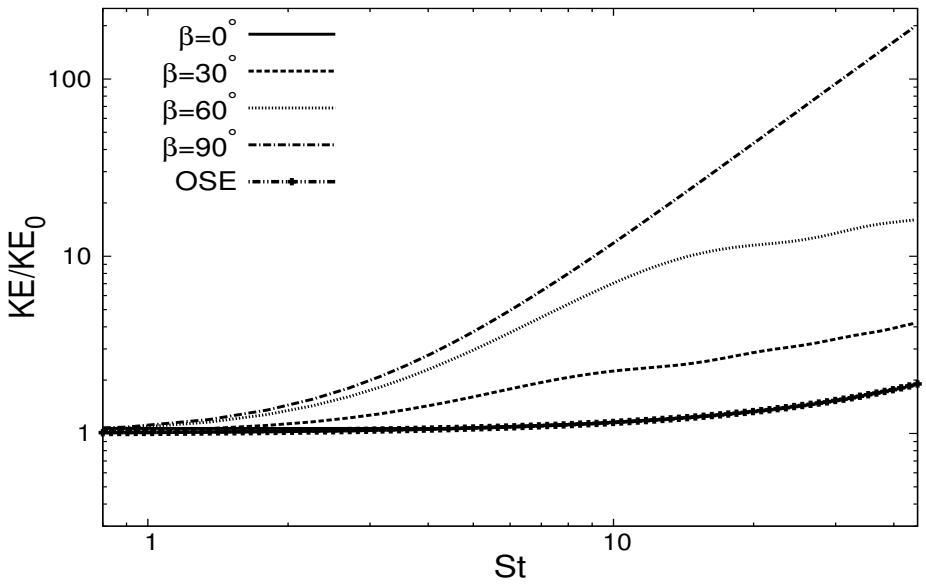

Figure 4.3: Kinetic energy evolution of oblique modes at Mach=0.08

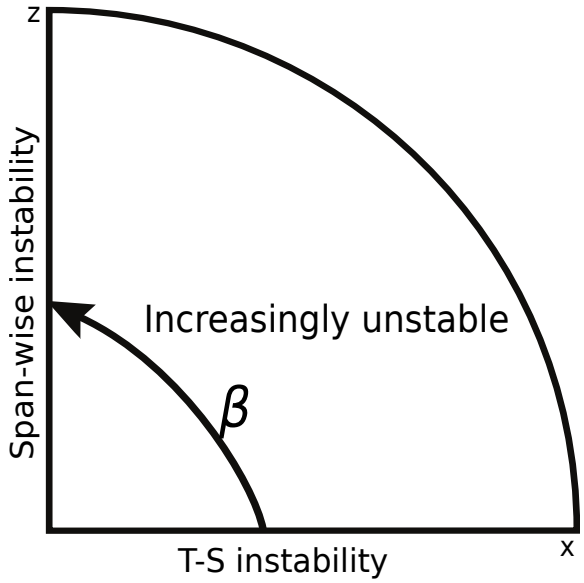

Figure 4.4: Stability map for incompressible Poiseuille flow

4.3.2 Single Mode Perturbation in Compressible Poiseuille Flow

Different from incompressible flow limit, high Mach number flow demonstrates strong compressibility effect. The compressibility effect manifests via the nature of pressure. Pressure plays distinctly different roles with flow transformation from incompressible to compressible regime. To investigate the compressibility effect further pressure effect on the perturbation evolution, we focus on kinetic energy evolution of different modes in high Mach number Poiseuille flow.

4.3.2.1 Streamwise Mode ($\beta = 0°$)

At incompressible flow limit, $\beta = 0°$ corresponds to the TS instability wave. For high Mach number flow, the same wave mode is considered to investigate compressibility effect on TS instability. The kinetic energy component u^2 is examined in Figure 4.5. The u^2 component is employed to present mode growth because approximate analysis of this velocity component is performed in prediction of mode evolution at pressure released limit. Thus, pressure released limit (PRE) and TS instability limit (OSE) are given in Figure 4.5. Three Mach numbers are considered: 4.5, 6 and 7.2. The initial growth of all three cases are identical and follow the PRE limit. Thus, for high Mach number flows, the initial evolution of small perturbation modes are exempt from pressure effect. The initial growth departs from the PRE limit relatively quickly. With the higher Mach number, the departure occurs later. The subsequent evolution is influenced by oscillatory behavior. This oscillation is accompanied by decaying. After the early stage, the oscillatory kinetic energy evolution goes down and reaches a much lower limit than TS instability growth of incompressible flow. Therefore, the persistent growth of TS wave in incompressible flow is changed to oscillatory decay in high Mach number flow and the TS instability is suppressed by compressibility effect. In the oscillation region, the higher Mach number leads to

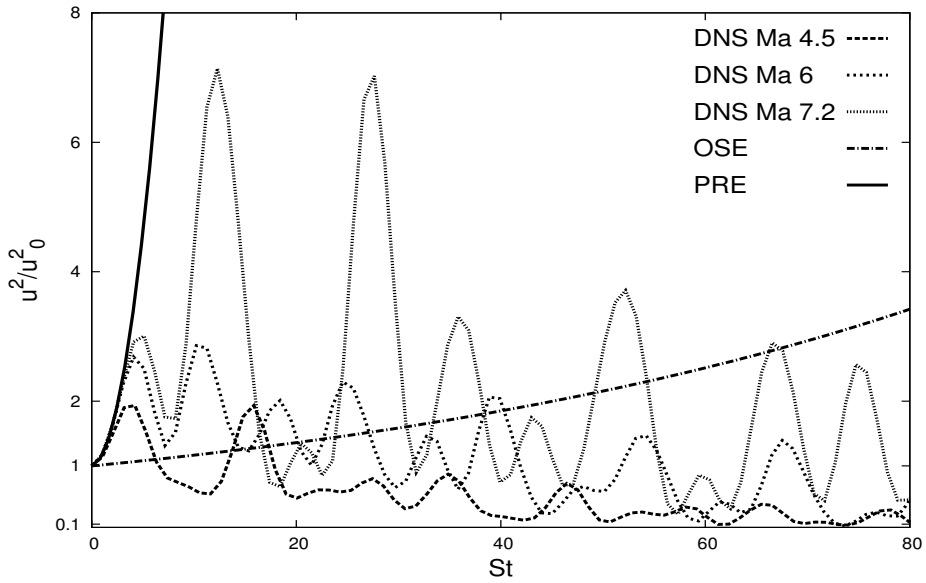

Figure 4.5: Evolution of streamwise ($\beta = 0°$) perturbation mode energy in high-speed Poiseuille flow

larger oscillatory amplitude. The Mach number essentially represents the base flow inertial effect over the acoustic effect. As mentioned, the perturbation evolution in this high Mach number Poiseuille flow demonstrates quite different behavior from low-speed case. This difference is related with the changing nature of pressure from incompressible to compressible regime. The balance behavior between flow inertial and pressure acts differently in low-speed and high-speed flows. In high-speed flow, the initial evolution of perturbation mode demonstrates sharp growing which follows the PRE limit. This scenario suggests that pressure effect is negligible at the early stage of evolution. The subsequent acoustic-like oscillation is due to the presence of pressure effect.

For $\beta = 0°$ mode, the kinetic energy component v^2 is also compared with pressure energy. Pressure energy is normalized as: $\frac{p^2}{r\bar{P}\bar{\rho}}$. For Mach 6 case, those two energy components are shown in Figure 4.6(a). The v^2 versus the total energy of the two

components with time evolution is given. This fraction initiates with the value 1 due to a null pressure perturbation. Then this value exhibits an oscillatory behavior. The fraction oscillates around the half separation represented by the dashed line. Thus, the energy is equi-partitioned between perturbation components v and p'. This result confirms the inference from linear analysis. In the linear analysis, the coupling between v and p' are shown to act as a harmonic oscillator and energy is supposed to be equi-partitioned between these two components. For Mach 4.5 case, the fraction plot is given in Figure 4.6(b). Similar equi-partition behavior is identified.

4.3.2.2 Span-wise Mode ($\beta = 90°$)

For span-wise mode, the wave vector is perpendicular to the base flow shear plane. The kinetic energy evolution of such mode at incompressible limit exhibits rapid growth. The kinetic energy plots for Mach 6 and 4.5 are given in Figures 4.7. Evidently, this mode is rapidly growing with time in high Mach number flow. The kinetic energy evolution is compared to PRE limit which excludes any pressure effect. The kinetic energy demonstrates similar behavior as PRE limit. Therefore, the span-wise mode grows without any constraint from pressure in high Mach number Poiseuille flow. In linear analysis, $\beta = 90°$ represents the zero limit of effective shear and effective Mach number. The compressibility effect on this mode is supposed to diminish to the minimal. The DNS results shown in Figure 4.7 confirm the findings from linear analysis.

4.3.2.3 Oblique Modes ($0° < \beta < 90°$)

For oblique modes with angle (β) between 0 and 90°, the individual mode evolutions are investigated by examining the kinetic energy evolution with time shown in Figure 4.8 for two Mach numbers. It is observed that the streamwise ($\beta = 0°$) mode

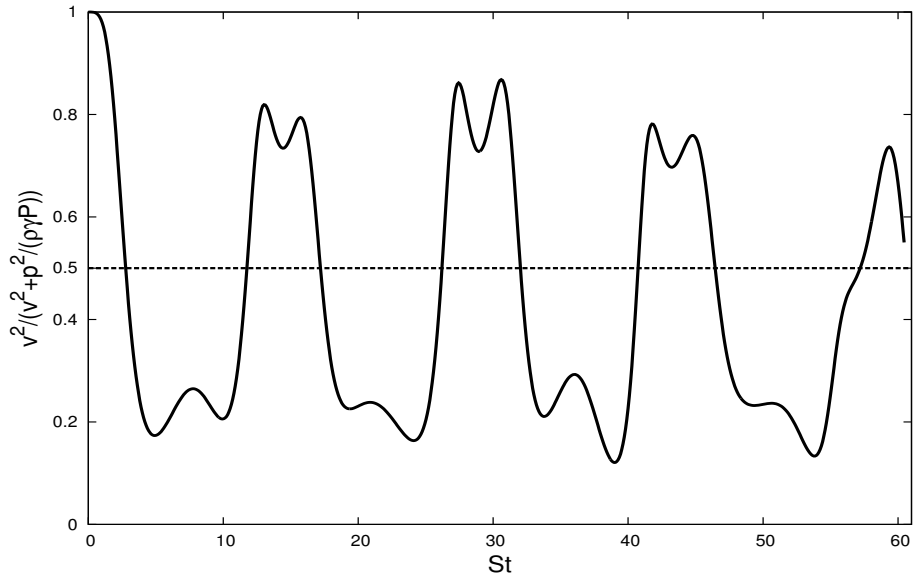

(a) Ma=6

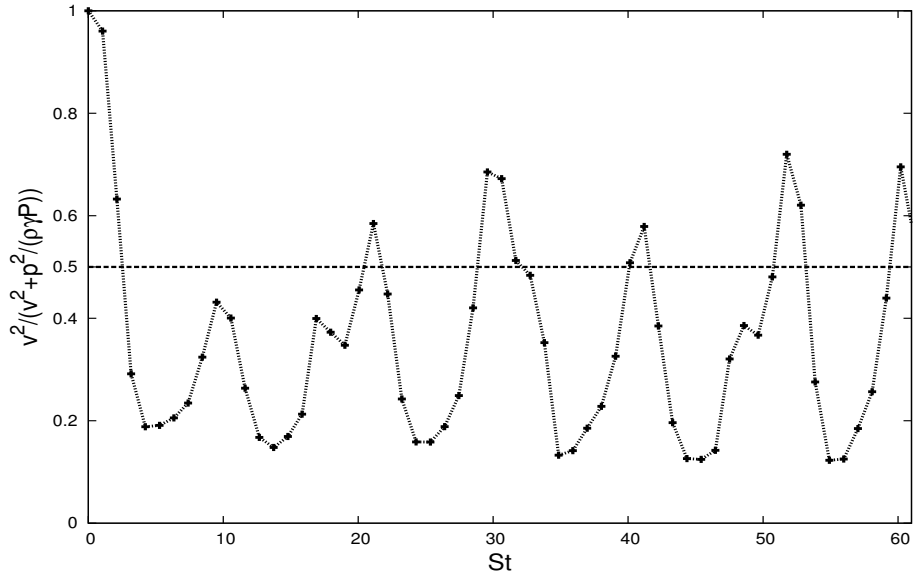

(b) Ma=4.5

Figure 4.6: Energy equi-partition between wall-normal velocity and pressure perturbation for streamwise ($\beta = 0°$) mode

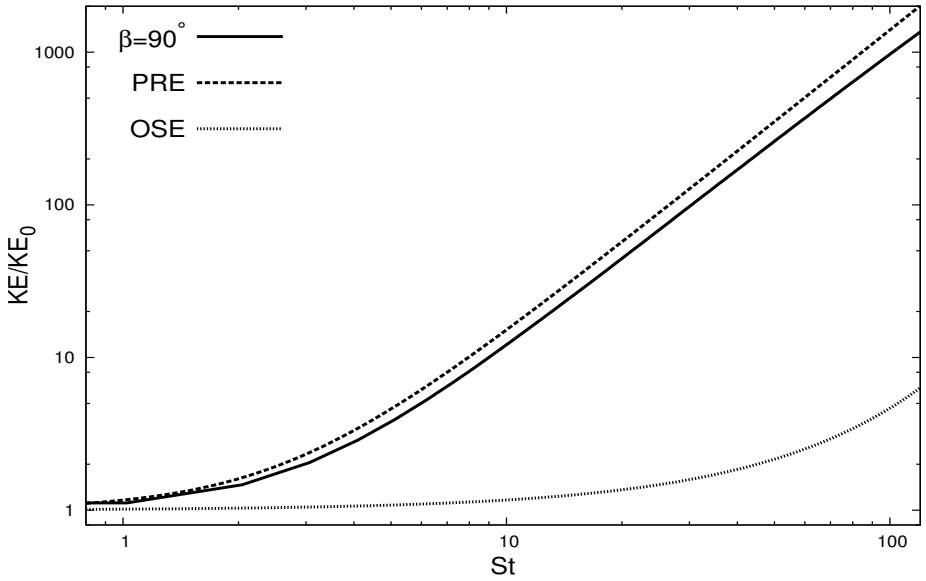

(a) Ma=6

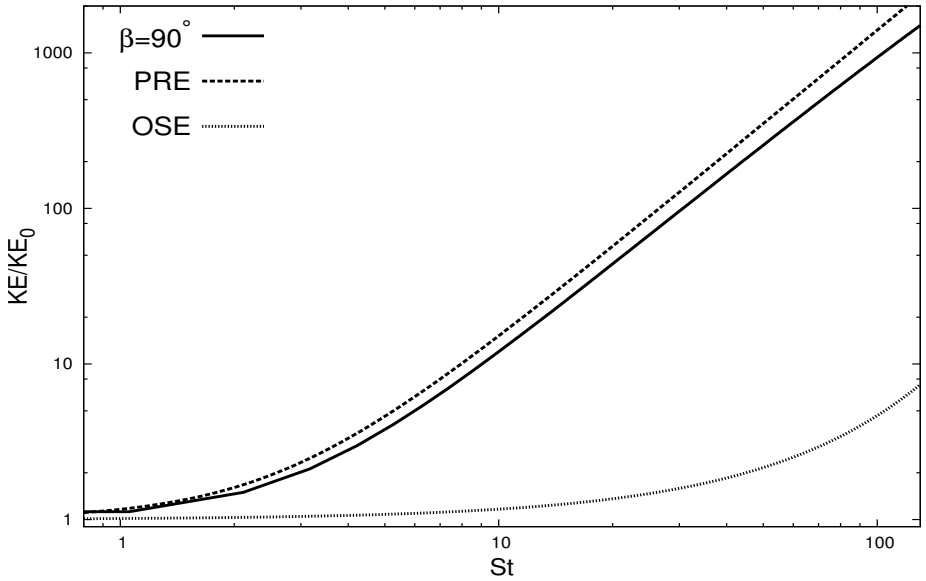

(b) Ma=4.5

Figure 4.7: Kinetic energy of span-wise ($\beta = 90°$) mode

evolution experiences the most oscillatory influence compared to other oblique modes. As mentioned before, the oscillation is brought in by the presence of acoustic-like pressure effect. Thus, the streamwise mode evolution experiences strongest influence from pressure. This finding supports the linear analysis mentioned before. The effective shear and Mach number reach maximum value with $\beta = 0°$. The strong compressibility effect is expected to appear with this mode condition from linear analysis. The oscillation impact decreases with increase in β. At $\beta = 90°$, the oscillatory behavior is not observed in the evolution. This oscillation is shown to depend on the obliqueness angle. We know that this oscillation is closely related with the behavior of pressure which acts as an acoustic wave in highly compressible flow. Therefore, the pressure effect is shown to be a function of β in current DNS results. On the other hand, the linear analysis suggests that perturbation evolution depends on the effective Mach number, further on β. Thus, the DNS results here confirm the findings from linear analysis. Based on linear analysis, a critical angle is found to characterize the transition from supersonic to subsonic effective Mach numbers. For the Mach number 6 case, the critical angle (β_c) is around 80°. In kinetic energy plot 4.8(a), 80° is the approximate separation of decaying and growing region. For the Mach number 4.5 case, the critical angle is around 77° which can be identified in Figure 4.8(b). The DNS results show that the critical angle is approximately the demarcation of mode growth and decay. Therefore, it is reasonable to propose a schematic stability map for high Mach number Poiseuille flow in mode orientation space. The stability map is given in Figure 4.9. The schematic stability map demonstrates that the $\beta = 0°$ TS instability is stabilized in high Mach number Poiseuille flow, however, with the increase in β, the stabilization effect diminishes. At around the critical angle, the stability feature is switched and modes with higher angles become unstable.

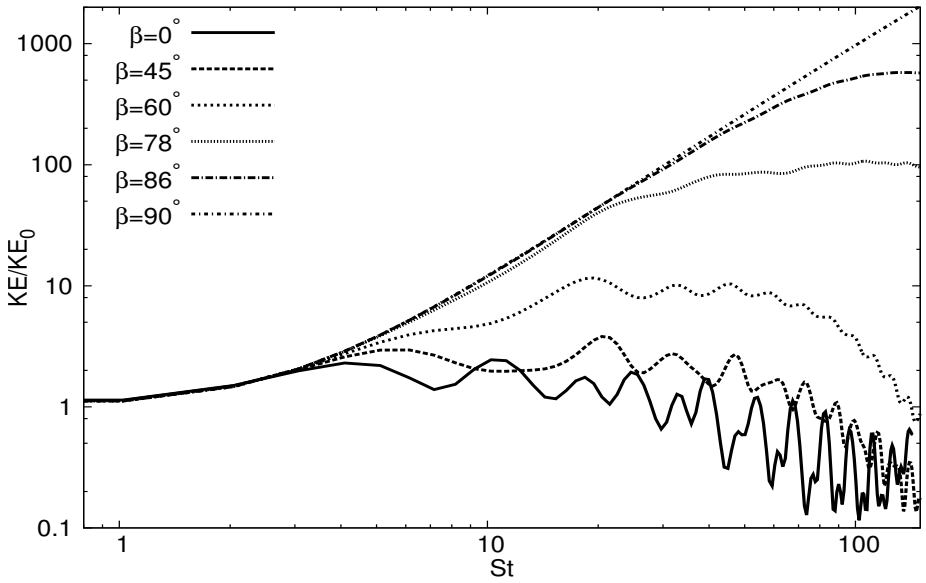

(a) Ma=6

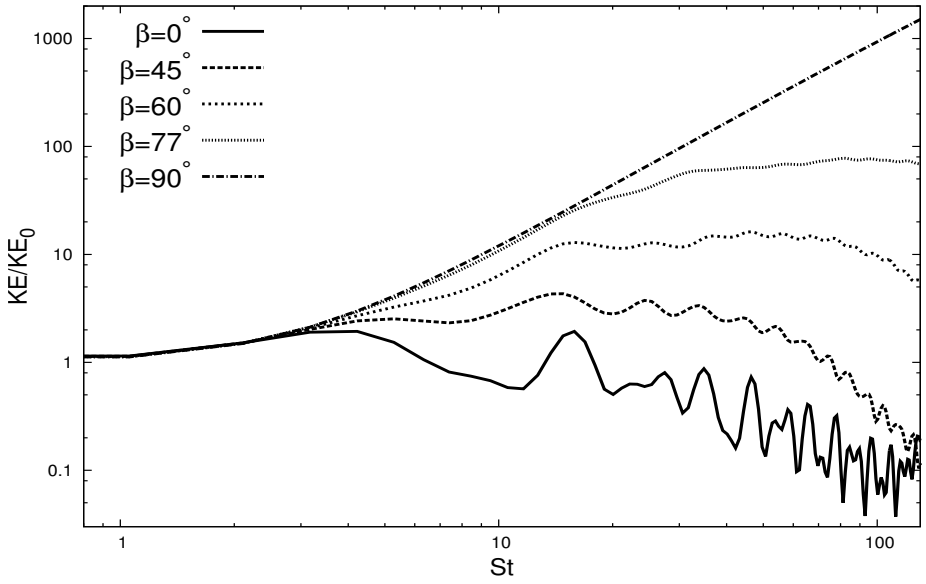

(b) Ma=4.5

Figure 4.8: Kinetic energy evolution of oblique modes

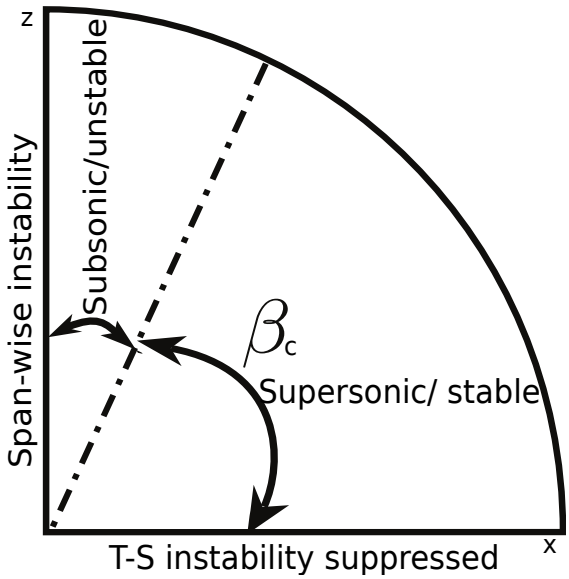

Figure 4.9: Stability map for Compressible Poiseuille flow

4.3.3 Other Initial Mode Shapes

In previous discussion, we examined the perturbation modes from Orr-Sommerfeld (OS) solutions. The OS modes demonstrate persistent instability for all β at incompressible flow limit and different stability features within two regions in high Mach number flows. To further investigate the stability characteristics of modes other than OS type, we also study two other types of mode: new mode 1 and new mode 2.

New mode 1 has the sine and cosine shapes along wall-normal direction. The perturbation is defined as:

$$u = sin(\frac{x}{L_x}2\pi) * sin(\frac{y}{L}\pi), \tag{4.51}$$

$$v = cos(\frac{x}{L_x}2\pi) * (cos(\frac{y}{L}\pi) + 1) * \frac{2L}{L_x}, \tag{4.52}$$

Here L_x is the length of dimension in streamwise direction and L is half channel width. This mode satisfies the boundary conditions at two walls and the divergence

free condition. The kinetic energy evolution of new mode 1 is shown in Figure 4.10(a). Evidently, similar behavior as OS modes is observed. New mode 2 is composed by superposition of OS mode and new mode 1. The kinetic energy evolution for this mode is given in Figure 4.10(b). The similar mode evolution as previous two are identified. Therefore, the stability characteristics shown in Figure 4.9 for OS modes are universal in high Mach number flows.

4.3.4 Vorticity Evolution of Streamwise ($\beta = 0°$) Mode

Three types of modes such as OS mode, new mode 1 and new mode 2 are examined in previous discussion. They all demonstrate similar stability feathers in high Mach number Poiseuille flow. In particular, the streamwise mode exhibits the most oscillation and stabilization influence under this highly compressible flow. To further investigate the underlying physics of compressibility impact, we examine the flow structure and span-wise vorticity evolution for streamwise mode.

4.3.4.1 Compressibility Effect

The streamwise ($\beta = 0°$) mode evolution in high-speed Poiseuille flow is quite different from that in low-speed regime. The low-speed instability is clearly suppressed and stabilized in high-speed flow. The kinetic energy evolution already shows the different behaviors. This difference can also be demonstrated in the perturbation velocity vector plot shown in Figure 4.11. For low-speed Poiseuille flow, the perturbation evolution sustains the initial spatial structure. However, the high-speed flow breaks up the initial perturbation into various small structures. More circulation exists in high-speed flow than low-speed flow. Besides the velocity vector, the span-wise vorticity also depicts the flow structure. The span-wise vorticity contours for both low and high speed Poiseuille flow are given in Figure 4.12. The vorticity is normalized by the base flow centerline velocity U_0 and length scale L. From the evolution

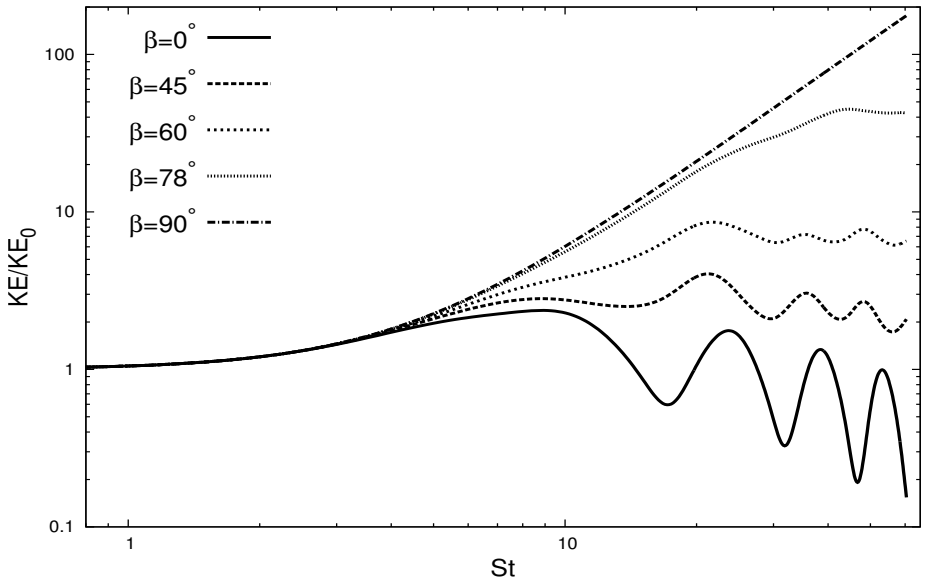

(a) New mode 1

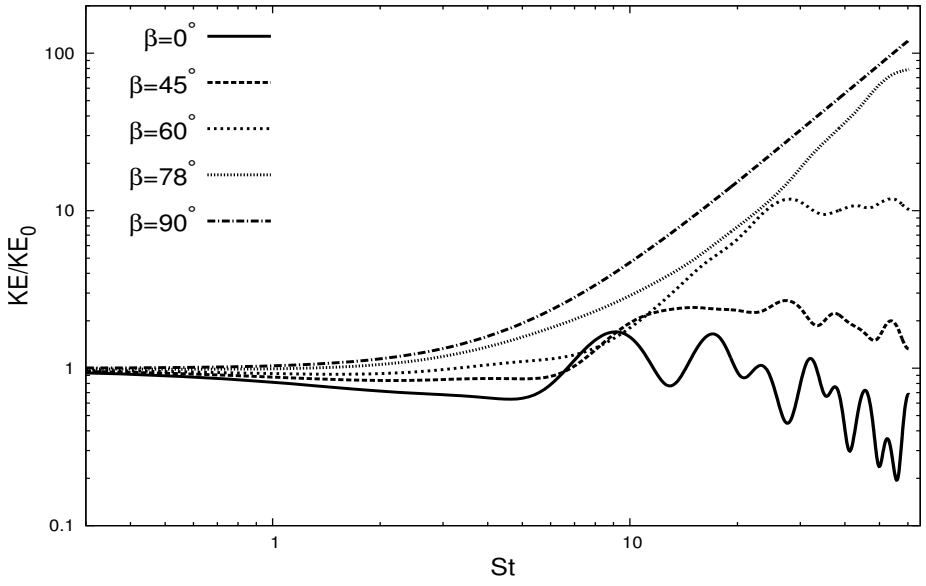

(b) New mode 2

Figure 4.10: Evolution of kinetic energy for other initial modes

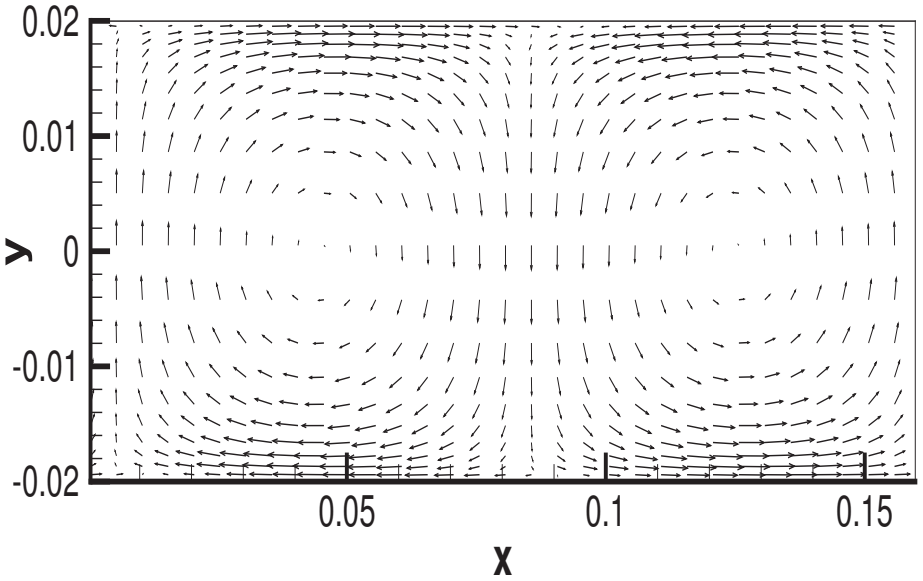

(a) Ma=0.12

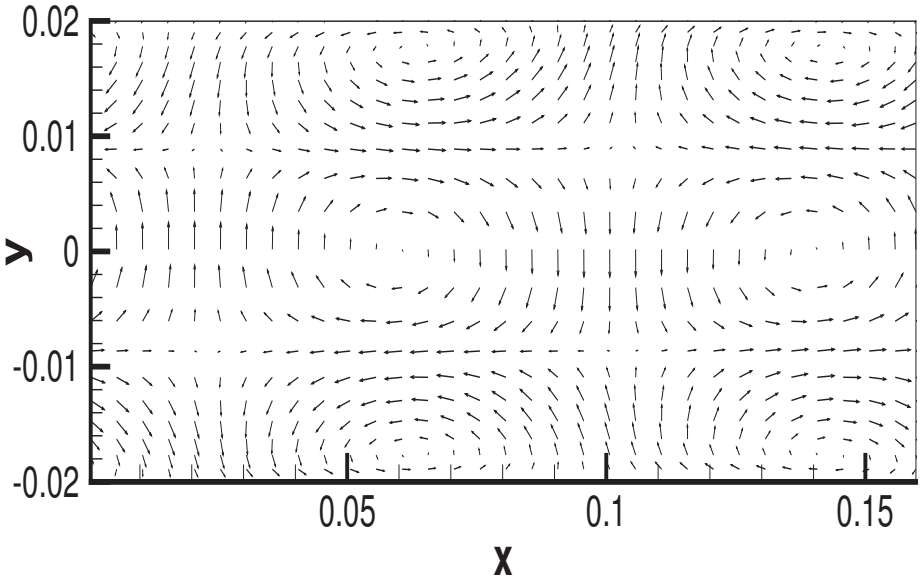

(b) Ma=6

Figure 4.11: Flow structure of both low-speed and high-speed flow

of vorticity contour, we found that vorticity for the low-speed case has stationary structure with time evolution however for the high-speed case the vorticity structure is changing rapidly. The distinctly different behavior in span-wise vorticity evolution of high-speed flow is an additional representation of compressibility influence on perturbation evolution.

4.3.4.2 Inhomogeneity Effect

The span-wise vorticity structure is examined in the previous discussion. To analyze the vorticity evolution further, we focus on the linearized span-wise vorticity equation given in equation (4.50). There are three major terms on the right side of equation besides the viscous effect which is trivial in present analysis. As mentioned before, the baroclinic term and compressible vorticity production are related to the compressibility effect, whereas the second derivative term exists in both the incompressible and compressible flow regimes. In high Mach number Poiseuille flow, those three balancing mechanisms are examined numerically. Those three budget terms are shown in Figure 4.13. From the budget shown, the baroclinic term is trivial compared to other two. The compressible vortex production term is shown to be dominant in the plot. In the DNS result, this compressible vorticity production is one order higher than second derivative term. Therefore, the compressible vorticity production term is more critical in the vorticity evolution for high Mach number flow. As mentioned before, the second derivative term represents the inhomogeneous shear effect since it reduces to zero for homogeneous shear flow. Thus, the inhomogeneity effect is superseded by compressibility impact in this high Mach number Poiseuille flow.

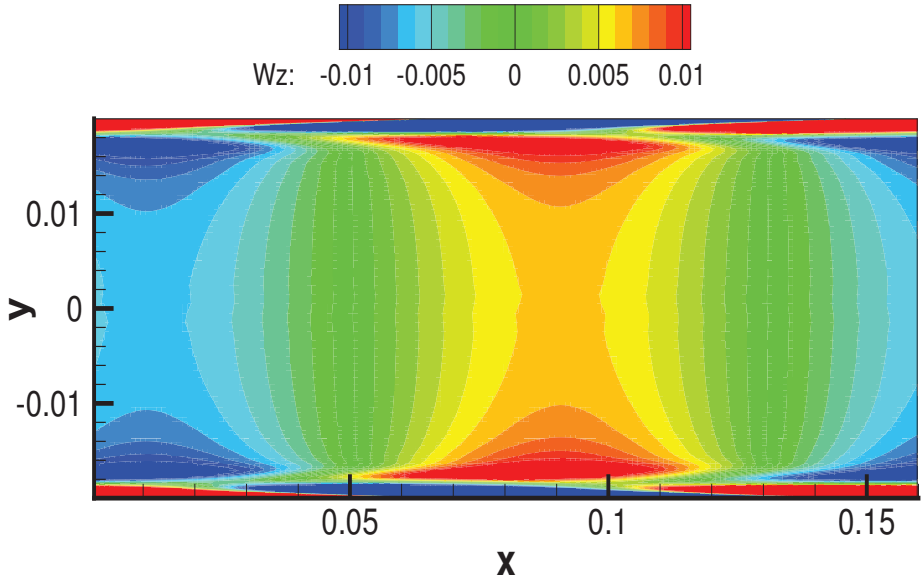

(a) Ma=0.12

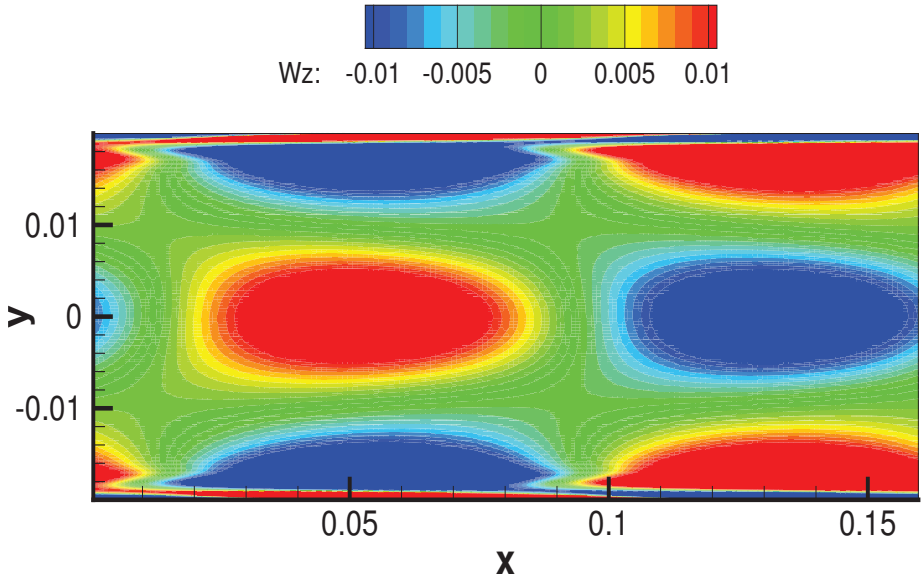

(b) Ma=6

Figure 4.12: Span-wise vorticity contour of both low-speed and high-speed flow: normalized by $U_0 = 931.6m/s$,$L = 0.020032m/s$

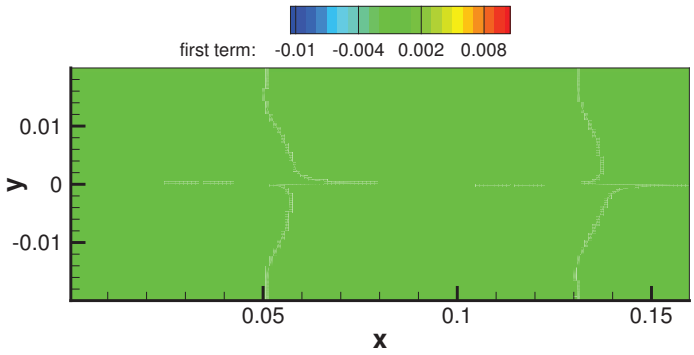

(a) Baroclinic term

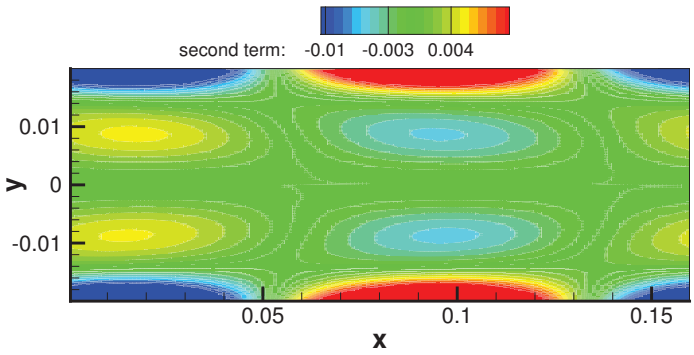

(b) Compressible vortex production

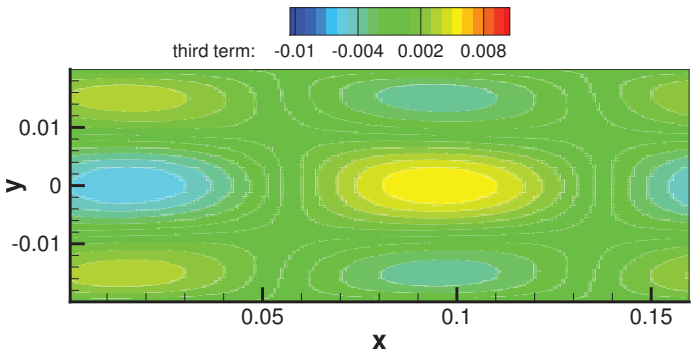

(c) Second derivative term

Figure 4.13: Span-wise vorticity budget term at Mach 6: normalized by $\frac{U_0^2}{L^2}$

4.4 Coupled Modes to Late Stage Evolution

The single mode evolution is discussed in the previous section. The stability of single mode is well characterized by linear analysis. To further investigate the perturbation evolution into late stage, 3-D perturbation modes are considered. In this work, we consider two coupled oblique modes as initial conditions. The nonlinear interactions between two oblique modes are examined and presented.

4.4.1 Single Mode and Coupled Modes

The comparison between two oblique modes and single mode with same obliqueness angle $\beta = 60°$ is shown in Figure 4.14(a). As the single mode evolution, coupled modes initially show rapid growth for short time. After departure from initial growth, coupled modes fall to a stabilization region. At late time, persistent growth of coupled modes is observed while single mode decays to trivial. The comparison between two coupled modes and individual mode with same obliqueness angle $\beta = 78°$ is shown in Figure 4.14(b). Thus, in both cases the coupled modes evolution demonstrates quite different behavior. The coupled mode evolution can be illustrated by the stability map shown in Figure 4.15. The initial two modes are interacting to generate other modes. The derivative modes have a portion fall into unstable region and other portion fall into stable region. The unstable modes will retain leading to the later stage growth identified in Figure 4.14.

4.4.2 Late Stage Modes Evolution

The two coupled oblique modes evolution yields late stage growth and possible breakdown to turbulence. The kinetic energy evolution of two 60° oblique modes is given in Figure 4.16. Five time instances are pointed out in the kinetic energy plot. Corresponding to the kinetic energy evolution at these five time spots, the contours of

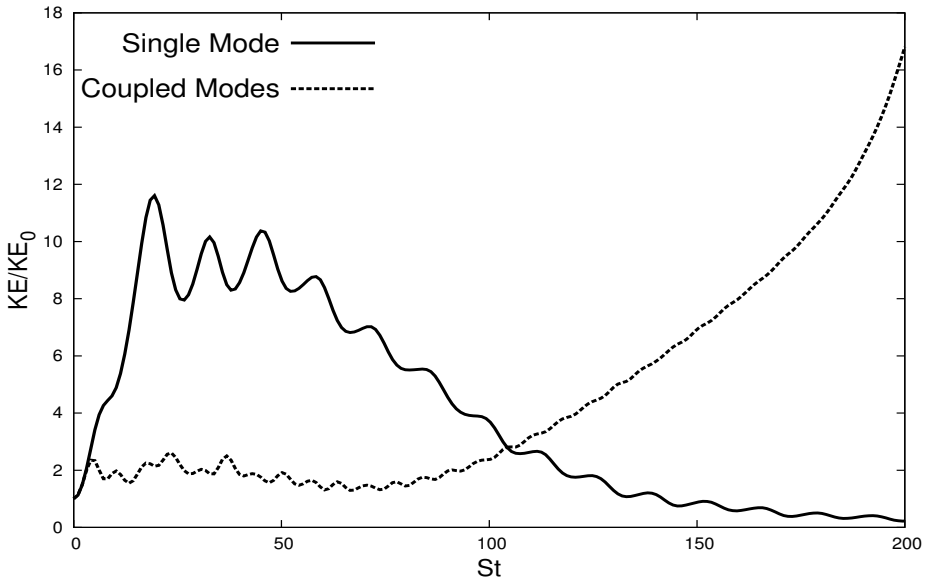

(a) $\beta = 60°$

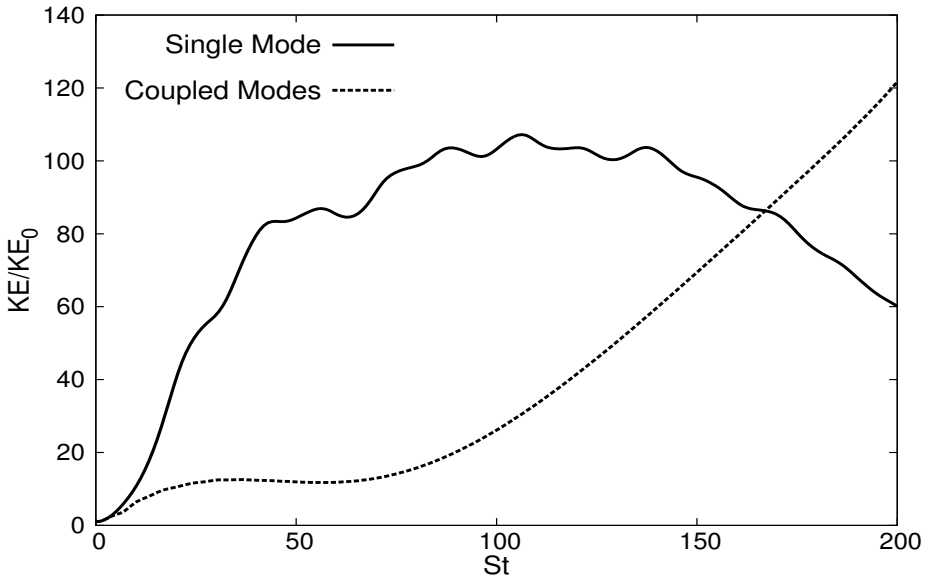

(b) $\beta = 78°$

Figure 4.14: Evolution of kinetic energy for single mode and coupled modes at Mach 6

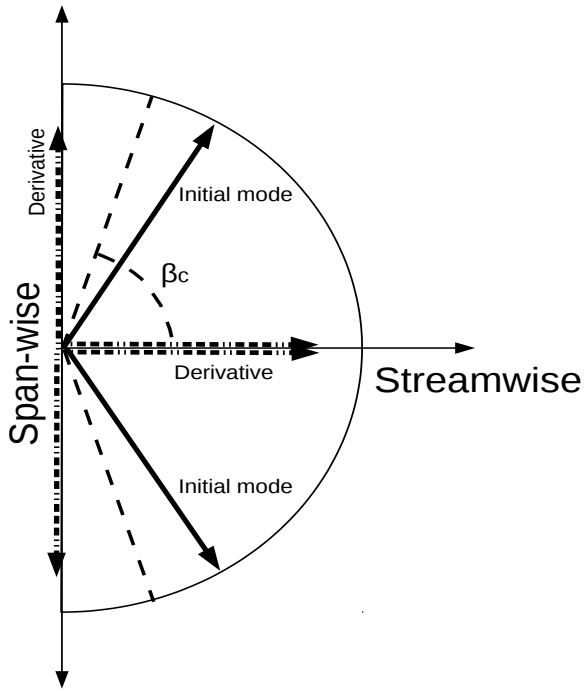

Figure 4.15: Stability map for two oblique modes in compressible Poiseuille flow

streamwise velocity perturbation are shown in Figures 4.17(a),4.18(a),4.19(a),4.20(a) and 4.21(a). The contour clearly shows the mode orientation change in coupled modes evolution. At $St = 120$, most energetic modes are span-wise modes. From the oblique mode discussion as before, these span-wise modes have continuous growth exempt from any pressure constraint. With dominant span-wise modes, the perturbation exhibits late-stage growth and then breaks down. At $St = 200$, flow starts to break down and then finally breaks down at $St = 250$. The wavenumber spectrum is also examined at the same plane as the contour. The spectrum is shown in Figures 4.17(b),4.18(b),4.19(b),4.20(b) and 4.21(b). At the early stage $St = 2$, there exist both streamwise and span-wise wave numbers. As flow evolves to $St = 120$, only span-wise dominant waves are observed. As flow breaks down, much broader spectrum is identified at $St = 250$.

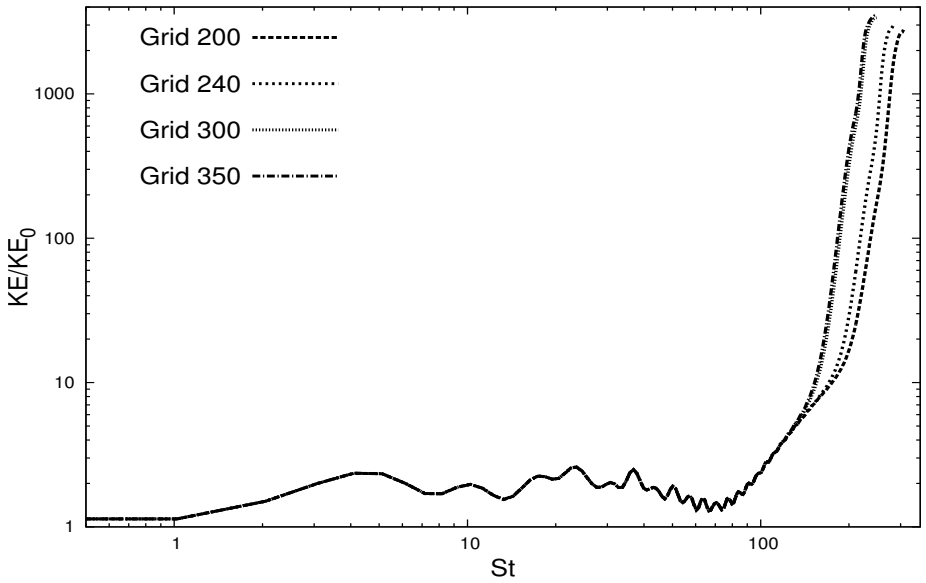

(a) Grid convergence

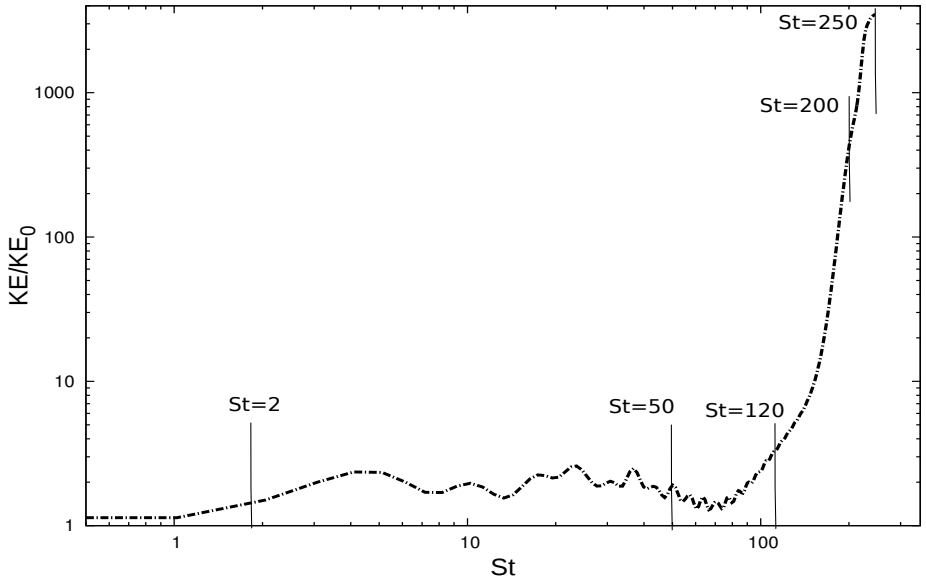

(b) Kinetic energy evolution

Figure 4.16: Kinetic energy evolution of coupled 60° modes at Mach 6

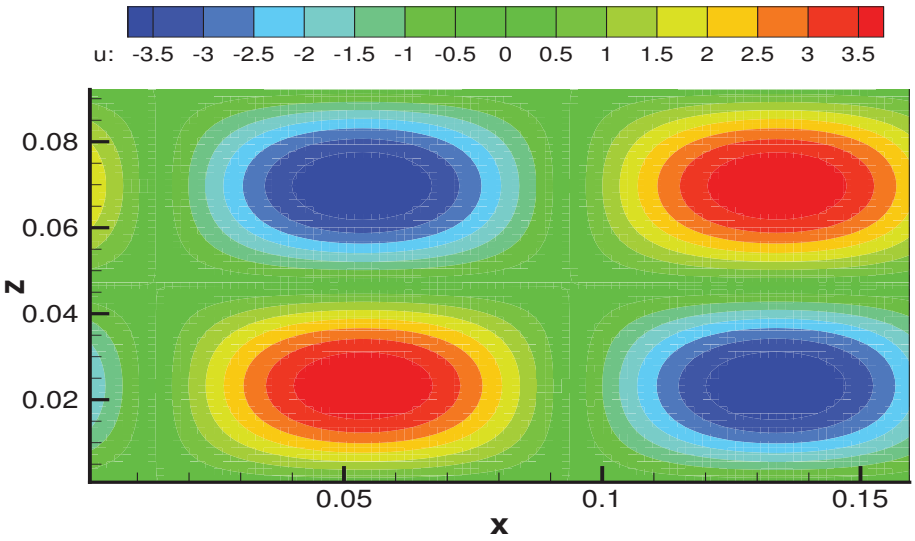

(a) Streamwise velocity perturbation contour

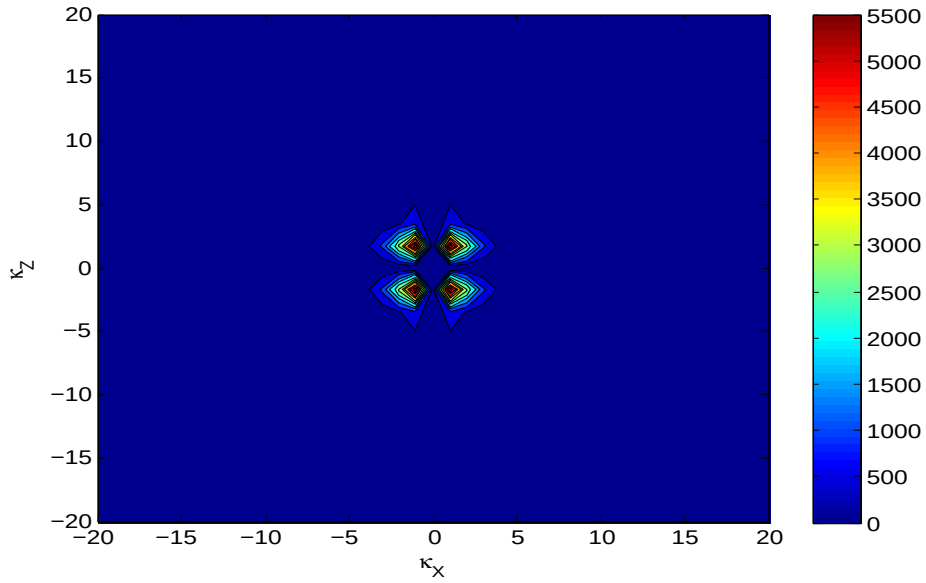

(b) Wavenumber spectrum

Figure 4.17: Streamwise perturbation velocity contour and wavenumber spectrum of coupled 60° modes at Mach 6:St=2

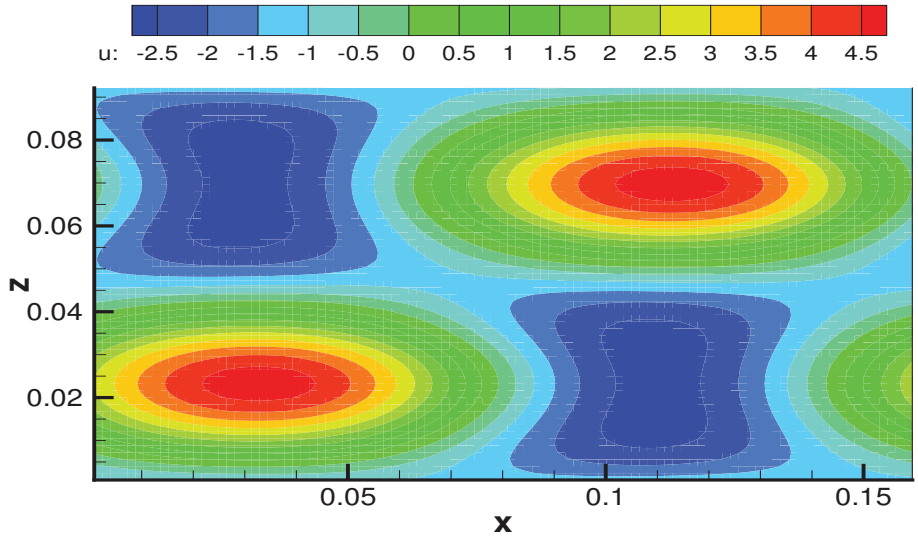

(a) Streamwise velocity perturbation contour

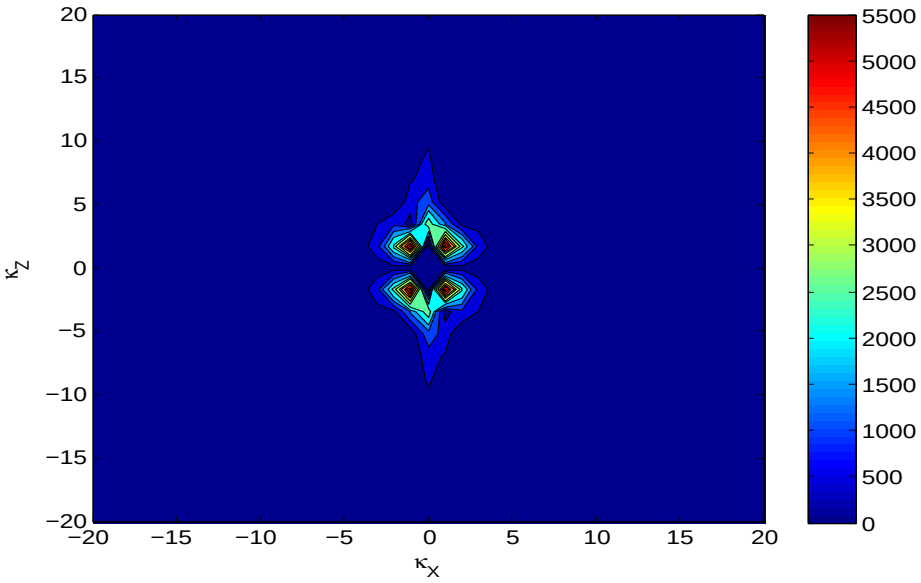

(b) Wavenumber spectrum

Figure 4.18: Streamwise perturbation velocity contour and wavenumber spectrum of coupled 60° modes at Mach 6:St=50

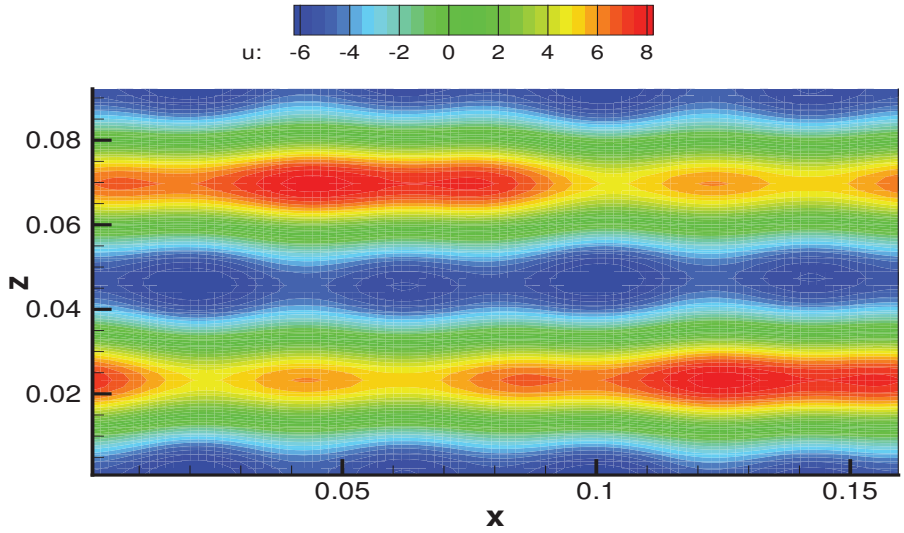

(a) Streamwise velocity perturbation contour

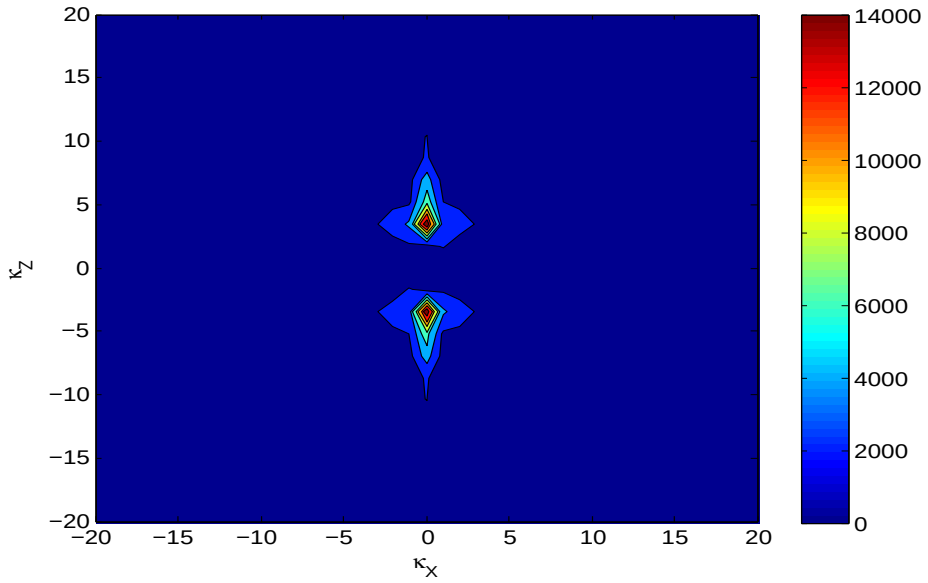

(b) Wavenumber spectrum

Figure 4.19: Streamwise perturbation velocity contour and wavenumber spectrum of coupled 60° modes at Mach 6:St=120

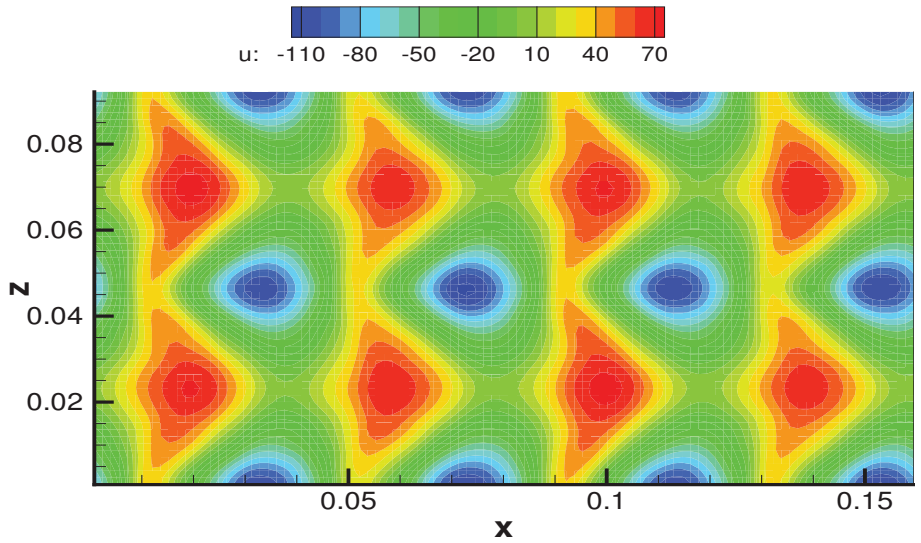

(a) Streamwise velocity perturbation contour

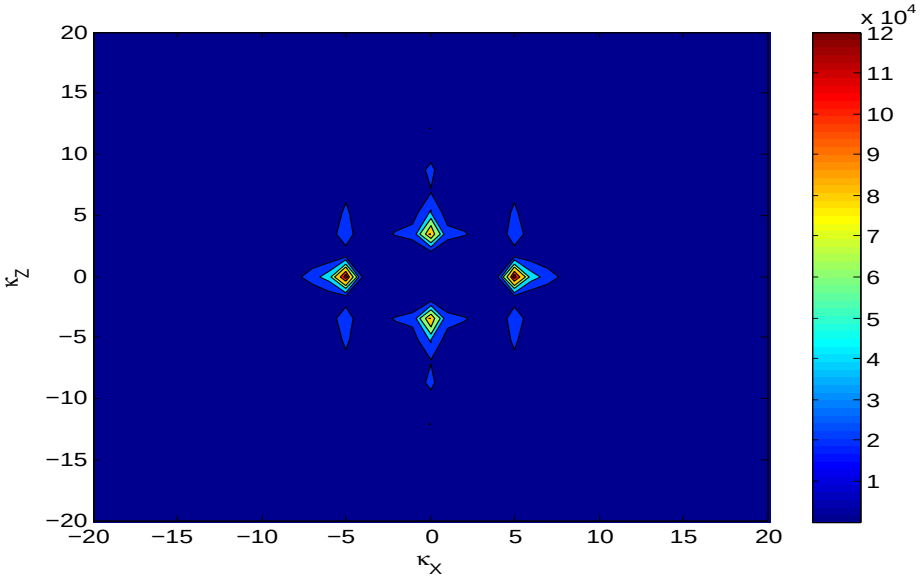

(b) Wavenumber spectrum

Figure 4.20: Streamwise perturbation velocity contour and wavenumber spectrum of coupled 60° modes at Mach 6:St=200

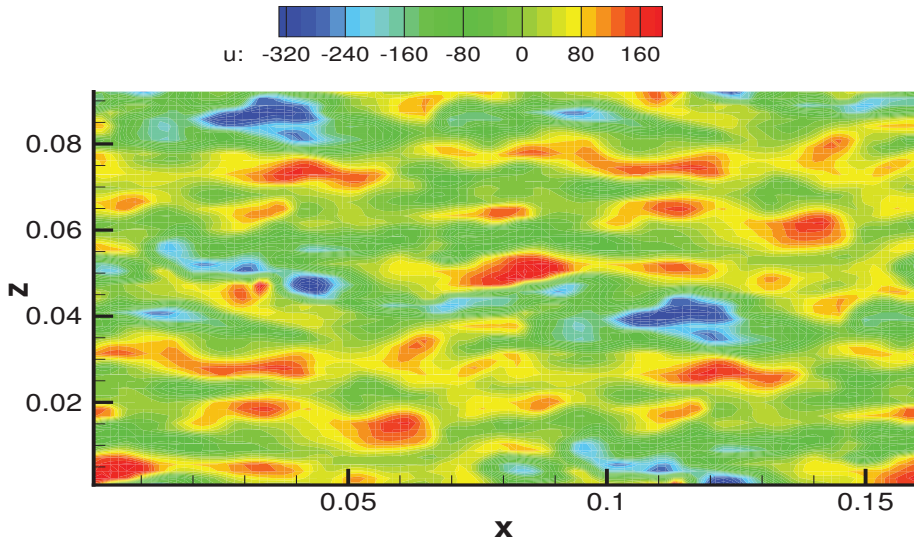

(a) Streamwise velocity perturbation contour

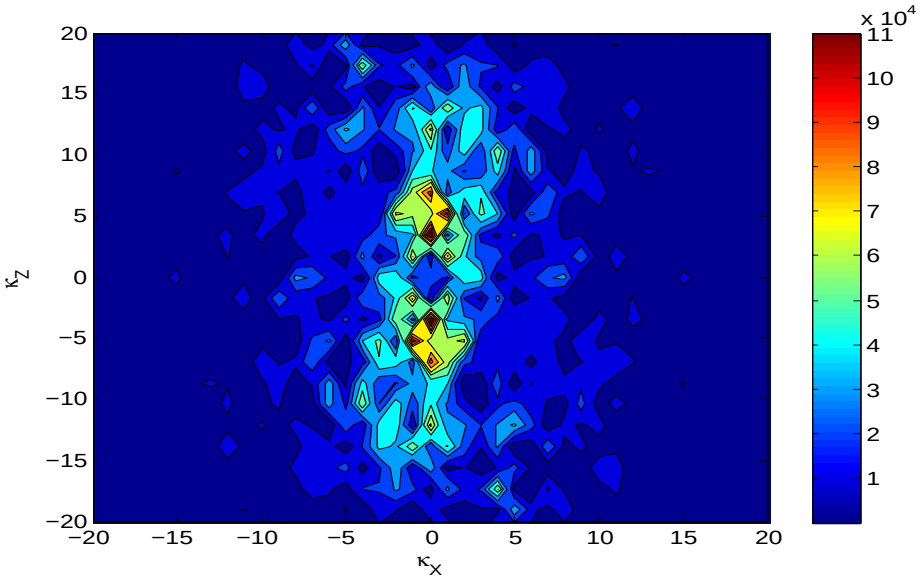

(b) Wavenumber spectrum

Figure 4.21: Streamwise perturbation velocity contour and wavenumber spectrum of coupled 60° modes at Mach 6:St=250

4.5 Summary and Conclusion

Compressibility effects in high-speed flow cause distinctly different flow pattern compared to incompressible low-speed flow. This difference is related to the changing behavior of pressure with the flow transformation from low-speed to high-speed regime. At very low Mach number pressure is dictated by the Poisson equation. Pressure evolves fast enough to instantly impose divergence free condition to the velocity field. However, at very high Mach number the action of pressure is relatively slow compared to that of velocity field. Consequently, the velocity field evolves almost unaffected by pressure. At intermediate Mach numbers, the time scale of pressure evolution is comparable to that of velocity. Pressure behaves according to wave equation resulting from the energy equation and thermodynamic state equation. In this study, we focused on the instability characteristics of Poiseuille flow at intermediate Mach numbers by investigating the evolution of small perturbation in forms of various wave modes.

We perform linear analysis and DNS studies of small perturbation evolution. The linearized perturbation analysis suggests that the perturbation mode obliqueness and Mach number are two critical parameters that affect stability in compressible flows. The DNS results confirm that the mode evolution is dependent on obliqueness and Mach numbers in high Mach number Poiseuille flow. The DNS work is first performed for single perturbation mode. The kinetic energy evolution for single mode is used to demonstrate the demarcated stability regions in perturbation orientation space. The zero angle mode is shown to experience the most suppression and stabilization from compressibility effect. On the other hand, the span-wise mode experiences very little compressibility effects. There exists a critical obliqueness angle between them to demarcate the stability region. With increase in Mach number, the evolution of

perturbation kinetic energy is affected by the growing inertial effect. By simulating two coupled oblique modes we find that the kinetic energy evolution exhibits multiple stage behavior which is quite different from single mode evolution. Non-linear interactions between modes are shown to play a critical role. The non-linear breakdown toward turbulence is also demonstrated.

5. CONCLUSIONS

In this doctoral thesis, we investigate the stability characteristics of high-speed laminar Poiseuille flow by performing linear analysis and temporal DNS. The work consists of three parts. The major findings of each study is summarized in the corresponding section. Here we present a brief synopsis of each study.

5.1 Development of GKM Solver

The first study addresses the development and validation of the GKM scheme for wall-bounded high Mach number flows. In low-speed flows, GKM simulation results are compared against Orr-Sommerfeld analytical solution resulting in excellent agreement. In high-speed flows, grid and time-step convergence study are performed for code verification. The budget of Reynolds stress evolution equation is examined. The two sides of the budget equation are shown to have exact equivalence verifying the fidelity of simulations. To better accommodate the spatial variations in Poiseuille flow, the fifth order non-uniform WENO scheme is developed and implemented into the GKM solver. The simulation results for both uniform and non-uniform WENO schemes are compared by examining the kinetic energy evolution. Non-uniform WENO is shown to yield superior performance. Both body force and pressure-gradient are examined for sustaining the flow. For low-speed flows, small perturbation evolution agrees well with linear theory for both cases and the type of driving does not significantly alter the thermodynamic quantity evolution due to weak thermodynamic coupling. For high-speed flows, body force driving produces a background thermodynamic field that is uniform in the stream-wise direction. Pressure-gradient driven simulation results show undesirable stream-wise gradients leading to unphysical results. Therefore, it is concluded that body force

driven temporal simulations is better suited for temporal simulations of compressible flows.

5.2 Stability at Extreme Mach Numbers

We establish the stability characteristics at very high and very low Mach number limits before proceeding to intermediate Mach numbers in the third study. We develop linear pressure-released equation (PRE) analysis to describe the stability of very high Mach number Poiseuille flow. The PRE and Orr-Sommerfeld analysis are compared against Poiseuille flow DNS results at extreme Mach numbers. The DNS employs the Gas-Kinetic Method (GKM) to study small perturbation evolution in channel flows over a range of Mach and Reynolds numbers. The agreement between numerical simulations and linear analysis is excellent. Overall this study confirms the physical accuracy and numerical viability of GKM approach for simulating wall-bounded flow instabilities over a large Mach number range. Further, the importance of PRE for describing wall-bounded non-uniform shear flow at early stage of evolution is firmly established.

5.3 Stability at Intermediate Mach Numbers

In this study, we perform linear analysis and DNS studies of small perturbation evolution at intermediate Mach numbers. The linearized perturbation analysis suggests that the perturbation mode obliqueness and Mach number are two critical parameters that affect stability in compressible flows. The DNS results confirm that the mode evolution are dependent on obliqueness and Mach numbers in a self-similar manner as suggested by linear analysis. The DNS investigation is first performed for single perturbation mode. The kinetic energy evolution for single mode is used to demarcate stability regions in perturbation orientation space. It is shown that the zero angle mode (Tollmien-Schlichting instability) experiences the most suppression

and stabilization due to compressibility effects. On the other hand, span-wise modes experience very little compressibility effects. There exists a critical obliqueness angle which demarcates the sub and supersonic modes. With the increase in Mach number, the evolution of perturbation kinetic energy is affected to different degrees in the different obliqueness regions. By coupling two oblique modes we find that the kinetic energy evolution exhibits multiple stage behavior which is quite different from single mode evolution. Non-linear interactions between modes are shown to play a critical role. The non-linear breakdown toward turbulence is also examined.

REFERENCES

[1] S. G. Goebel and J. C. Dutton, "Experimental study of compressible turbulent mixing layers," *AIAA Journal*, vol. 29, no. 4, pp. 538–546, 1991.

[2] T. L. Jackson and C. E. Grosch, "Absolute/convective instabilities and the convective Mach number in a compressible mixing layer," *Physics of Fluids A: Fluid Dynamics (1989-1993)*, vol. 2, no. 6, pp. 949–954, 1990.

[3] S. Sarkar, "The stabilizing effect of compressibility in turbulent shear flow," *Journal of Fluid Mechanics*, vol. 282, pp. 163–186, 1995.

[4] A. Simone, G. N. Coleman, and C. Cambon, "The effect of compressibility on turbulent shear flow: a rapid-distortion-theory and direct-numerical-simulation study," *Journal of Fluid Mechanics*, vol. 330, pp. 307–338, 1997.

[5] K. Lee, S. S. Girimaji, and J. Kerimo, "Effect of compressibility on turbulent velocity gradients and small-scale structure," *Journal of Turbulence*, vol. 10, no. 9, pp. 1–18, 2009.

[6] D. J. Mee, "Boundary layer transition measurements in hypervelocity flows in a shock tunnel," in *39th AIAA Aerospace Sciences Meeting and Exhibit*, no. 2001-0208, pp. 1–11, American Institute of Aeronautics and Astronautics, 2001.

[7] J. L. Papp, D. C. Kenzakowski, and S. M. Dash, "Extensions of a rapid engineering approach to modeling hypersonic laminar to turbulent transitional flows," *AIAA Paper*, vol. 892, pp. 1–17, 2005.

[8] C. J. Roy and F. G. Blottner, "Review and assessment of turbulence models for hypersonic flows," *Progress in Aerospace Sciences*, vol. 42, pp. 469–530, 2006.

[9] A. C. Laible and H. F. Fasel, "Numerical investigation of hypersonic transition for a flared and a straight cone at Mach 6," *AIAA Paper*, vol. 3565, pp. 1–23, 2011.

[10] J. Sivasubramanian and H. F. Fasel, "Direct numerical simulation of a turbulent spot in a cone boundary-layer at Mach 6," *AIAA Paper*, vol. 4599, pp. 1–26, 2010.

[11] H. Yu, L. Luo, and S. S. Girimaji, "Scalar mixing and chemical reaction simulations using lattice Boltzmann method," *International Journal of Computational Engineering Science*, vol. 3, no. 1, pp. 73–88, 2002.

[12] H. Yu, S. S. Girimaji, and L. Luo, "DNS and LES of decaying isotropic turbulence with and without frame rotation using lattice Boltzmann method," *Journal of Computational Physics*, vol. 209, no. 2, pp. 599–616, 2005.

[13] H. Yu, S. S. Girimaji, and L. S. Luo, "Lattice Boltzmann simulations of decaying homogeneous isotropic turbulence," *Physical Review E*, vol. 71, no. 1, p. 016708, 2005.

[14] D. Yu and S. S. Girimaji, "Multi-block lattice Boltzmann method: Extension to 3D and validation in turbulence," *Physica A: Statistical Mechanics and Its Applications*, vol. 362, no. 1, pp. 118–124, 2006.

[15] H. Yu and S. S. Girimaji, "Near-field turbulent simulations of rectangular jets using lattice Boltzmann method," *Physics of Fluids*, vol. 17, no. 12, p. 125106, 2005.

[16] J. Kerimo and S. S. Girimaji, "Boltzmann-BGK approach to simulating weakly compressible 3D turbulence: comparison between lattice Boltzmann and gas kinetic methods," *Journal of Turbulence*, vol. 8, no. 46, pp. 1–16, 2007.

[17] G. Kumar, S. S. Girimaji, and J. Kerimo, "WENO-enhanced gas-kinetic scheme for direct simulations of compressible transition and turbulence," *Journal of Computational Physics*, vol. 234, pp. 499–523, 2013.

[18] R. Bertsch, S. Suman, and S. S. Girimaji, "Rapid distortion analysis of high Mach number homogeneous shear flows: Characterization of flow-thermodynamics interaction regimes," *Physics of Fluids*, vol. 24, no. 12, p. 125106, 2012.

[19] M. Nishioka, S. Iida, and Y. Ichikawa, "An experimental investigation of the stability of plane Poiseuille flow," *Journal of Fluid Mechanics*, vol. 72, pp. 731–751, 1975.

[20] C. Liang, S. Premasuthan, and A. Jameson, "Large eddy simulation of compressible turbulent channel flow with spectral difference method," *AIAA Paper*, vol. 402, pp. 1–15, 2009.

[21] G. N. Coleman, J. Kim, and R. D. Moser, "A numerical study of turbulent supersonic isothermal-wall channel flow," *Journal of Fluid Mechanics*, vol. 305, pp. 159–183, 1995.

[22] H. Foysi, S. Sarkar, and R. Friedrich, "Compressibility effects and turbulence scalings in supersonic channel flow," *Journal of Fluid Mechanics*, vol. 509, pp. 207–216, 2004.

[23] G. Kumar, *Compressible Shear Flow Transition and Turbulence: Enhancement of GKM Scheme and Simulation/Analysis of Pressure Effects on Flow Stabilization*. PhD dissertation, Texas A&M University, 2012.

[24] K. Xu, L. Martinelli, and A. Jameson, "Gas-kinetic finite volume methods, flux-vector splitting, and artificial diffusion," *Journal of Computational Physics*, vol. 120, no. 1, pp. 48–65, 1995.

[25] Q. Li, S. Fu, and K. Xu, "Application of gas-kinetic scheme with kinetic boundary conditions in hypersonic flow," *AIAA Journal*, vol. 43, no. 10, pp. 2170–2176, 2005.

[26] Q. Li, K. Xu, and S. Fu, "A high-order gas-kinetic Navier-Stokes flow solver," *Journal of Computational Physics*, vol. 229, no. 19, pp. 6715–6731, 2010.

[27] D. Chae, C. Kim, and O. H. Rho, "Development of an improved gas-kinetic BGK scheme for inviscid and viscous flows," *Journal of Computational Physics*, vol. 158, no. 1, pp. 1–27, 2000.

[28] W. Liao, Y. Peng, and L. S. Luo, "Gas-kinetic schemes for direct numerical simulations of compressible homogeneous turbulence," *Physical Review E*, vol. 80, no. 4, p. 046702, 2009.

[29] S. Chen, K. Xu, C. Li, and Q. Cai, "A unified gas kinetic scheme with moving mesh and velocity space adaptation," *Journal of Computational Physics*, vol. 231, no. 20, pp. 6643–6664, 2012.

[30] G. May, B. Srinivasan, and A. Jameson, "An improved gas-kinetic BGK finite-volume method for three-dimensional transonic flow," *Journal of Computational Physics*, vol. 220, no. 2, pp. 856–878, 2007.

[31] R. Wang, H. Fei, and R. J. Spiteri, "Observations on the fifth-order WENO method with non-uniform meshes," *Applied Mathematics and Computation*, vol. 196, no. 1, pp. 433–447, 2008.

[32] P. G. Huang, G. N. Coleman, and P. Bradshaw, "Compressible turbulent channel flows: DNS results and modeling," *Journal of Fluid Mechanics*, vol. 305, pp. 185–218, 1995.

[33] Y. Morinishi, S. Tamano, and K. Nakabayashi, "A DNS algorithm using b-spline collocation method for compressible turbulent channel flow," *Computers & Fluids*, vol. 32, no. 5, pp. 751–776, 2003.

[34] S. B. Pope, *Turbulent Flows*. Cambridge: Cambridge University Press, 2000.

[35] D. C. Wilcox, *Turbulence Modeling for CFD*. DCW Industries La Canada, CA, 1998.

[36] A. A. Mishra and S. S. Girimaji, "Intercomponent energy transfer in incompressible homogeneous turbulence: multi-point physics and amenability to one-point closures," *Journal of Fluid Mechanics*, vol. 731, pp. 639–681, 2013.

[37] C. Cambon, G. N. Coleman, and N. N. Mansour, "Rapid distortion analysis and direct simulation of compressible homogeneous turbulence at finite Mach number," *Journal of Fluid Mechanics*, vol. 257, pp. 641–665, 1993.

[38] R. K. Bikkani and S. S. Girimaji, "Role of pressure in nonlinear velocity gradient dynamics in turbulence," *Physical Review E*, vol. 75, no. 3, p. 036307, 2007.

[39] L. Mack, *Boundary-Layer Linear Stability Theory*. Belvoir: Defense Technical Information Center, 1984.

[40] P. J. Schmid and D. S. Henningson, *Stability and Transition in Shear Flows.* New York: Springer, 2001.

[41] W. H. Heiser and D. T. Pratt, *Hypersonic Airbreathing Propulsion.* Washington,DC: AIAA, 1994.

[42] A. Harten, B. Engquist, S. Osher, and S. R. Chakravarthy, "Uniformly high order accurate essentially non-oscillatory schemes,III," *Journal of Computational Physics*, vol. 71, no. 2, pp. 231–303, 1987.

[43] G. S. Jiang and C. W. Shu, "Efficient implementation of weighted ENO schemes," *Journal of Computational Physics*, vol. 126, no. 1, pp. 202–228, 1996.

[44] K. Xu and K. H. Prendergast, "Numerical Navier-Stokes solutions from gas kinetic theory," *Journal of Computational Physics*, vol. 114, no. 1, pp. 9–17, 1994.

[45] K. Xu, "A Gas-Kinetic BGK scheme for the Navier-Stokes equations and its connection with artificial dissipation and Godunov method," *Journal of Computational Physics*, vol. 171, no. 1, pp. 289–335, 2001.

[46] K. Xu, M. Mao, and L. Tang, "A multidimensional gas-kinetic BGK scheme for hypersonic viscous flow," *Journal of Computational Physics*, vol. 203, no. 2, pp. 405–421, 2005.

[47] K. Xu and E. Josyula, "Gas-kinetic scheme for rarefied flow simulation," *Mathematics and Computers in Simulation*, vol. 72, no. 2, pp. 253–256, 2006.

[48] K. Xu and J. C. Huang, "A unified gas-kinetic scheme for continuum and rarefied flows," *Journal of Computational Physics*, vol. 229, no. 20, pp. 7747–7764, 2010.

[49] T. Maeder, N. A. Adams, and L. Kleiser, "Direct simulation of turbulent supersonic boundary layers by an extended temporal approach," *Journal of Fluid Mechanics*, vol. 429, pp. 187–216, 2001.

[50] T. A. Lavin, S. S. Girimaji, S. Suman, and H. Yu, "Flow-thermodynamics interactions in rapidly-sheared compressible turbulence," *Theoretical and Computational Fluid Dynamics*, vol. 26, no. 6, pp. 501–522, 2012.

[51] S. A. Orszag, "Accurate solution of the Orr-Sommerfeld stability equation," *Journal of Fluid Mechanics*, vol. 50, pp. 689–703, 1971.

[52] A. Davey, "A simple numerical method for solving Orr-Sommerfeld problems," *Quarterly Journal of Mechanics and Applied Mathematics*, vol. 26, no. 4, pp. 401–411, 1973.

[53] J. M. Gersting and D. F. Jankowski, "Numerical methods for Orr-Sommerfeld problems," *International Journal for Numerical Methods in Engineering*, vol. 4, no. 2, pp. 195–206, 1972.

[54] Z. Xie and G. Girimaji, "Instability of Poiseuille flow at extreme mach numbers: Linear analysis and simulations," *Physical Review E*, vol. 89, no. 4, p. 043001, 2014.